APPROVAL SHEET

Title of Dissertation: Modeling phase noise and nonlinearity in photodetectors

Name of Candidate: Seyed Ehsan Jamali Mahabadi
                     Doctor of Philosophy, 2020

Dissertation and Abstract Approved: _____
                                    Curtis R. Menyuk
                                    Professor
                                    Department of Computer Science and Electrical
                                    Engineering

Date Approved: ___11/23/2020_____

Ehsan Jamali

✉ sjamali1@umbc.edu,

EDUCATION

- **University of Maryland, Baltimore County** — Baltimore, MD
  Ph.D. in Electrical Engineering, GPA 3.84 — Expected: December 2020
  - Dissertation: Modeling nonlinearity and phase noise in photodetectors
- **University of Maryland, Baltimore County** — Baltimore, MD
  M.S. in Electrical Engineering, GPA 3.84 — August 2018

PROFESSIONAL EXPERIENCE

- **Computational Photonics Laboratory, University of Maryland, Baltimore County** — Baltimore, MD
  Graduate Research Assistant — August 2012 - Present

  In-depth knowledge and understanding of semiconductor devices, electro-optic components, and semiconductor lasers design, modeling, and performance optimization

  - Modeled the impulse response in p-i-n and modified uni-traveling carrier photodetectors
  - Modeled phase noise in high-power photodetectors
  - Modeled impact of nonlinearity on RF-modulated frequency combs in high power photodetectors
  - Developed Matlab codes to model nonlinearity in high-power photodetectors
  - Investigated and modeled carrier transport and gain recovery in quantum cascade lasers
  - Modeled pump-probe experiments with quantum cascade lasers
  - Developed Matlab codes to model, design, and engineer quantum cascade lasers
  - Designed and modeled power LDMOSFETs to achieve high breakdown voltages and improve self-heating behavior
  - Collaborated with experimentalists at the Naval Research Laboratory and National Institute of Standards and Technology
  - Led a team of undergraduate students as a mentor in an NSF undergraduate research program to develop Matlab codes to model noise in photodetectors
  - Designed, modeled, and fabricated Schottky diodes at Microfabrication Laboratory

- **CSEE Department, University of Maryland, Baltimore County** — Baltimore, MD
  Graduate Teaching Assistant — August 2012 - May 2013
  - Assisted with instructional responsibilities of Electromagnetic Theory and Digital Logic courses
  - Held weekly discussion/laboratory sessions and office hours, reinforced and followed-up student learning activities

COMPUTER SKILL

Simulation Software: Atlas Semiconductor Device Simulator of Silvaco, Electronics Work Bench, MultiSim, Protel DXP, Proteus, Cadence, COMSOL
Programming Skills: C/C++, Matlab, Java, Python
Other skills: LaTeX, Microsoft office, Visio, Mathematica, parallel computing

MATHEMATICAL SKILL

Partial differential equations, numerical optimization, signal processing, Monte Carlo simulation, Fourier analysis, spectrum analysis

Relevant Coursework

Advanced Electromagnetic Theory, Custom VLSI design, Lasers, Quantum Mechanics, Semiconductor Devices, Solid State Electronics

Volunteer Works

Served as the college of engineering dean advisory committee member at University of Maryland, Baltimore County
Served as the president of the Iranian Graduate Student Association at University of Maryland, Baltimore County
Served as CCEE department senator in the Graduate Student Association at University of Maryland, Baltimore County

Journal Publications

1- **S. E. Jamali Mahabadi**, T. F. Carruthers, C. R. Menyuk, J. D. McKinney, and K. J. Williams, "Comparison of the impact of nonlinearity in a p-i-n and MUTC photodetector on electro-optic frequency combs," Under peer review process Opt. Lett. (2020).

2- **S. E. Jamali Mahabadi**, T. F. Carruthers, C. R. Menyuk, J. D. McKinney, and K. J. Williams, "Impact of nonlinearity including bleaching in MUTC photodetectors on RF-modulated electro-optic frequency combs," Prepared to submit to Opt. Express (2020).

3- **S. E. Jamali Mahabadi**, T. F. Carruthers, C. R. Menyuk, J. D. McKinney, and K. J. Williams, "Impact of nonlinearity including bleaching in p-i-n photodetectors on RF-modulated electro-optic frequency combs," Prepared to submit to Opt. Express (2020).

4- S. Wang, C. Tu, **S. E. Jamali Mahabadi**, S. Droste, L. C. Sinclair, I. Coddington, N. R. Newbury, T. F. Carruthers, and C. R. Menyuk, "Obtaining more energetic modelocked pulses from a SESAM-based fiber laser," Opt. Express **28**, 20345–20361 (2020).

5- **S. E. Jamali Mahabadi**, S. Wang, T. F. Carruthers, C. R. Menyuk, F. J. Quinlan, M. N. Hutchinson, J. D. McKinney, and K. J. Williams, "Calculation of the impulse response and phase noise of a high-current photodetector using the drift-diffusion equations," Opt. Express **27**, 3717–3730 (2019).

6- **S. E. Jamali Mahabadi**, Y. Hu, M. A. Talukder, T. F. Carruthers, C. R. Menyuk, "A comprehensive model of gain recovery due to unipolar electron transport after a short optical pulse in quantum cascade lasers," J. Appl. Phys. **120**, 154502 (2016).

7- **S. E. Jamali Mahabadi**, "Upper drift region double step partial SOI LDMOSFET: A novel device for enhancing breakdown voltage and output characteristics," Superlattice Microst. **89**, 345–354 (2016).

8- **S. E. Jamali Mahabadi** and H. A. Moghadam, "Comprehensive study of a 4H–SiC MES–MOSFET," Physica E Low Dimens. Syst. Nanostruct. **74**, 25–29 (2015).

9- **S. E. Jamali Mahabadi**, S. Rajabi, and J. Loiacono, "A novel partial SOI LDMOSFET with periodic buried oxide for breakdown voltage and self heating effect enhancement," Superlattice Microst. **85**, 872–879 (2015).

10- H. A. Moghadam, A. A. Orouji, and **S. E. Jamali Mahabadi**, "Employing reduced surface field technique by a P-type region in 4H–SiC MESFETs for increasing breakdown voltage," Int. J. Numer. Model. Electon. Netw. Devices Fields **2**, 103–111 (2013).

11- A. A. Orouji, **S. E. Jamali Mahabadi**, and P. Keshavarzi, "A novel partial SOI LDMOSFET with a trench and buried P layer for breakdown voltage improvement," Superlattice Microst. **50**, 449–460 (2011).

12- **S. E. Jamali Mahabadi**, A. A. Orouji, P. Keshavarzi, and H. A. Moghadam, "A new partial SOI-LDMOSFET with a modified buried oxide layer for improving self-heating and breakdown voltage," Semicond. Sci. Technol. **26**, 095005 (2011).

1- **S. E. Jamali Mahabadi**, T. F. Carruthers, C. R. Menyuk, J. D. McKinney, and K. J. Williams, "Impact on frequency combs of nonlinearity including bleaching in p-i-n photodetectors," in IEEE Photonics Society Summer Topicals Meeting (IEEE, 2020), pp. 1–2.

2- **S. E. Jamali Mahabadi**, T. F. Carruthers, C. R. Menyuk, M. N. Hutchinson, J. D. McKinney, and K. J. Williams, "Impact of nonlinearity on RF-modulated frequency combs with different modulation depths in an MUTC photodetector," in IEEE International Topical Meeting on Microwave Photonics (IEEE, 2019), pp. 1–4.

3- **S. E. Jamali Mahabadi**, T. F. Carruthers, C. R. Menyuk, M. N. Hutchinson, J. D. McKinney, and K. J. Williams, "Impact of nonlinearity in an MUTC photodetector on an RF-modulated frequency comb," in IEEE Photonics Conference (IEEE, 2019), pp. 1–2.

4- **S. E. Jamali Mahabadi**, T. F. Carruthers, and C. R. Menyuk, "Modeling phase noise in high-power photodetectors," in IEEE International Conference on Numerical Simulation of Optoelectronic Devices (IEEE, 2019), pp. 65–66.

5- **S. E. Jamali Mahabadi** and C. R. Menyuk, "Calculation of the impulse response of PIN and MUTC photodetectors using the drift-diffusion equations," in Laser Science (Optical Society of America, 2017), paper JTu2A-53.

6- N. Sardesai, **S. E. Jamali Mahabadi**, Q. Meng, and F. S. Choa, "Comparative analysis of recorded brain EEG signals generated from from the right and left hand while writing," Proc. SPIE 9863, 98630S–98630S (2016).

7- S. Rajabi, A. A. Orouji, H. A. Moghadam, **S. E. Jamali Mahabadi**, and M. Fathipour, "A novel AlGaN/GaN/AlGaN double-heterojunction high electron mobility transistor for performance improvement," in IEEE International Conference on Signal Processing, Communication, Computing and Networking Technologies (IEEE, 2011), pp. 675–678.

8- **S. E. Jamali Mahabadi**, A. A. Orouji, P. Keshavarzi, S. Rajabi, and H. A. Moghadam, "A novel step buried oxide partial SOI LDMOSFET with triple drift layer," in IEEE International Conference on Signal Processing, Communication, Computing and Networking Technologies (IEEE, 2011), pp. 174–177.

9- S. Rajabi, A. A. Orouji, H. A. Moghadam, **S. E. Jamali Mahabadi**, and M. Fathipour, "A novel double field-plate power high electron mobility transistor based on AlGaN/GaN for performance improvement," in IEEE International Conference on Signal Processing, Communication, Computing and Networking Technologies (IEEE, 2011), pp. 272–276.

10- S. Rajabi, A. A. Orouji, H. A. Moghadam, **S. E. Jamali Mahabadi**, and M. Fathipour, "A novel power High Electron Mobility Transistor with partial stepped recess in the drain access region for performance improvement," in IEEE International Conference on Signal Processing, Communication, Computing and Networking Technologies (IEEE, 2011), pp. 269–271.

11- H. A. Moghadam, **S. E. Jamali Mahabadi**, and S. Rajabi, "Combination of a 4H-SiC MESFET with a 4H-SiC MOSFET to realize a high voltage MOSFET," in IEEE International Conference on Signal Processing, Communication, Computing and Networking Technologies (IEEE, 2011), pp. 172–173.

12- H. A. Moghadam, **S. E. Jamali Mahabadi**, and S. Rajabi, "4H-SiC SOI-MESFET with a step in buried oxide for improving electrical performance," in IEEE International Conference on Computer Science and Automation Engineering (IEEE, 2011), pp. 219–222.

13- **S. E. Jamali Mahabadi**, A. A. Orouji, H. A. Moghadam, and P. Keshavarzi, "A new method for improving breakdown voltage in PSOI MOSFETs using variable drift region doping concentration," in IEEE International Conference on Computer Science and Automation Engineering (IEEE, 2011), pp. 57–60.

A full list of all publications is available at (https://scholar.google.com/citations?user=soglCLwAAAAJ&hl=en)

ABSTRACT

Title of dissertation:	MODELING PHASE NOISE AND NONLINEARITY IN PHOTODETECTORS
	Seyed Ehsan Jamali Mahabadi Doctor of Philosophy, 2020
Dissertation directed by:	Professor Curtis R. Menyuk Department of Computer Science and Electrical Engineering, University of Maryland, Baltimore County

High-power photodetectors are important devices in the analog optical links that are present in many RF-photonic systems. The wide bandwidth of RF-photonic links, along with their immunity to electromagnetic interference, and their decreased size, weight, and power requirements compared to other microwave systems make them an appropriate choice in a variety of applications. Applications include antenna remoting and radio-over-fiber, beamforming in phased-array radars, and optical signal processing of microwave signals.

Phase noise in photodetectors is a critical limiting factor in many RF-photonic applications, particularly metrology applications in which phase noise limits the extent to which the inherently low noise of an optical comb can be transferred to microwaves.

Bleaching or absorption saturation can occur in a high-current photodetector when the high density of photogenerated carriers either saturate the number of available final energy states or depopulate the initial states. Additionally, the high density of photogenerated electrons can increase the possibility that they are recaptured. Bleaching leads to a reduction in the photodetector's responsivity as the peak intensity and hence the average power increases. Bleaching can, in turn, lead to nonlinear distortion of an incoming RF-photonic signal and limit the performance of photonic analog-to-digital converters (PADCs).

In this dissertation, we first describe prior work on a one-dimensional (1-D) drift-diffusion model that we used to study phase noise in a modified uni-traveling carrier (MUTC) photodetector and the bleaching effect in p-i-n and MUTC photodetectors. We then describe a procedure to calculate the impulse response and phase noise of high-current photodetectors using the drift-diffusion equations while avoiding computationally expensive Monte Carlo simulations. We apply this procedure to an MUTC photodetector. In our approach, we first use the full drift-diffusion equations to calculate the steady-state photodetector parameters. We then perturb the generation rate as a function of time to calculate the impulse response. We next calculate the fundamental shot noise limit and cut-off frequency of the device. We find the contributions of the electron, hole, and displacement currents. Finally, we calculate the phase noise of an MUTC photodetector.

Applying our approach, we found good agreement between our results, the Monte Carlo simulation results, and experimental results. We showed that phase noise is minimized by having a fast photocurrent response with a tail that is as small as possible. Our approach is much faster computationally than Monte Carlo simulations, making it possible to carry out a broad parameter study to optimize the device performance. We propose a new optimized structure with lower phase noise and reduced nonlinearity.

We next study the impact of photodetector nonlinearity on RF-modulated frequency combs. Frequency combs can be used in RF-photonic systems to disambiguate radar signals and to increase the threshold for Brillouin scattering in optical fiber links. In addition to the sources of nonlinearity that are present when detecting continuous wave (CW) signals, the high peak power of optical frequency combs can bleach the photodetectors and contribute to the nonlinear distortion of the RF signal.

We developed an empirical model of bleaching, which we added to the 1-D drift-diffusion model that we previously developed. We determined the parameters of this model by comparison with experimental results in both pulsed and CW modes in a p-i-n photodetector and in the pulsed mode in an MUTC photodetector.

We calculated the impact of the bleaching on device nonlinearity as a function of average optical power. We used the three-tone modulation technique to calculate the second- and third-order intermodulation distortions (IMD2 and IMD3) in the pulsed mode [1]. We calculated the second- and third-order output intercept points (OIP2 and OIP3) to characterize IMD2 and IMD3. The output of modulated optical pulse trains in the photodetector corresponds to a set of frequency comb lines in the frequency domain. With a CW input, there is a single IMD2 and IMD3 and a single OIP2 and OIP3. By contrast, with an optical frequency comb input, there is a different $IMD2_n$, $IMD3_n$, $OIP2_n$, and $OIP3_n$ associated with each comb line n. We determined the behavior of $IMD2_n$, $IMD3_n$, $OIP2_n$, and $OIP3_n$ as a function of comb line frequency ($f = nf_r$, where n is the comb line number and f_r is the repetition frequency) both with and without bleaching to determine the impact of bleaching on nonlinear distortion products in the p-i-n and MUTC photodetectors. We found that when bleaching is included, $OIP2_n$ and $OIP3_n$ are higher in the p-i-n photodetector than the MUTC photodetector, and the difference between them increases as the comb line frequency increases. We calculated the distortion-to-signal strength ratios $\rho_{2n} = IMD2_n/S_{in}$ and $\rho_{3n} = IMD3_n/S_{in}$, where S_{in} is the fundamental power as a function of comb line frequency with and without bleaching. We found that these ratios increase as the comb line number increases, which means that the impact of nonlinearity becomes larger as the comb line number increases. We showed that the impact of bleaching on the ratios ρ_{2n} and ρ_{3n} is complex and not always detrimental. In the MUTC photodetector, when $n \lesssim 100$ ($\lesssim 5$ GHz), we found that the ratio is higher with bleaching. On the other hand, when $n \gtrsim 100$ ($\gtrsim 5$ GHz), the ratio is lower with bleaching, so that bleaching actually improves this ratio. We found nonlinear distortion is greater for the p-i-n photodetector than it is for the MUTC photodetector at low comb line frequencies and the opposite is true at high comb line frequencies.

MODELING PHASE NOISE AND NONLINEARITY IN PHOTODETECTORS

by

Seyed Ehsan Jamali Mahabadi

Dissertation submitted to the Faculty of the Graduate School of the
University of Maryland, Baltimore County in partial fulfillment
of the requirements for the degree of
Doctor of Philosophy
2020

Advisory Committee:
Professor Curtis R. Menyuk, Chair/Advisor
Professor Li Yan
Professor Anthony M. Johnson
Professor Terrance L. Worchesky
Dr. Thomas F. Carruthers
Dr. Jason D. McKinney

To my wonderful parents and dear wife

Acknowledgments

I would like to express my sincere gratitude to my advisor, Professor Curtis Menyuk for his endless and unwavering support throughout my Ph.D. education. His encouragement, advice, constructive criticism and truly scientific intuition and wisdom inspired me and enriched my growth as a researcher. Working with him has nourished my intellectual maturity, and I will benefit from that for the remainder of my life. I appreciate the opportunity that he gave me to work with him and learn from him. It is a great honor to finish this work under his supervision.

I cannot express enough thanks to my committee members for their continued support and encouragement: Dr. Thomas Carruthers, Dr. Jason McKinney, Professor Li Yan, Professor Anthony Johnson, and Professor Terrance Worchesky. I offer my sincere appreciation for the learning opportunities provided by my committee.

The completion of my Ph.D. research could not have been accomplished without the support of my colleagues in the Computational Photonics Laboratory: Joe Weiblen, Jerry Wang, Yue Hu, Zhen Qi, Patrick Sykes, Chaoran Tu, and Ishraq Anjum. Thank you all for the stimulating discussions, for the help and support during hard times, and for all the fun we have had while working together.

Also, I would like to thank my parents for the unconditional love and support they gave me, and sacrifices they made for my future.

Finally, to my caring, loving, and supportive wife, Maryam, my deepest gratitude. Your encouragement when the times got rough are much appreciated and duly noted. It was a great comfort to be with you during this journey.

Table of Contents

List of Tables

List of Figures

Chapter 1

Introduction

A photodetector is a device that measures photon flux or optical power by converting the energy of the absorbed photons into an electronic form. Two principal classes of photodetectors are thermal detectors and photoelectric detectors. Thermal detectors operate by converting photon energy into heat. However, most thermal detectors are inefficient and slow compared to photoelectric detectors as a result of the time required to change their temperatures. Consequently, they are not suitable for most applications in photonics [2]. The operation of photoelectric detectors is based on the absorption of photons in a material that results directly in an electronic transition to higher energy levels in which the charge carriers are mobile. Under the effect of an electric field these carriers move and produce a measurable electric current [2]. We only consider photoelectric detectors in this dissertation.

1.1 Basic photodetector structure and physics

Photoelectric photodetectors are semiconductor devices that detect optical signals. At its operating wavelength, a photodetector should have high sensitivity, a low response time, low noise, small size, and high reliability under operating conditions [3, 4]. The operation of a photodetector proceeds in three steps: carrier generation by incident light, carrier transport and/or multiplication by whatever
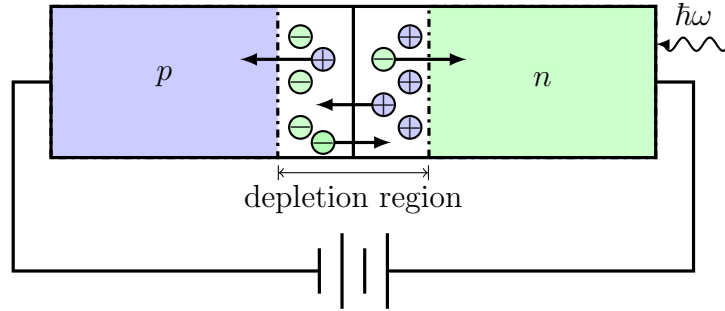
Figure 1.1: Diagram of a reverse-biased *p-n* photodetector.

physical current-gain mechanism exists in the device, and interaction of the current with the external circuit to provide the output signal [5]. Photodetectors have a broad range of applications, including infrared sensors in opto-isolators and detectors for optical-fiber communications and microwave photonics [6].

When incident light hits the surface of the photoconductor, electron-hole pairs are generated either by band-to-band transitions (intrinsic) that lead to creation of electron-hole pairs or by transitions involving forbidden-gap energy levels (extrinsic), band-to-impurity level or impurity-to-band level transitions, in which only one type of mobile carrier is created [7].

The simplest type of photodetector is a *p-n* junction that operates under a reverse bias. Figure 1.1 shows a diagram of a *p-n* photodetector under reverse bias. The electric field distribution is nonuniform, and the maximum field is at the junction. When an optical signal penetrates into the depletion region of the photodetector, the electric field in the depletion region serves to separate the photo-generated electron-hole pairs, and an electric current is generated that flows in the external circuit. The photogenerated holes drift in the depletion region, diffuse into
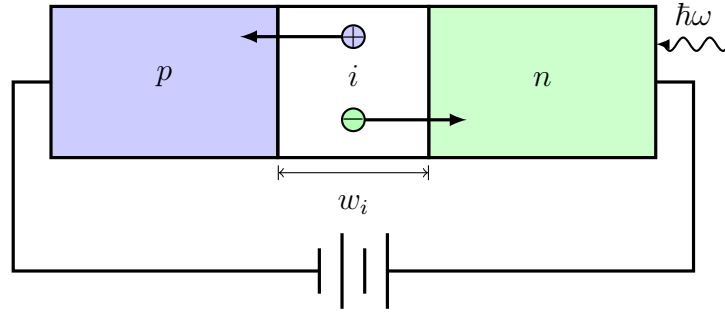
Figure 1.2: Diagram of a reverse-biased *p-i-n* photodetector.

the neutral *p*-region, and then combine with electrons that come from the negative electrode. Similarly, photogenerated electrons drift in the opposite direction. When an optical signal penetrates within a diffusion length outside the depletion region, the photogenerated carriers will diffuse into the depletion region and drift across the depletion region to the other side. These neutral regions can be regarded as resistive extensions of electrodes to the depletion region. The photocurrent depends on the number of photogenerated electron-hole pairs and the drift velocities of the carriers. The current in the external circuit is only due to the flow of electrons, even though both electrons and holes drift in the depletion region. For high-frequency operation, the depletion region must be kept thin in order to reduce the transit time. On the other hand, to increase the quantum efficiency the depletion region must be sufficiently thick to allow a large fraction of the incident light to be absorbed. Thus, there is a trade-off between the response time and the quantum efficiency [4].

Figure 1.2 shows a diagram of a reverse-biased *p-i-n* photodetector. The most common photodetector in use in analog optical links is the *p-i-n* photodetector, because the undoped intrinsic region (*i*) thickness can be tailored to optimize the

quantum efficiency and frequency response [8]. The i-layer thickness is typically 5–50 μm, depending on the application. The intrinsic i-layer in a p-i-n photodetector is completely depleted. The junction capacitance is made small by having a large depletion region width, which makes it possible for the p-i-n photodetector to operate at high modulation frequencies. Its depletion region is made wide enough to have a large absorption in the depletion region at long wavelengths [9]. The p-i-n structure is designed so that almost complete optical absorption occurs in the i-layer. The electron-hole pairs that are either produced in the depletion region or are within a diffusion length of this region will eventually be separated by the electric field, and a current flows in the external circuit as carriers drift across the depletion region [9]. Generally, the response time is limited by the drift time of the holes across the width of the i-layer, since holes are the slowest photogenerated carriers.

Photodetectors are characterized by their voltage-current relation, quantum efficiency, responsivity, and response time. The voltage-current relation in p-n and p-i-n photodetectors under dark conditions and when reverse biased is defined as [10]

$$I_D = I_0 \left[\exp \left(\frac{qV}{k_B T} \right) - 1 \right], \qquad (1.1)$$

where I_0 is the reverse bias saturation current, V is the bias voltage, q is the electron charge, k_B is Boltzmann's constant, and T is the absolute temperature. In a reverse-biased photodetector, the dark current is negligible. Under continuous wave (CW)

4

illumination, the photocurrent is dependent on the input optical power and equals [2]

$$I_{\text{opt}} = \frac{\eta q}{h\nu} P_{\text{opt}}, \tag{1.2}$$

where η is the quantum efficiency, P_{opt} is the input optical power, h is Planck's constant, and ν is the frequency of incident light. The total current of a photodetector is

$$I = I_D + I_{\text{opt}}. \tag{1.3}$$

The quantum efficiency η $(0 \leq \eta \leq 1)$ of a photodetector is defined as the ratio of the number of photo-generated electron-hole pairs that contribute to the detector output current to the number of incident photons. For a surface-normal photodetector, the quantum efficiency can be written as [2]

$$\eta = (1 - R)\zeta \left[1 - \exp(-\alpha w_a)\right], \tag{1.4}$$

where R is the reflection coefficient, ζ is the fraction of electron-hole pairs that contribute to the photocurrent, α is the absorption coefficient, and w_a is the length of the absorption region in the photodetector. The responsivity $\mathfrak{R}$ is the ratio of output electrical current to the input optical power. It is defined as [2]

$$\mathfrak{R} = \frac{I_{\text{opt}}}{P_{\text{opt}}} = \frac{\eta q}{h\nu}. \tag{1.5}$$

A narrower i-layer decreases the quantity of absorbed photons and hence reduces

5

the responsivity [4].

The response time or the bandwidth of a photodetector is constrained by the transit time and the RC time constant. Since the electron mobility is larger than the hole mobility by a factor of 40 in InGaAs, the transit time is mainly determined by the hole velocity in the intrinsic region. For a p-i-n photodetector, the bandwidth is limited by this transit time and approximately equals [11]

$$f_T = \frac{v_{p,\text{sat}}}{\pi w_i},$$

(1.6)

where $v_{p,\text{sat}}$ is the saturation velocity of the holes. The RC-limited bandwidth is given by [11]

$$f_{RC} = \frac{1}{2\pi C(R_s + R_{\text{load}})},$$

(1.7)

where R_s is equivalent series resistance of the photodetector, C is the junction capacitance of the photodetector, and R_{load} is the load resistor. The capacitance in the p-i-n photodetector is given by [10]

$$C = \frac{\epsilon A}{w_i},$$

(1.8)

where ϵ is the dielectric constant and A is the effective area of the device.

1.2   Prior work on modeling photodetectors

Williams *et al.* [12, 13] used the drift-diffusion equations to develop a one-dimensional (1-D) model of high-current photodetectors, which elucidated the space-

6

charge effects in these devices. Later, Huang *et al.* [14] took into account the barrier heights at the material interfaces and the external circuit in the model. Guo *et al.* [15] took into account the change in the refractive index. Jiang *et al.* [16] developed a circuit-equivalent model to study the nonlinear distortion of the electrical signal in a *p-i-n* photodetector. Walker [17] developed 1-D and two-dimensional (2-D) models for metal-semiconductor-metal photodetectors to study the transient behavior of the photodetectors. Harari *et al.* [18] modeled a waveguide *p-i-n* photodetector and studied its behavior when the optical power is high ($\sim$ 25 mW). Afzalian *et al.* [19] implemented a 1-D model of lateral *p-i-n* photodetector to optimize the quantum efficiency, output current, speed, and dark current as a function of the intrinsic length of the diode and other operating parameters. Wilson *et al.* [20] studied the impact ionization effect in a GaAs *p-i-n* photodetector under high illumination. Recently, Fu *et al.* [21] used a 1-D drift-diffusion model to study the nonlinear intermodulation distortion in a modified uni-traveling-carrier (MUTC) photodetector. In the model, they included the Franz-Keldysh effect and impact ionization. They calculated the electric field in the device, and then calculated the absorption coefficient and impact ionization. Hu *et al.* [22] used a drift-diffusion model to study nonlinearities in a simple *p-i-n* photodetector. They later extended their model to study harmonic powers [23] and amplitude-to-phase conversion [24] in an MUTC photodetector. The model included external loading, incomplete ionization, the Franz-Keldysh effect, and history-dependent impact ionization.
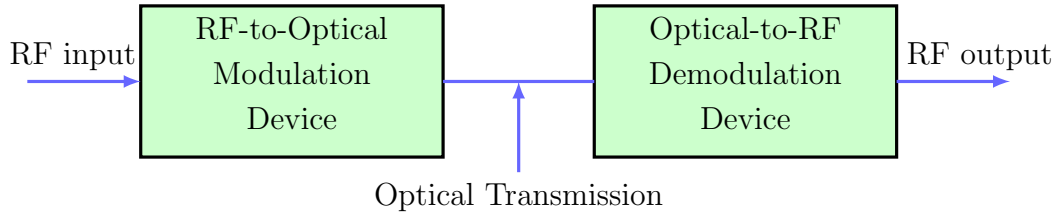
Figure 1.3: Schematic of an optical link.

1.3 Our work on modeling photodetectors

Each optical link consists of three major components: a modulator, which transfers the electrical signal onto an optical carrier, an optical fiber, and a photodetector, which turns the optical carrier back into an electrical signal. Figure 1.3 shows a schematic illustration of an optical link.

High-power photodetectors are important devices in RF-photonics [25–27] and more specifically in analog optical link applications [28]. The wide bandwidth of these photodetectors, their immunity to electromagnetic interference, and their low size, weight, and power relative to RF detectors make optical links an appealing choice in variety of applications [29].

In order to overcome the limitations of analog-to-digital converters at higher frequencies, sub-sampling techniques may be employed, which sample a signal at rates below the Nyquist frequency limit [30]. For sub-sampling to be most useful, it is necessary to overcome the frequency ambiguity introduced by aliasing. Since sub-sampling causes multiple input frequencies to alias to the same output frequency, the input frequency and thus the input spectrum cannot be reconstructed by frequency measurement alone [31]. For this reason, frequency disambiguation techniques have

been developed, which typically involve the use of multiple samplers [32–36] (e.g., periodic samplers interleaved in time or operating at different frequencies), or a single sampler operating at a non-uniform sampling rate [37–39].

By utilizing a non-uniform sampling rate, additional information is provided in the sub-sampled signal that can be used to disambiguate, or determine, the input frequency [32, 40]. Harmen and McKinney [37] introduced a novel technique for broadband RF disambiguation, which exploits a known jitter imparted onto the sampling rate of an optical pulse source in a subsampled analog optical link. This sampling technique allowed for ultra-wideband signal recovery with a single measurement. They showed reliable disambiguation for signals with center frequencies spanning 1 MHz – 40 GHz. Schermer and and McKinney [31] used acousto-optic delay modulation for non-uniform sub-Nyquist optical sampling.

Photogenerated electrons and holes in the depletion region of a p-i-n photodetector produce space charge effects in which the external electric field is partially blocked, resulting in field modulation and limitations in high frequency operation. Because of their much lower drift velocity, holes dominate the space charge. The speed of the photoresponse is also mostly determined by hole transport due to the lower mobility of the holes. To increase the speed of high-current photodetectors, it is advantageous to avoid using holes as active carriers. Uni-traveling carrier (UTC) photodetectors only use electrons as active carriers [41] by blocking the motion of the photogenerated holes and can thereby achieve higher output currents than is possible for p-i-n photodetectors [41]. The development of UTC photodetectors was followed by the development of MUTC photodetectors [42]. There is a cliff layer in

9

the MUTC structure between the collection region and the absorption region, which is moderately doped and reduces the space charge effect at high photocurrents [42].

We have extended the model of Hu *et al.* [22] and Williams [43] using the drift-diffusion equations to calculate the impulse response and phase noise of high-current photodetectors and to include bleaching [28, 44] for both *p-i-n* and MUTC photodetector.

Phase noise in photodetectors is a critical limiting factor in many RF-photonic applications [2, 28]. This limit is particularly important in metrology applications, in which phase noise limits the extent to which the low noise of an optical comb can be transferred to a photodetected electronic microwave signal [28].

Quinlan *et al.* [45] predicted that the phase noise is reduced when the photodetector is illuminated by short optical pulses, and experiments showed a significant reduction in the phase noise for short pulses [46]. However, the prediction in Ref. [45] that the phase noise disappears as the pulse duration tends to zero is not observed experimentally. Instead, the decrease in the phase noise ceases once the optical pulse duration becomes smaller than the duration of the electrical pulses that emerge from the photodetector. Sun *et al.* [47] were able to reproduce these experimental results using Monte Carlo simulations that accounted for collisional diffusion of electrons in the device. However, they did not take advantage of the fact that the distribution of electrons in any time slot is expected to be Poissonian, which simplifies the calculations and physical interpretation of the results. More practically, the Monte Carlo simulations are too computationally slow to be useful for performance optimization.

To calculate the impulse response and the phase noise of high-current pho-

todetectors, we use the drift-diffusion equations, which makes it possible to avoid computationally expensive Monte Carlo simulations. We have applied this procedure to an MUTC photodetector [48–51] and will describe our results in detail in Chapters 3 and 4. We first calculated the steady-state photodetector parameters. We then perturbed the generation rate as a function of time in the drift-diffusion equations to calculate the impulse response. We next calculated the fundamental shot noise limit and cut-off frequency of the devices. We found the contributions of the electron, hole, and displacement currents. Finally, we calculated the phase noise of an MUTC photodetector and compared our results to Monte Carlo simulation results and experimental results. Since our approach is much faster computationally than Monte Carlo simulations, we were able to perform a comprehensive parameter study, and we proposed a new structure with lower phase noise and reduced nonlinearity.

Bleaching or absorption saturation in a high-current photodetector can occur when intense optical fields either saturate the number of available final energy states or depopulate the initial states [28]. Additionally, the high density of photogenerated electrons can increase the possibility that they are recaptured. Bleaching leads to a reduction in the photodetector's responsivity as the peak intensity and hence the average power increases. This decrease in responsivity can lead in turn to nonlinear distortion of an incoming RF-photonic signal. Juodawlkis *et al.* [44] have reported that this effect can limit the performance of photonic analog-to-digital converters (PADCs).

We have developed an empirical model of bleaching, and we have incorporated

11

this model into the 1-D drift-diffusion equations in order to calculate its impact on the nonlinear distortion in p-i-n and MUTC photodetectors. We determined the parameters of the bleaching model by comparison with experimental results both in the pulsed mode and the CW mode in a p-i-n photodetector [13] and in the pulsed mode in an MUTC photodetector [42]. We developed our bleaching model starting with the rate equations for a two-level system. In practice, however, the physics of bleaching is complex and poorly understood. We have found it necessary to use a slightly more sophisticated empirical model that includes quadratic terms in the numerator and denominator in order to obtain agreement with the experimental measurements. Our calculations are presented in detail in Chapter 5.

We calculate the impact of nonlinearity including the effect of bleaching in p-i-n and MUTC photodetectors in the pulsed mode as a function of the average input optical power. When considering nonlinearities in photodetectors, second-order intermodulation distortion (IMD2) and third-order intermodulation distortion (IMD3) are particularly significant. Frequencies that IMD3 generates can be close to the fundamental modulation frequencies. The second-order output intercept point (OIP2) and the third-order output intercept point (OIP3) with the fundamental frequency response are the key figures of merit to characterize IMD2 and IMD3. OIP2 is defined as the extrapolated intercept point of the power of the fundamental frequency and IMD2, while OIP3 is defined as the extrapolated intercept point of the power of the fundamental frequency and IMD3 [1].

There is a key difference between CW and frequency comb inputs. For a CW input, there is only one set of IMD2, IMD3, OIP2, and OIP3 for a given RF

modulation frequency. By contrast, for a frequency comb input, there will be a different $IMD2_n$, $IMD3_n$, $OIP2_n$, and $OIP3_n$ for each comb line n. We calculate these quantities for each of the comb lines for a repetition rate of 20 ns and powers of 0.1–50 mW that correspond to experiments that are being carried out at the Naval Research Laboratory. We carry out our calculations both with and without bleaching to determine the impact of bleaching [52–54]. We show in Chapter 6 that bleaching impacts the nonlinearity differently for different comb lines.

Chapter 2

Modeling a *p-i-n* and an MUTC photodetector: Review of prior work

Models that we are using in this dissertation are based on the models that were developed by Williams [43] and Hu [55]. In this chapter we are repeating and reviewing the models and materials that were presented by Williams and Hu for completeness.

2.1   *p-i-n* and MUTC photodetector structures

2.1.1   *p-i-n* structure

In Fig. 2.1, we show the *p-i-n* photodetector structure that we study. It is a single heterojunction device made of InP and InGaAs. The device is composed of a highly-doped transparent *n*-InP substrate of length $w_n = 0.1$ μm ($N_D = 2 \times 10^{17}$ cm^{-3}), an intrinsic region of *n*-InGaAs of length $w_i = 0.95$ μm ($N_B = 5 \times 10^{15}$ cm^{-3}), and a degenerately doped *p*-InGaAs *p*-region of length $w_p = 1$ μm ($N_A = 7 \times 10^{18}$ cm^{-3}), where N_A and N_D denote the acceptor and donor densities, and N_B denotes the unintentional donor density in the intrinsic region. The total length of the photodetector is $L = 2.05$ μm. The incident light is assumed to pass through an aperture on the *n*-side ohmic contact of the device. The device radius is 15 μm. In our simulations of this device, we consistently use these same device parameters except as noted. These parameters were first used by Williams *et al.* [13]
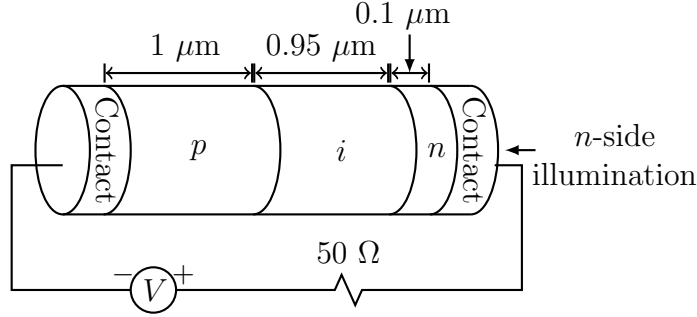
Figure 2.1: *p-i-n* photodetector structure. This figure is taken from Hu [55].

2.1.2 MUTC structure

Photogenerated electrons and holes in the depletion region of a *p-i-n* photodetector produce space charge, resulting in nonlinear distortion of the optical field and limiting the RF frequencies that the optical field can carry. Because of their lower drift velocity, holes dominate the space charge. The speed of the photoresponse is also mostly determined by hole transport due to the lower mobility of the holes (~ 40 times lower than electrons in InGaAs at low electric fields and almost double at high electric fields).

To increase the speed of high-current photodetectors, it is advantageous to avoid using holes as active carriers. Uni-traveling carrier (UTC) photodetectors only use electrons as active carriers and can thereby achieve higher output currents than can *p-i-n* photodetectors [41].

In Fig. 2.2 we schematically show the band diagram of a UTC photodetector. The main difference between a *p-i-n* photodetector and a UTC photodetector is the position of the absorption region. In a *p-i-n* photodetector, the depleted region
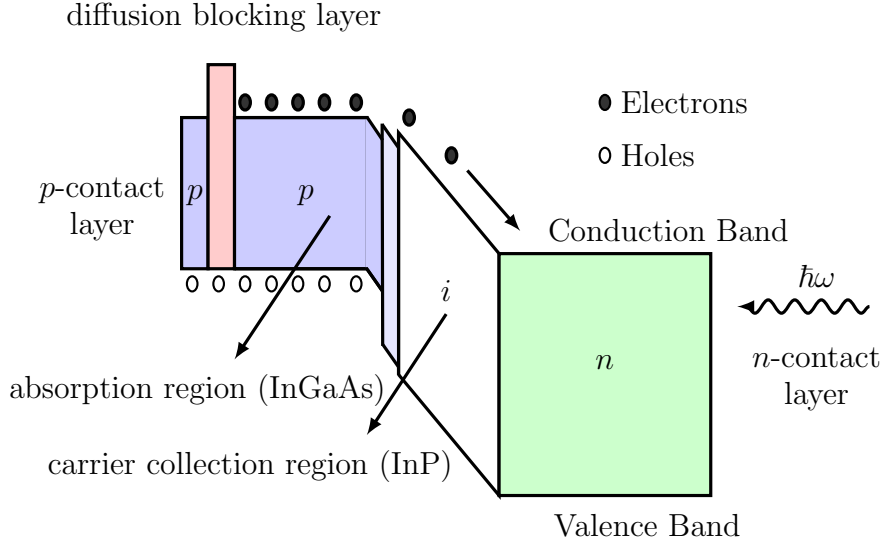
Figure 2.2: UTC photodetector band diagram. This figure is similar to Fig. 1 in Ito [56].

and the p-region are used as the absorption layers. Holes have to travel through the entire intrinsic region and the p-region in order to reach the p-contact. The response time of a p-i-n photodetector is determined by the velocity of the holes and is longer than the response time of electrons. In a UTC photodetector, the only absorption layers are in the p-region. The intrinsic region is used for collection. Photogenerated majority holes diffuse almost immediately to the p-contact. The photogenerated minority electrons in the absorption layers diffuse (and/or drift) into the depleted collection region. Hence, the response time of a UTC photodetector is only determined by the electron transport in the device [56]. There is a diffusion blocking layer on the left side of the absorption region that prevents electrons from diffusing to the p-contact. Between the absorption region and collection region, a graded energy gap helps the electrons transit through the interface and thus reduces the transport time [55]. UTC photodetectors have a rapid response
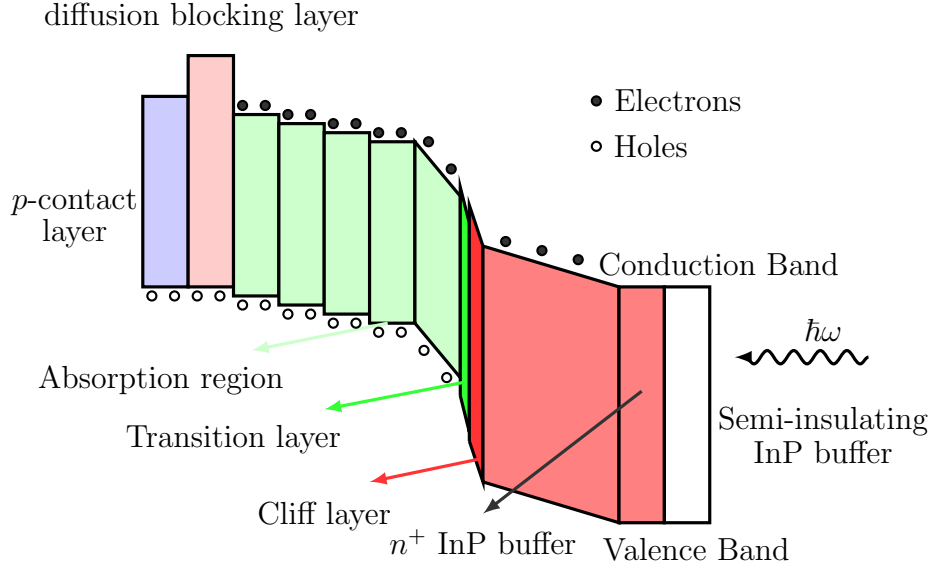
Figure 2.3: MUTC photodetector band diagram.

($\sim 10^{-12}$ s) without sacrificing responsivity. UTC photodetectors also have a high output saturation current (~ 100 mA) because of the reduced space charge effect compared to p-i-n photodetectors [41]. To date, a record 3-dB bandwidth of 310 GHz and a millimeter-wave output power of over 13 dBm at 100 GHz have been achieved [56] using a short pulse and an effective load of 12.5 Ω. With a 50-Ω load, Rouvalis et $al.$ [57] obtained a responsivity of 0.27 A/W, a 3-dB bandwidth of 170 GHz, and an output power of -9 dBm at 200 GHz.

The development of UTC photodetectors was followed by the development of modified-uni-traveling-carrier (MUTC) photodetectors [42]. Figure 2.3 shows the band diagram of an MUTC structure. There is a cliff layer in the MUTC structure between the collection region and the absorption layers, which is moderately doped and reduces the space charge effect at high photocurrents [42]. In a standard UTC device, the electric field is higher in the entire intrinsic region than elsewhere in the

InGaAs, p^+, Zn, 2.0×10^{19}, 50 nm
InP, p^+, Zn, 1.5×10^{18}, 100 nm
InGaAsP, Q1.1, Zn, 2.0×10^{18}, 15 nm
InGaAsP, Q1.4, Zn, 2.0×10^{18}, 15 nm
InGaAs, p, Zn, 2.0×10^{18}, 100 nm
InGaAs, p, Zn, 1.2×10^{18}, 150 nm
InGaAs, p, Zn, 8.0×10^{17}, 200 nm
InGaAs, p, Zn, 5.0×10^{17}, 250 nm
InGaAs, Si, 1.0×10^{16}, 150 nm
InGaAsP, Q1.4, Si, 1.0×10^{16}, 15 nm
InGaAsP, Q1.1, Si, 1.0×10^{16}, 15 nm
InP, Si, 1.4×10^{17}, 50 nm
InP, Si, 1.0×10^{16}, 900 nm
InP, n^+, Si, 1.0×10^{18}, 100 nm
InP, n^+, Si, 1.0×10^{19}, 900 nm
InGaAs, n^+, Si, 1.0×10^{19}, 20 nm
InP, n^+, Si, 1.0×10^{19}, 200 nm
InP, semi-insulating substrate Double side polished

Figure 2.4: Structure of the MUTC photodetector [42] that we have modeled to date. Green indicates the absorption regions, which include an intrinsic region and a p-doped region. Red indicates highly doped InP layers, purple indicates highly-doped InGaAs layers, and white indicates other layers.

device. In an MUTC device, the electric field is only large in the InGaAs intrinsic layer, rather than the entire intrinsic region, which decreases the space charge effect. Additionally, there is a thin intrinsic layer of InGaAs, which is used to increase the responsivity. In Fig. 2.4 we show the MUTC structure [42] that we have modeled.

2.2 Drift-diffusion model

We use a one-dimensional (1-D) model of the p-i-n and MUTC photodetectors [22–24, 58–62] to model carrier transport in these photodetectors. We account for external loading, impact ionization, and the Franz-Keldysh effect as needed in our simulations. Our starting point is the electron and hole continuity equations and the Poisson equation,

$$
\frac{\partial(p - N_A^-)}{\partial t} = -\frac{1}{q}\nabla \cdot \mathbf{J}_p + G_{\text{ii}} + G_{\text{opt}} - R(n, p),
$$

$$
\frac{\partial(n - N_D^+)}{\partial t} = +\frac{1}{q}\nabla \cdot \mathbf{J}_n + G_{\text{ii}} + G_{\text{opt}} - R(n, p), \tag{2.1}
$$

$$
\nabla \cdot \mathbf{E} = \frac{q}{\epsilon}\left(n - p + N_A^- - N_D^+\right),
$$

where n is the electron density, p is the hole density, t is time, q is the unit of charge, $\mathbf{J}_n$ is the electron current density, $\mathbf{J}_p$ is the hole current density, R is the recombination rate, G_{ii} and G_{opt} are impact ionization and optical generation rates, $\mathbf{E}$ is the electric field at any point in the device, ϵ is the material permittivity, N_A^- is the ionized acceptor concentration, and N_D^+ is the ionized donor concentration. The electron and hole current densities are governed by the equations

$$
\mathbf{J}_p = qp\mathbf{v}_p(\mathbf{E}) - qD_p\nabla p,
$$

$$
\mathbf{J}_n = qn\mathbf{v}_n(\mathbf{E}) + qD_n\nabla n, \tag{2.2}
$$

where $\mathbf{v}_n(\mathbf{E})$ and $\mathbf{v}_p(\mathbf{E})$ are the electric-field-dependent electron and hole drift velocities, D_n is the electron diffusion coefficient, and D_p is the hole diffusion coefficient.

19

Windhorn *et al.* [63] have measured the electron drift velocity as a function of the electric field for InGaAs at electric field strengths from 10–100 kV/cm. Dentan *et al.* [59] proposed an empirical expression for $\mathbf{v}_n(\mathbf{E})$ to fit the measured results in InGaAs. Their expression is

$$\mathbf{v}_n(\mathbf{E}) = \frac{\mathbf{E}\left(\mu_n + v_{n,\text{sat}}\beta|\mathbf{E}|\right)}{1 + \beta|\mathbf{E}|^2}, \qquad (2.3)$$

where μ_n is the electron low-field mobility, $v_{n,\text{sat}}$ is the saturated electron velocity, and β is a fitting parameter. Hill *et al.* [64] have measured the hole velocity in the range of 54–108 kV/cm. Böer [65] proposed an empirical expression to fit the measured hole drift velocity as a function of electric field $\mathbf{v}_p(\mathbf{E})$ in InGaAs. His expression is

$$\mathbf{v}_p(\mathbf{E}) = \frac{\mu_p v_{p,\text{sat}}\mathbf{E}}{\left(v_{p,\text{sat}}^\gamma + \mu_p^\gamma|\mathbf{E}|^\gamma\right)^{1/\gamma}}, \qquad (2.4)$$

where μ_p is the hole low-field mobility, γ is an empirical fitting parameter that depends on temperature, and $v_{p,\text{sat}}$ is the saturated hole velocity. In Fig. 2.5, we show electron and hole drift velocities as a function of the electric field given by Eqs. 2.3 and 2.4.

Hilsum [66] proposed an empirical formula to take into account the dependence of electron and hole low field mobilities, μ_n and μ_p, on the doping density,

$$\mu_{n,p} = \frac{\mu_{n_0,p_0}}{1 + \left(\dfrac{N_D + N_A}{N_{\text{ref}}}\right)^\eta}, \qquad (2.5)$$
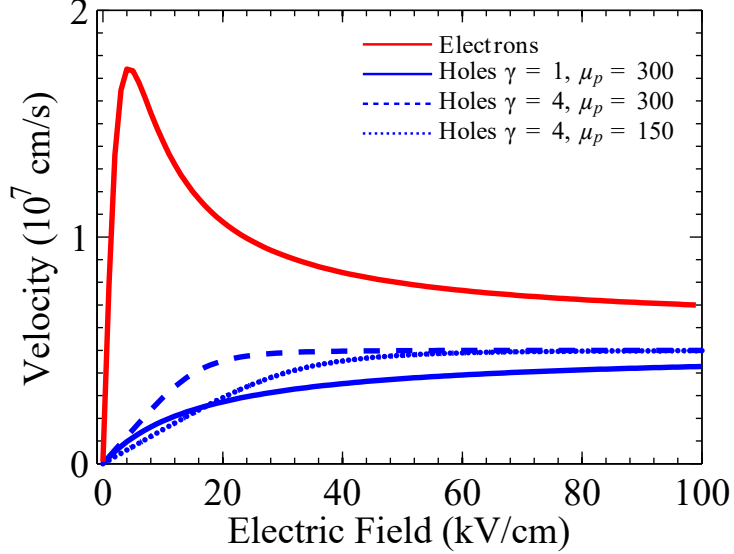
Figure 2.5: Electron and hole drift velocities in InGaAs as a function of the electric field for different fitting parameters $\gamma = 1$, 4 and hole mobilities $\mu_p = 150$ cm^2/V-s, 300 cm^2/V-s, using Eqs. 2.3 and 2.4. This figure is similar to Fig. 3 in Williams [43].

where μ_{n_0} and μ_{p_0} are electron and hole mobilities at low doping concentrations, respectively, while N_{ref} and η are empirical parameters.

Williams [43] and Böer [65, 67] gave an empirical expression for the electron diffusion coefficient as a function of electric field,

$$D_n(\mathbf{E}) = \frac{k_B T \mu_n / q}{\left[1 - 2\left(|\mathbf{E}|/E_p\right)^2 + \frac{4}{3}\left(|\mathbf{E}|/E_p\right)^3\right]^{1/4}},\tag{2.6}$$

where E_p is the electric field at which the diffusion constant peaks. In our simulations we use $E_p = 4$ kV/cm since it was the optimal choice to fit the data [55]. Williams [43] gave an expression for the hole diffusion coefficient as a function of electric field,

$$D_p(\mathbf{E}) = \frac{k_B T}{q} \frac{\mathbf{v}_p(\mathbf{E})}{\mathbf{E}}.\tag{2.7}$$

The main contribution to the recombination rate in Eq. 2.1 is the Shockley-Read-Hall (SRH) effect, which yields [68]

$$R = \frac{np - n_i^2}{\tau_p(n + n_i) + \tau_n(p + n_i)},$$

(2.8)

where τ_n, τ_p, and n_i are the electron and hole lifetimes and intrinsic carrier density respectively.

The optical generation rate in Eq. 2.1 is

$$G_{\text{opt}}(x, t) = G_c(x, t) \exp\left[-\alpha(L - x)\right],$$

(2.9)

where α is the absorption coefficient, x is distance across the device, L is the device length, and $G_c(t)$ is the generation rate coefficient as a function of time, which is given by [55]

$$G_c(t) = \frac{\alpha P_{\text{opt}}(t)}{A W_{\text{photon}}},$$

(2.10)

where $P_{\text{opt}}(t)$ is the optical power as a function of time, A is the area of the light spot, and W_{photon} is the photon energy. As a result of Eq. 2.9, the generation rate in the absorption layer depends on the location in the device as well as the material.

We will assume that the beam is Gaussian-shaped with a profile given by

$$Q(r, t) = Q_0(t) \exp[-2(r/r_0)^2],$$

(2.11)

where $Q_0(t)$ is the time-dependent incident photon flux, r is the radius, and r_0 is the spot size of the light. In the 1-D drift-diffusion model, the physical Gaussian beam profile must be approximated by a constant intensity over an effective beam area. The optical intensity is defined as the optical power per unit area. We define an effective beam diameter D_0 and an average beam intensity I_{av} such that the total power of this constant approximation is the same as the Gaussian beam, so that

$$\int_0^\infty I(r)2\pi r dr = I_{av}\pi \left(\frac{D_0}{2}\right)^2, \tag{2.12}$$

where $I(r) = I_0 \exp(-2r^2/r_0^2)$ is the intensity of the Gaussian beam and r_0 is the $1/e$ beam radius of the Gaussian beam. In the 1-D model, the diameter D_0 is a fitting parameter, and we obtain reasonable results when D_0 approximately equals $2r_0$ [55].

The total output current is the sum of the hole, electron, and displacement currents and is given by

$$J_{total} = J_n + J_p + \epsilon\frac{\partial E}{\partial t}. \tag{2.13}$$

2.3   Boundary conditions and thermionic emission

To determine a set of boundary conditions, we assume that the p- and n-contacts in Fig. 2.1 are ohmic contacts and so create no barrier to the carrier flow. Hence, the carrier densities near the contacts may be approximated by their densities in the bulk region. Assuming thermal equilibrium and vanishing space charge at

the ohmic contacts, the boundary conditions at the contacts are

$$p(0) = N_A^-, \qquad n(0) = \frac{n_i^2}{p(0)}, \tag{2.14}$$

$$n(L) = N_D^+, \qquad p(L) = \frac{n_i^2}{n(L)}, \tag{2.15}$$

where $p(0)$ and $n(0)$ are the hole and electron densities at the contact at $x = 0$, while $p(L)$ and $n(L)$ are the hole and electron densities at the contact at $x = L$, and N_A^- and N_D^+ are the ionized acceptor and donor impurity concentrations.

We set the electrostatic potential at $x = 0$ to zero, i.e., $\varphi(0) = 0$. We must then set the boundary conditions for φ at the other device interfaces. To determine the appropriate condition for $\varphi(L)$, we must take into account the load resistor. Altogether, the potential boundary conditions relate the given reverse bias V_a, the built-in potential V_{bi} [10],

$$V_{bi} = \frac{k_B T}{q} \ln\left(\frac{N_A^- N_D^+}{n_i^2}\right), \tag{2.16}$$

and the current in the photodetector to the electric field in the semiconductor region. Hence, the boundary condition for the potential becomes

$$\varphi(L) - \varphi(0) = \varphi(L) = V_a - IR_{\text{Load}} + V_{bi}, \tag{2.17}$$

where I is the output current. Since the current I is unknown at the start of any simulation, we must find it iteratively. We use the same method as Hu *et al.* [22,55].

Starting with an initial guess I_0, we determine a new current I_1 using Eq. 2.17. We then use I_1 as the next guess. We can assume that the output current I is an unknown function,

$$I = f(V_D), \tag{2.18}$$

where $V_D = \varphi(L) - \varphi(0)$ is the bias across the device. We substitute Eq. 2.17 into Eq. 2.18, and we obtain

$$F(V_D) = \frac{V_D - V_\mathrm{a} - V_\mathrm{bi}}{R_\mathrm{Load}} + f(V_D) = 0, \tag{2.19}$$

where $F(V_D)$ is the difference between the output current and the load current as a function of V_D. We then obtain the numerical derivative of $df(V_D)/dV_D$ from two initial guesses of output current I_1 and I_0,

$$\frac{df(V_D)}{dV_D} = \frac{I_1 - I_0}{V_{D1} - V_{D0}}, \tag{2.20}$$

where V_{D1} is the bias applied on the device when the output current is I_1, and V_{D0} is the bias applied on the device when the output current is I_0. We next obtain the numerical derivative of $dF(V_D)/dV_D$,

$$\frac{dF(V_D)}{dV_D} = \frac{1}{R_\mathrm{Load}} + \frac{I_1 - I_0}{V_{D1} - V_{D0}}. \tag{2.21}$$

We finally use Newton's method to solve Eq. 2.19. The next guess for V_D, V_{D2}, is
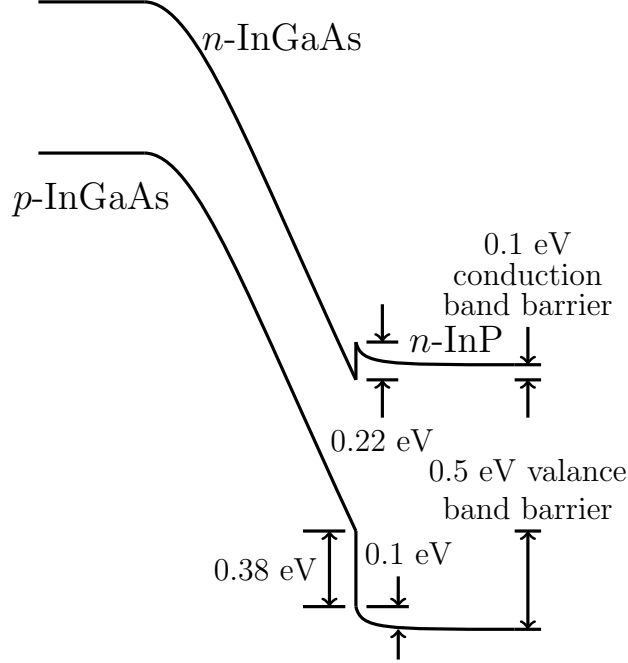
Figure 2.6: A depiction of the photodetector band diagram [55]. This figure is similar to Fig. 3.2 in Williams [43].

then

$$V_{D2} = V_{D1} - \frac{I_1 R_{\text{Load}} + V_{D1} - V_{\text{a}} - V_{\text{bi}}}{V_{D1} - V_{D0} + R_{\text{Load}}(I_1 - I_0)}(V_{D1} - V_{D0}). \qquad (2.22)$$

We iterate until the relative difference is smaller than 10^{-6}. If we further decrease the relative difference, there is no change in the simulation results.

Figure 2.6 shows the band diagram of the photodetector, where a reverse bias voltage of a few volts is applied to the device. The InGaAs/InP heterojunction depicted in Fig. 2.6 has a valence band discontinuity of 0.38 eV and a conduction band discontinuity of 0.23 eV [43, 69, 70]. The reduction in the conduction band discontinuity and the increase in the valence band discontinuity of approximately 0.1 eV is the result of the difference in the doping of the intrinsic and n-InGaAs layer. We assume that the electrons flow without restriction across the heterojunction

26

because the barrier is only 0.1 eV. However, holes are affected by the barrier of 0.5 eV. We use a thermionic emission model [71, 72] to calculate the hole current at the heterojunction. We may write

$$J_p = qv_1 p_- \exp[(W_{v1} - W_{v2})/k_B T] - qv_2 p_+, \qquad (2.23)$$

where v_1 and v_2 are respectively the hole emission velocities on the left side and right side of the heterojunction, p_- and p_+ are the hole densities on the left side and right side of the heterojunction, and W_{v1} and W_{v2} are the valance band energies on the left side and right side of the heterojunction [55].

2.4   Physical effects

2.4.1   Incomplete ionization

The ionization of impurity atoms is an important process in determining the number of free carriers in semiconductors and thus their conductivity and other physical properties. The ionization process depends on the type of impurity and the temperature, as well as the type of semiconductor. In device modeling, it is a common practice to assume complete ionization, particularly at room temperature or higher temperatures. However, the impurity ionization is often incomplete, and the conventional complete ionization approximation can introduce considerable errors in predictions of the semiconductor device behavior [73].

At low temperatures, the thermal energy within a semiconductor is not high

enough to fully ionize doping impurities introduced into InGaAs and InP. As a result, the carrier concentration will not equal the concentration of the dopant atoms. The incomplete ionization of impurities in InGaAs and InP must be considered in a similar manner to those in silicon because the impurity energy levels are relatively deep compared to the thermal energy, so that only some of the impurities are ionized [55]. Our model accounts for the incomplete ionization of doping impurities such as boron, aluminum, and nitrogen, using the following expressions [55, 74],

$$
N_D^+ = \frac{N_D}{1 + g_D \exp\left(\dfrac{E_C - E_D}{k_B T}\right) \exp\left(\dfrac{E_{Fn} - E_C}{k_B T}\right)},
$$

$$
N_A^- = \frac{N_A}{1 + g_A \exp\left(\dfrac{E_A - E_V}{k_B T}\right) \exp\left(-\dfrac{E_{Fp} - E_V}{k_B T}\right)},
$$

(2.24)

where N_D and N_A are the donor and acceptor impurity concentrations, $g_D = 2$ and $g_A = 4$ are the respective ground-state degeneracy of donor and accept impurity levels [22, 73], E_A and E_D are the acceptor and donor energy levels, E_C and E_V are the low conduction band and the high valence band energy levels, E_{Fn} and E_{Fp} are the quasi-Fermi energy levels for the electrons and holes, and T is the temperature. The energy differences in our simulations are $\Delta E_D = E_C - E_D = 5$ meV and $\Delta E_A = E_A - E_V = 25$ meV [69]. The basic variables in the drift-diffusion equations, Eq. 2.1, are the potential (or electric field), the electron concentration, and the hole concentration. Therefore, it is more convenient to rewrite Eq. 2.24 in terms of the

carrier concentration instead of the quasi-Fermi levels. We use the expressions

$$N_D^+ = \frac{N_D}{1 + g_D n/n_1}, \quad N_A^- = \frac{N_A}{1 + g_A p/p_1}, \quad (2.25)$$

where

$$\begin{aligned} n_1 &= N_C \exp\left(-\frac{\Delta E_D}{k_B T}\right), \\ p_1 &= N_V \exp\left(-\frac{\Delta E_A}{k_B T}\right), \end{aligned} \quad (2.26)$$

and

$$\begin{aligned} n &= N_C \exp\left(\frac{E_{Fn} - E_C}{k_B T}\right), \\ p &= N_V \exp\left(-\frac{E_{Fp} - E_V}{k_B T}\right). \end{aligned} \quad (2.27)$$

2.4.2 Impact ionization

At high electric fields, a hot electron/hole, which has a high energy due to the applied field in comparison with the band gap, can collide with an electron/hole in the valence/conduction band *via* the Coulomb interaction and knock it into the conduction/valence band, creating another pair of mobile charge carriers. The initial electron/hole must provide enough energy to bring the valence-band/conduction-band electron/hole into the conduction/valence band [75]. Thus, the initial electron should have energy slightly larger than the band gap (around 1 eV for $In_{0.53}Ga_{0.47}As$ [76]). With a strong electric field and an acceleration region with a sufficiently long length, this mechanism can lead to avalanche breakdown [77]. In the *p-i-n* photodetectors that we are considering, the acceleration lengths are too small to lead to avalanche breakdown since electrons leave the acceleration region

too quickly. Nonetheless, impact ionization can lead to an important increase in the electron and hole densities [55]. The electron and hole generation rate due to impact ionization G_{ii} can be described as [78]

$$G_{\mathrm{ii}} = \alpha_n \frac{|\mathbf{J}_n|}{q} + \alpha_p \frac{|\mathbf{J}_p|}{q}, \qquad (2.28)$$

where α_n and α_p are the impact ionization coefficients of the electrons and holes, respectively. We calculate their values using the formulae [69, 78]

$$\begin{aligned} \alpha_n &= A_n \cdot \exp\left[-\left(\frac{B_n}{|\mathbf{E}|}\right)^m\right], \\ \alpha_p &= A_p \cdot \exp\left[-\left(\frac{B_p}{|\mathbf{E}|}\right)^m\right], \end{aligned} \qquad (2.29)$$

where A_n, B_n, A_p, and B_p are experimentally-determined parameters [69, 70]. The exponent m is set equal to 1.05. The values that we use, shown in Table 2.1 for InGaAs, are modified slightly from the values in [69, 70] in order to obtain harmonic powers that are consistent with experiments. However, all values fall within the range of experimental error.

2.4.3 Franz-Keldysh effect

When the photon energy of the incident optical light is close to the band edge of the InGaAs absorber, the Franz-Keldysh effect must be taken into account [79]. The Franz-Keldysh effect leads to oscillations in the carrier transition probability for energies that are greater than the band gap and tunneling of the electron state

Table 2.1: Material parameters at 300 K that we used in our simulations

Parameter	InP	In$_{0.53}$Ga$_{0.47}$As
E$_g$ (eV)	1.35	0.71
χ (eV)	4.38	4.6
ϵ_r (eV)	12.4	13.7
ΔE_D (eV)	0.007	0.005
ΔE_A (eV)	0.025	0.025
$\tau_{n,p}$ in i-region (ns)	10	10
$\tau_{n,p}$ in doped region (ps)	100	100
A_n (cm^{-1})	1.12 $\times 10^7$	6.64$\times 10^7$
B_n (V/cm)	3.11 $\times 10^6$	2$\times 10^6$
A_p (cm^{-1})	4.79 $\times 10^6$	9.34$\times 10^7$
B_p (V/cm)	2.55 $\times 10^6$	2.26$\times 10^6$
β (cm^2/V^2)	8×10^{-8}	4×10^{-8}
γ	1	1
α (μm^{-1})	$-$	1.45
$v_{n,\text{sat}}$ (cm/sec)	6.7×10^6	1.53×10^7
$v_{p,\text{sat}}$ (cm/sec)	5×10^6	6.39×10^6
m_n^*/m_0	0.08	0.041
m_p^*/m_0	0.64	0.59

into the forbidden band due to band-bending below the band gap in the presence of an applied electric field.

The expression for the absorption coefficient due to the Franz-Keldysh effect [55, 80] is

$$\alpha = \left(\frac{2\pi e^2}{m_e{}^2 c \eta' \omega} \right) \left(\frac{|\langle c\mathbf{k_0}|\mathbf{e} \cdot \mathbf{p}|v\mathbf{k_0}\rangle|^2}{A^2 \pi^2 f^{1/2} \chi} \right), \tag{2.30}$$

where e is the magnitude of the electron charge (here positive), m_e is the electron mass, η' is the real part of the refractive index at the frequency ω, c is the speed of light, $\mathbf{k_0}$ is the point in the $\mathbf{k}$-space where the minimum energy gap between the conduction band c and the valence band v occurs, $\mathbf{e} \cdot \mathbf{p}$ denotes the matrix elements of the transition, A is a normalization constant, f is the field strength, and χ is a constant that can be calculated by solving the effective mass equation [65].

Chapter 3

Modeling the impulse response and the phase noise

3.1   One-dimensional computational model

We use the same one-dimensional model that Hu *et al.* [22,55] have presented.
We use the implicit Euler method to discretize the drift-diffusion equations in time
t for numerical computation. We use second-order finite differences to discretize
the spatial dimension x. Figure 3.1 schematically shows the mesh that we use to
discretize the x-dimension. We define the hole density p, the electron density n,
and the electric potential φ, at the integer points in the mesh that are indexed by
$l = 1, 2, ..., N$. The current and electric field are defined at intermediate points that
are indexed by $l = 3/2, 5/2, ..., N - 1/2$. We define the distance between the integer
points l and $l + 1$ as h_l, and the distance between the intermediate points $l - 1/2$
and $l + 1/2$ as h'_l. We set

$$h'_l = \frac{h_{l-1} + h_l}{2}. \tag{3.1}$$

We approximate the electric field at the half-integer points in the mesh as

$$E_{l+1/2} = -\left(\frac{\psi_{l+1} - \psi_l}{h'_l}\right), \tag{3.2}$$
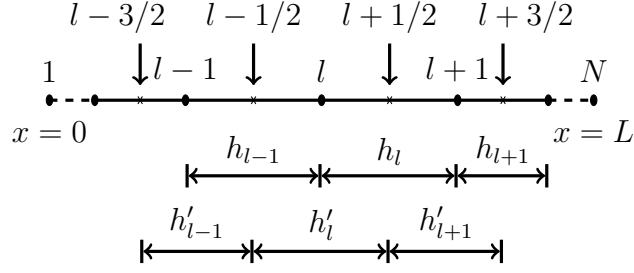
Figure 3.1: Numerical mesh used for the finite difference spatial discretization of the 1-D drift-diffusion equation.

where ψ_l is the potential at mesh-point l, and we approximate $\partial p/\partial x$ and $\partial n/\partial x$ at

the half-integer points as

$$
\begin{aligned}
\left.\frac{\partial p}{\partial x}\right|_{l+1/2} &= \left(\frac{p_{l+1} - p_l}{h'_l}\right), \\
\left.\frac{\partial n}{\partial x}\right|_{l+1/2} &= \left(\frac{n_{l+1} - n_l}{h'_l}\right).
\end{aligned}
\tag{3.3}
$$

We calculate the currents at the half-integer points by discretizing Eq. 2.2 to obtain

$$
\begin{aligned}
\mathbf{J}_{p,l+1/2} &= q p_{l+1/2} \mathbf{v}_{p,l+1/2}(\mathbf{E}) - q D_{p,l+1/2}\left(\frac{p_{l+1} - p_l}{h_l}\right), \\
\mathbf{J}_{n,l+1/2} &= q n_{l+1/2} \mathbf{v}_{n,l+1/2}(\mathbf{E}) + q D_{n,l+1/2}\left(\frac{n_{l+1} - n_l}{h_l}\right),
\end{aligned}
\tag{3.4}
$$

where $p_{l+1/2} = (p_{l+1} + p_l)/2$, $n_{l+1/2} = (n_{l+1} + n_l)/2$, $D_{n,l+1/2}$ and $D_{p,l+1/2}$ are the

electron and hole diffusion coefficients at the point $l + 1/2$, and $\mathbf{v}_{n,l+1/2}$ and $\mathbf{v}_{p,l+1/2}$

are the electron and hole drift velocities at the point $l + 1/2$. Using this mesh, we

34
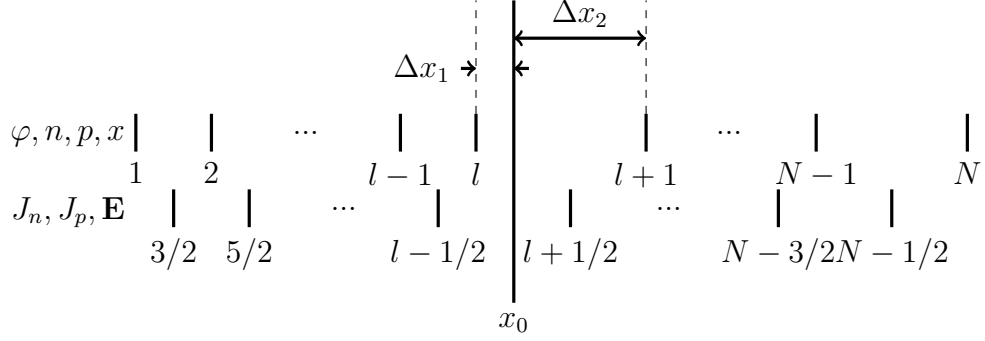
Figure 3.2: Discretization scheme that we used in our device model at a heterojunction interface.

discretize Eq. 2.1 so that it becomes

$$
\frac{n_l^{i+1} - n_l^i}{\delta t} = \frac{1}{q} \frac{J_{n,l+1/2}^{i+1} - J_{n,l-1/2}^{i+1}}{h_l'} + G_l^{i+1} + G_{i,l}^{i+1} - R_l^{i+1},
$$

$$
\frac{p_l^{i+1} - p_l^i}{\delta t} = -\frac{1}{q} \frac{(J_p)_{l+1/2}^{i+1} - (J_p)_{l-1/2}^{i+1}}{h_l'} + G_l^{i+1} + G_{i,l}^{i+1} - R_l^{i+1}, \qquad (3.5)
$$

$$
\frac{1}{h_l'} \left[\frac{\varphi_{l+1}^{i+1} - \varphi_l^{i+1}}{h_l} - \frac{\varphi_l^{i+1} - \varphi_{l-1}^{i+1}}{h_{l-1}} \right] = -\frac{q}{\epsilon} \left(N_{Dl}^+ - N_{Al}^- + p_l^{i+1} - n_l^{i+1} \right),
$$

where n_l^{i+1} and p_l^{i+1} are the electron and hole densities at the point l and time-step $i+1$, respectively, G_l^{i+1} is the generation rate at the point l and time-step $i+1$, R_l^{i+1} is the recombination rate at the point l and time-step $i+1$, φ_l^{i+1} is the electrostatic potential at the point l and time-step $i+1$, and finally N_{Dl}^+ and N_{Al}^- are the ionized donor and acceptor doping densities at the point l.

At the heterojunction interface x_0 that we show in Fig. 3.2, the discretization is different due to a discontinuity in the hole density. Figure 3.2 shows a schematic illustration of the discretization in this case. We treat the drift-diffusion equation as a differential equation in the hole density, assuming that all other variables are

35

constant across the grid, and we integrate across the grid element to obtain the hole density at the interface x_0. The integration is done in two steps, first from x_l to x_0 and then from x_0 to x_{l+1}, as illustrated in Fig. 3.2. The drift-diffusion equation for holes, which is obtained by inserting Eqs. 2.4 and 2.7 into Eq. 2.2, can be written as a differential equation in the hole density,

$$\frac{\partial p}{\partial x} = \frac{qE}{k_B T} p - \frac{E J_p}{k_B T v_p}. \tag{3.6}$$

Integrating from x_l to x_0 yields

$$
p_{x_0^-} = p_l \exp\left[\frac{qE_{l+1/2}}{k_B T}\Delta x_1\right]
$$
$$
- \frac{J_{p,l+1/2}}{q v_{p,l+1/2}}\left\{1 - \exp\left[\frac{qE_{m+1/2}}{k_B T}\Delta x_1\right]\right\}. \tag{3.7}
$$

The integral from x_0 to x_{m+1} yields:

$$
p_{x_0^+} = p_{l+1}\exp\left[-\frac{qE_{l+1/2}}{k_B T}\Delta x_2\right]
$$
$$
- \frac{J_{p,l+1/2}}{q v_{p,l+1/2}}\left\{1 - \exp\left[-\frac{qE_{l+1/2}}{k_B T}\Delta x_2\right]\right\}. \tag{3.8}
$$

We also take into account thermionic emission at the heterojunction interface [71, 72]. In Fig. 3.3, we illustrate the possible barriers for holes. When holes move from a material with a higher valance band energy to a lower valance band energy, as shown on the left of Fig. 3.3, the heterojunction is a barrier to holes. This case occurs in the structure that we study. When holes move from a material with a lower valance band energy to a material with a higher valance band energy, as
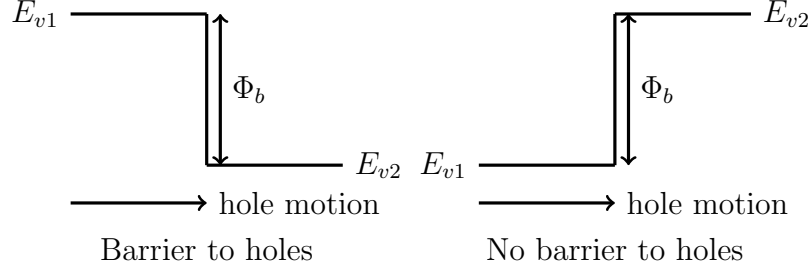
Figure 3.3: Schematic illustration of the boundary conditions used at the heterojunction.

shown on the right of Fig. 3.3, then holes move freely through the heterojunction. This kind of heterojunction is not a barrier to holes. This case does not appear in the structure that we study. Using Eq. 2.23, the current at the heterojunction can be written as

$$J_p(l + 1/2) = qv_1 p(x_0^-) \exp[(E_{v1} - E_{v2})/k_B T] - qv_2 p(x_0^+). \tag{3.9}$$

Inserting Eqs. 3.7 and 3.8 into Eq. 3.9 and rearranging yields

$$J_p(l + 1/2) = qv_p(l + 1/2) \frac{A - B}{1 + C - D}, \tag{3.10}$$

where A, B, C, and D are given by [22, 55]

$$A = p(l) \exp\left[\frac{qE(l + 1/2)\Delta x1 + E_{v1} - E_{v2}}{k_B T}\right], \tag{3.11}$$

$$B = p(l + 1) \exp\left[-\frac{qE(l + 1/2)\Delta x_2}{k_B T}\right], \tag{3.12}$$

$$C = \left\{ 1 - \exp\left[\frac{qE(l + 1/2)\Delta x_1}{k_B T} \right] \right\} \exp\left[\frac{E_{v1} - E_{v2}}{k_B T} \right], \qquad (3.13)$$

$$D = 1 - \exp\left[-\frac{qE(l + 1/2)\Delta x_2}{k_B T} \right]. \qquad (3.14)$$

We have assumed that the electric field and the hole velocity remain constant across the heterojunction interface.

3.2 Impulse response of the p-i-n and MUTC photodetectors

To calculate the impulse response, we first calculate the steady state output current. We then perturb the generation rate by ΔG_{opt} and calculate the impulse response due to the perturbation ΔG_{opt}. We use

$$\Delta G_{\text{opt}} = r G_{\text{opt}} \operatorname{rect}\left(\frac{t}{\tau} \right), \qquad (3.15)$$

where G_{opt} is the optical generation rate, r is the perturbation coefficient, $\operatorname{rect}(t)$ is the rectangular function

$$\operatorname{rect}(t) = \begin{cases} 0, & t < 0 \\ 1, & 0 < t < 1 \\ 0, & 1 < t \end{cases}$$

t is time, and τ is the impulse width. We set $\tau = 10$ fs, which we verified produces reliable results for the impulse response for times that are larger than 40 fs. We use $r = 10^{-1}$, which we have verified is sufficiently small that no nonlinear effects occur,
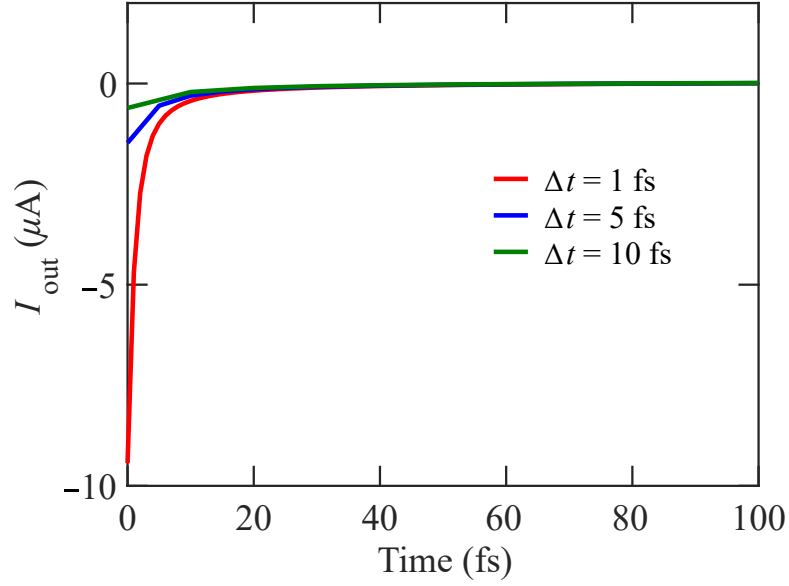
Figure 3.4: Output current I_{out} of the MUTC photodetector as a function of time for different time meshes (Δt).

while it is large enough to avoid roundoff errors. The normalized impulse response $h(t)$ is then given by

$$h(t) = \frac{\Delta I_{\text{out}}(t)}{\int_0^\infty \Delta I_{\text{out}}(t)dt}, \tag{3.16}$$

so that $\int_0^\infty h(t)dt = 1$, where $\Delta I_{\text{out}}(t)$ is the change in the output current due to the impulse.

We note that $h(t)$ as defined here includes the combined effect of a finite optical pulse duration and the electrical response to the optical pulse. This definition is consistent with Refs. [46] and [47]. In order to verify that our results are independent of the choice of τ and r, we ran numerical tests in which we allowed these quantities to vary.
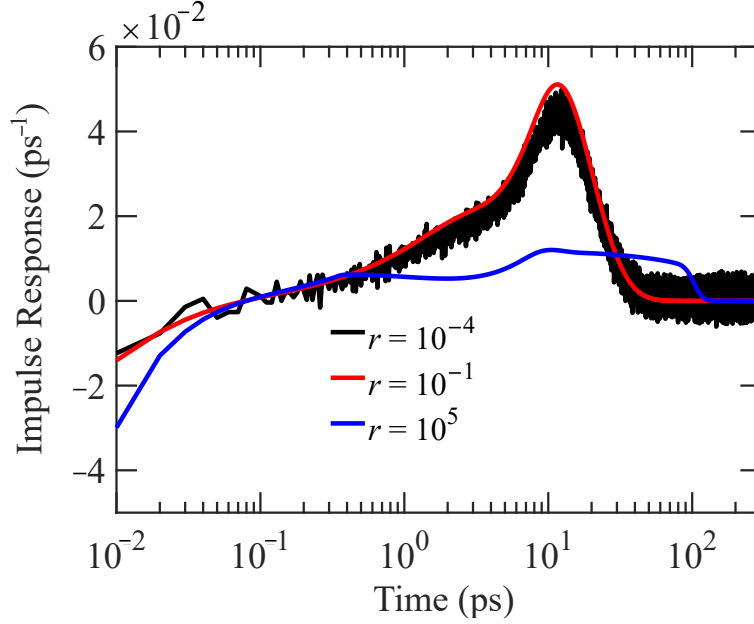
Figure 3.5: Normalized impulse response of the MUTC photodetector as a function of time for different values of r.

In Fig. 3.4, we show output current (I_{out}) of the MUTC photodetector as a function of time t for different time meshes (Δt). The results are almost identical for $t > 20$ fs, indicating that the frequency dependence will be reliable up to frequencies of 50 THz, which is far beyond the limit of 10–50 GHz at which experiments indicate that the device can no longer respond. Similar results hold for the p-i-n photodetector.

In Fig. 3.5, we show how the calculated impulse response varies for the MUTC device as r varies. When $r = 10^{-4}$, computational errors degrade the impulse response, leading to rapid fluctuations. When $r = 10^{5}$, nonlinearity becomes important, and the impulse response is distorted. For $10^{-3} < r < 10^{4}$, the impulse response is almost identical to the impulse response when $r = 10^{-1}$, which we have shown in the figure. While it is possible in principle to linearize Eqs. 2.1–2.9 about the sta-

tionary solution and avoid this issue, the equations that we obtain with this direct

linearization are sufficiently complex that there is no advantage in doing so.

3.3   Calculation of the phase noise in photodetectors

In this section, we calculate the phase noise of the MUTC photodetector. We

first calculate the timing jitter using the impulse response function, and we then use

the timing jitter to calculate the phase noise.

We define the finite-time Fourier transform,

$$\mathscr{F}_T\{x(t)\} \equiv \frac{1}{2T} \int_{-T}^{T} x(t) \exp(-j2\pi ft)\mathrm{d}t. \tag{3.17}$$

We next write

$$
\begin{aligned}
\mathscr{F}_T\{i(t)\} &= \frac{1}{2T} \int_{-T}^{T} i(t) \exp(-j2\pi ft)\mathrm{d}t \\
&= \frac{1}{2KT_R} \sum_{k=-K}^{K-1} \int_{0}^{T_R} i(t + kT_R) \exp[-j2\pi f(t + kT_R)]\mathrm{d}t,
\end{aligned}
\tag{3.18}
$$

where $i(t)$ is the output current, T_R is the repetition time between optical pulses,

and $T = KT_R$. If we let $i_k(t) = i(t + kT_R)$, so that $i_k(t)$ is the k-th current output

pulse, we obtain

$$\mathscr{F}_T\{i(t)\} = \frac{1}{2KT_R} \sum_{k=-K}^{K-1} \int_{0}^{T_R} i_k(t) \exp(-j2\pi ft)\mathrm{d}t. \tag{3.19}$$

For the n-th harmonic of the current, we obtain

$$R_n + jQ_n = \frac{1}{2KT_R} \sum_{k=-K}^{K-1} \int_0^{T_R} i_k(t) \left[\cos\left(2\pi n f_r t\right) - j \sin\left(2\pi n f_r t\right)\right] \mathrm{d}t, \qquad (3.20)$$

where R_n and Q_n are in-phase and quadrature components of the n-th harmonic. We also define the ensemble average $\langle c_k(t)\rangle$ for any quantity $c_k(t)$ as

$$\langle c_k(t)\rangle \equiv \lim_{K \to \infty} \frac{1}{2K} \sum_{k=-K}^{K-1} c_k(t). \qquad (3.21)$$

It is useful to shift the time to remove the quadrature component to good approximation. To do that, we write

$$R_n + jQ_n = \frac{1}{2KT_R} \sum_{k=-K}^{K-1} \int_0^{T_R} i_k(t) \left\{\cos\left[\frac{2\pi n}{T_R} (t - t_c)\right] - j \sin\left[\frac{2\pi n}{T_R} (t - t_c)\right]\right\} \mathrm{d}t,$$

$$(3.22)$$

where t_c is the central time of the output current, which is implicitly defined by the relation

$$Q_n = \frac{1}{T_R} \int_0^{T_R} \langle i_k(t)\rangle \sin\left[\frac{2\pi n}{T_R} (t - t_c)\right] \mathrm{d}t = 0. \qquad (3.23)$$

We next define

$$\Phi_n = \frac{-j \sum_{k=-K}^{K-1} \int_0^{T_R} i_k(t) \sin\left[\frac{2\pi n}{T_R} (t - t_c)\right] \mathrm{d}t}{\sum_{k=-K}^{K-1} \int_0^{T_R} i_k(t) \cos\left[\frac{2\pi n}{T_R} (t - t_c)\right] \mathrm{d}t} = 0. \qquad (3.24)$$

Although we have $\Phi_n = 0$, the separate phase contribution of each comb pulse to Φ_n will be non-zero. We have $\Phi_n = \sum_k \Phi_{kn}$ and $Q_n = \sum_k Q_{kn}$, where

$$\Phi_{kn} = \frac{Q_{kn}}{R_n} = \frac{-j \int_0^{T_R} i_k(t) \sin\left[\frac{2\pi n}{T_R}(t - t_c)\right] \mathrm{d}t}{\int_0^{T_R} i_k(t) \cos\left[\frac{2\pi n}{T_R}(t - t_c)\right] \mathrm{d}t}. \tag{3.25}$$

We next find

$$\Phi_{kn}^2 = \frac{\int_0^{T_R} \int_0^{T_R} i_k(t) i_k(u) \sin\left[\frac{2\pi n}{T_R}(t - t_c)\right] \sin\left[\frac{2\pi n}{T_R}(u - t_c)\right] \mathrm{d}t \mathrm{d}u}{\left\{\int_0^{T_R} i_k(t) \cos\left[\frac{2\pi n}{T_R}(t - t_c)\right] \mathrm{d}t\right\}^2}. \tag{3.26}$$

We may assume that the electrons in each current pulse are Poisson-distributed [81]. This assumption may seem surprising at first since the photodetectors of interest to us operate in a nonlinear regime. However, the electrons only interact through the electric field that they collectively create. Due to the large number of electrons that create this field, a mean-field approximation is valid, and the arrival time of the electrons is nearly independent. Given the assumption that the current pulses are Poisson-distributed, we find

$$\langle i_k(t) i_k(u) \rangle - \langle i_k(t) \rangle \langle i_k(u) \rangle = h(t) e^2 N_{\text{tot}} \delta(t - u). \tag{3.27}$$

Taking the ensemble average of Eq. 3.26, substituting Eq. 3.27 into this ensemble-averaged equation, and using Eq. 3.23, we find

$$\langle \Phi_n^2 \rangle = \frac{1}{N_{\text{tot}}} \frac{\int_0^{T_R} h(t) \sin^2\left[2\pi n(t - t_c)/T_R\right] \mathrm{d}t}{\left\{\int_0^{T_R} h(t) \cos\left[2\pi n(t - t_c)/T_R\right] \mathrm{d}t\right\}^2}, \tag{3.28}$$

where $\langle \Phi_n^2 \rangle$ is the mean-square phase fluctuation and N_{tot} is the total number of electrons in the photocurrent. Increasing the photocurrent for a given impulse response $h(t)$ decreases the phase noise. In the limit of short optical pulse durations ($\lesssim 500$ fs), we find that $\langle \Phi_n^2 \rangle$ tends to a non-zero constant, which is given by

$$\langle \Phi_n^2 \rangle = \frac{1}{N_{\text{tot}}} \frac{\int_0^{T_R} h_e(t) \sin^2 \left[2\pi n(t - t_c)/T_R \right] \mathrm{d}t}{\left\{ \int_0^{T_R} h_e(t) \cos \left[2\pi n(t - t_c)/T_R \right] \mathrm{d}t \right\}^2}, \tag{3.29}$$

where $h_e(t)$ is the electronic impulse response of the device. From Eq. 3.29, we infer that phase noise is reduced for a fixed pulse energy by designing the photodetector so that its impulse response tail is as small as possible. We stress that this analysis applies to any photodetector, not only MUTC photodetectors.

Using Eq. 3.29, we may calculate the phase noise of MUTC photodetectors.

Chapter 4

Impulse response and phase noise simulation results for the *p-i-n* and MUTC photodetectors

4.1 Simulation results at steady state for the *p-i-n* photodetector

Here, we present the simulation results for the *p-i-n* photodetector that we study (see Fig. 2.1) at steady state. Figure 4.1 shows the electric field distribution inside the *p-i-n* photodetector, and Fig. 4.2 shows the electron and hole densities.
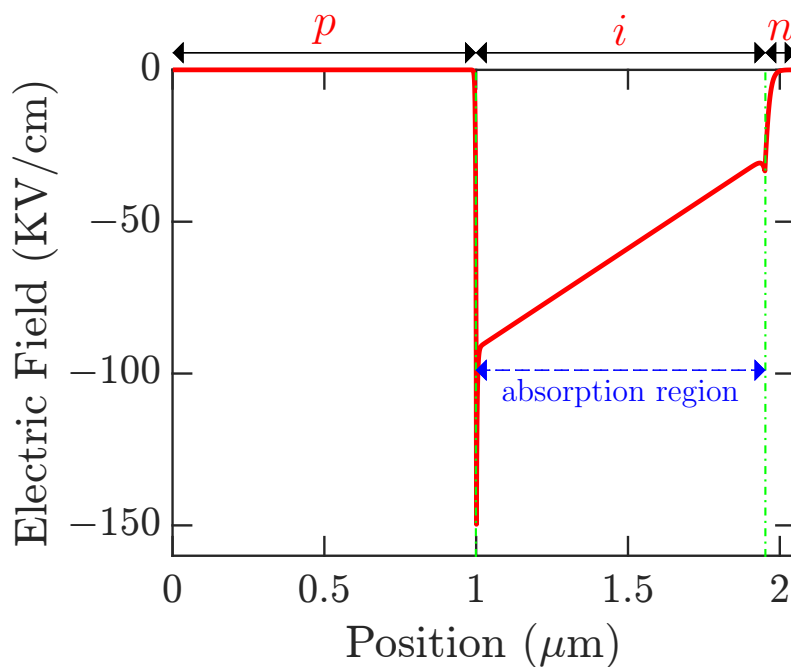
Figure 4.1: Electric field distribution at steady-state inside the *p-i-n* photodetector.
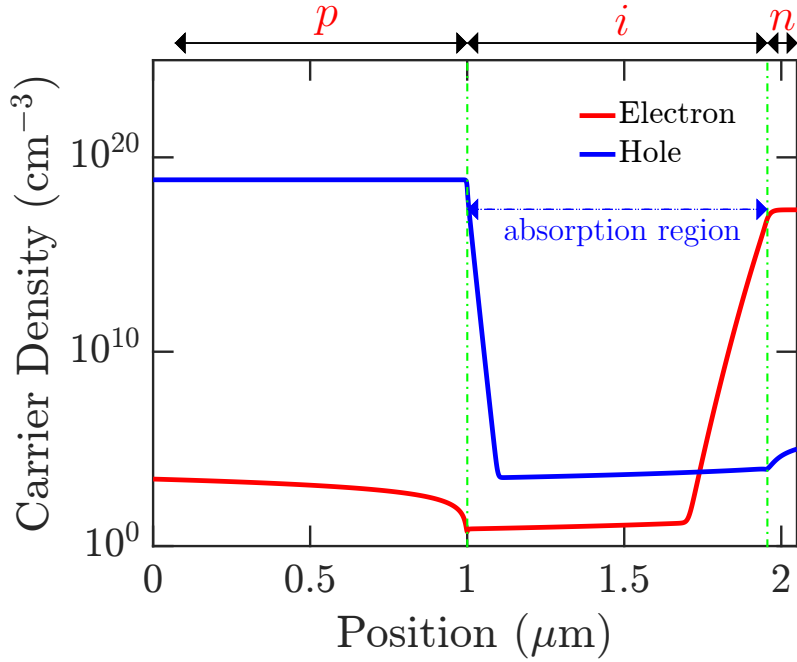
Figure 4.2: Density of electrons (red) and holes (blue) at steady-state inside the *p-i-n* photodetector.

4.2 Impulse response of the *p-i-n* photodetector

After we calculated the steady-state parameters, we perturbed the optical generation rate by ΔG_{opt} and we then calculated the impulse response due to this perturbation using the method that we described earlier in Sec. 2.5. Figure 4.3 shows the impulse response of the *p-i-n* photodetector as a function of time, normalized to 1, *i.e.*,

$$\int_0^\infty h(t)dt = 1. \tag{4.1}$$

In this figure, the black curve shows the total current, the red curve shows the electron current, the blue curve shows the hole current, and the dashed green curve
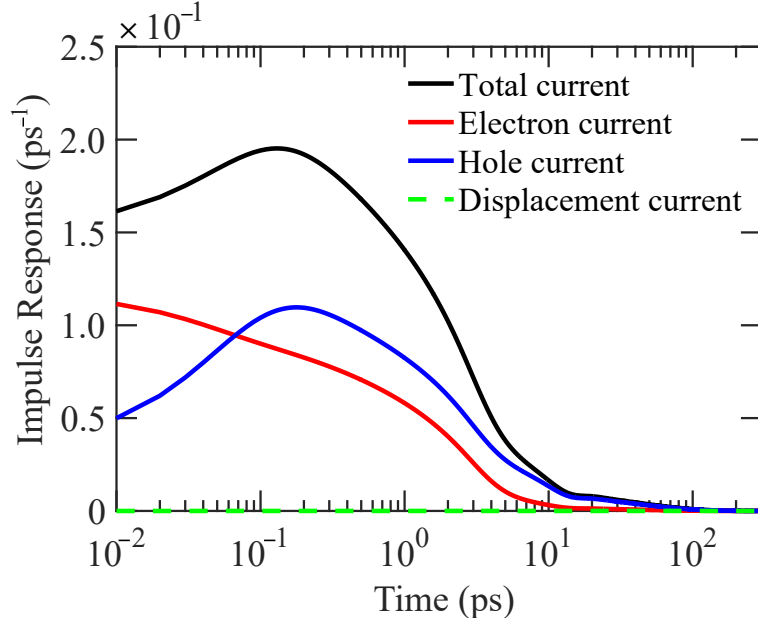
Figure 4.3: Impulse response of the *p-i-n* photodetector.

shows the displacement current. To calculate the total current, we add the electron, hole, and displacement currents. At very early times (first 70 fs), the electron current dominates the total current, but at later times the hole current dominates the total current. The displacement current is always negligible.

In Fig. 4.4, we show the corresponding power spectral density $|H(f)|^2$, where

$$H(f) = \int_{-\infty}^{\infty} h(t) \exp(-2\pi jft)dt. \tag{4.2}$$

4.3   Simulation results at steady state for the MUTC photodetector

In Figs. 4.5 and 4.6, we show the electric field and carrier distributions at steady state inside the MUTC photodetector. The behavior as a function of position is significantly more complex than it is for the *p-i-n* photodetector, due to

47
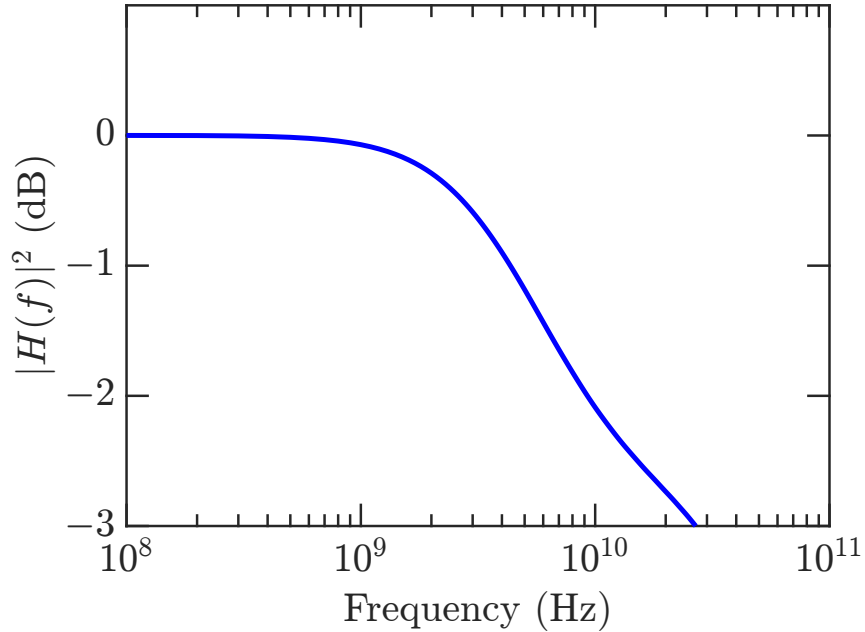
Figure 4.4: Fourier transform of the impulse response of the *p-i-n* photodetector.

the more complex structure. A clear difference in the hole density is observed between the two structures. In the *p-i-n* photodetector, the hole density decreases by two orders of magnitude at the transition between the *p*-region and the intrinsic region. By contrast, the hole density decreases by ten orders of magnitude in the MUTC photodetector. It is the virtual elimination of holes as current carriers that is responsible for the faster response of this device.

4.4 Impulse response of the MUTC photodetector

In Fig. 4.7, we show the impulse response of the MUTC photodetector as a function of time. We used the optical pulses that are defined in Eq. 3.15. In contrast to the *p-i-n* photodetector, we see that the displacement current cannot
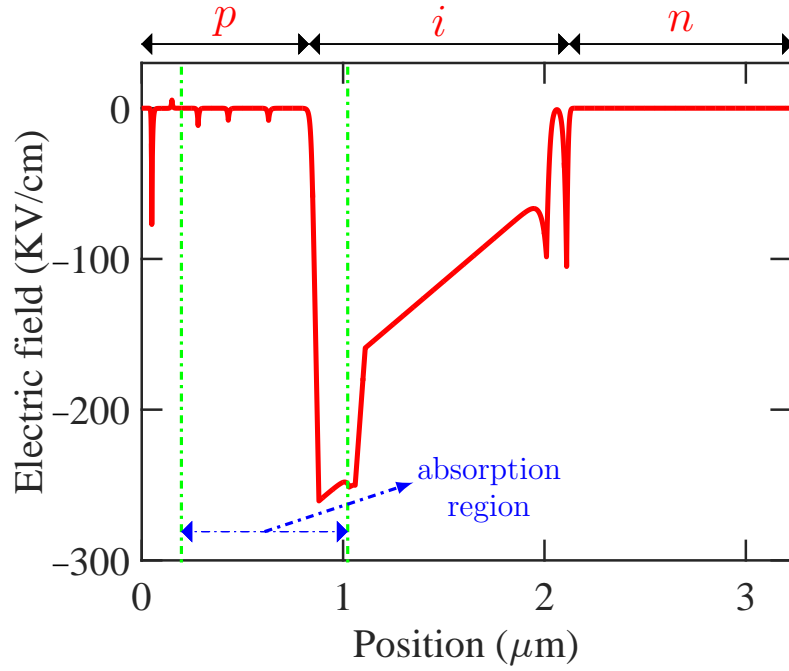
Figure 4.5: Electric field distribution at steady state inside the MUTC photodetector with $I_\text{out} = 15$ mA and $V_\text{bias} = 16$ V.
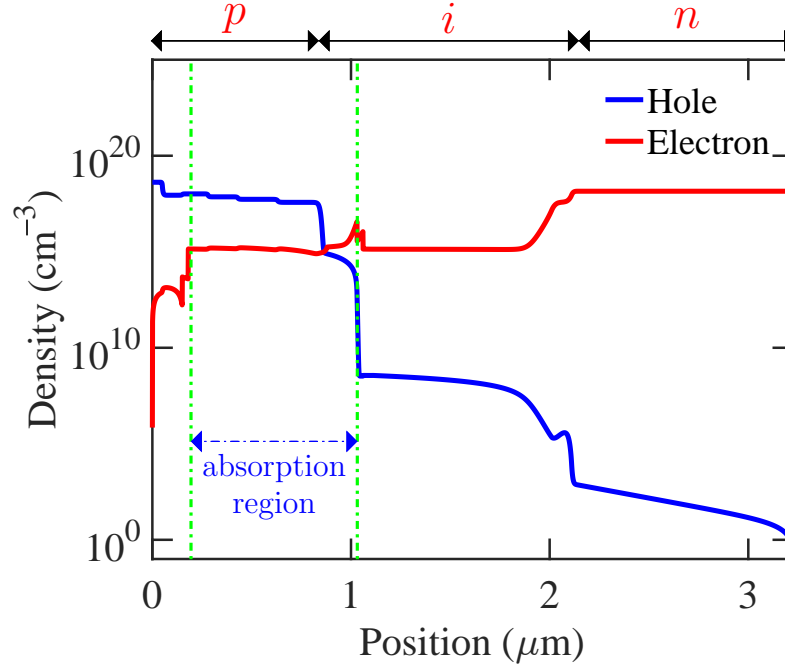
Figure 4.6: Density of electrons (red) and holes (blue) at steady state inside the MUTC photodetector with $I_\text{out} = 15$ mA and $V_\text{bias} = 16$ V.

49
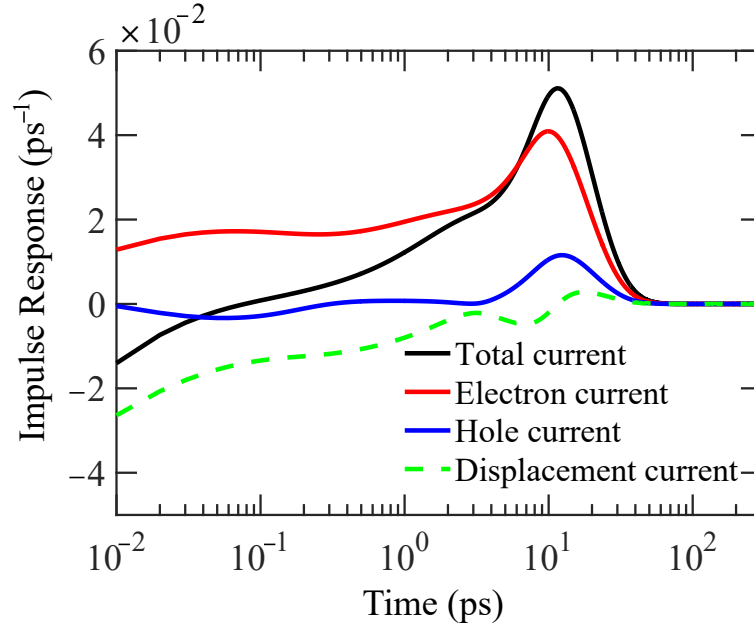
Figure 4.7: Impulse response of the MUTC photodetector.
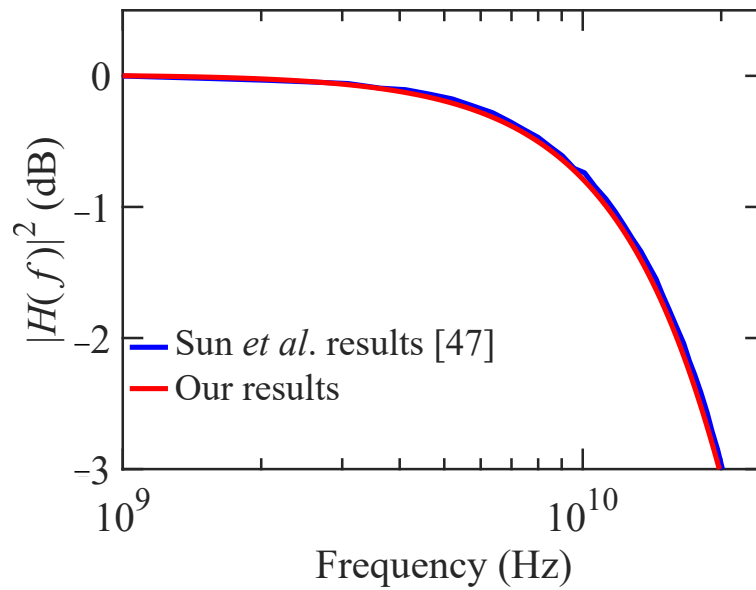
Figure 4.8: Power spectral density of the MUTC photodetector.

be neglected, and it dominates the total current for the first 50 fs. Thereafter, the electron current dominates at all times, in sharp contrast to the *p-i-n* photodetector, for which the hole current dominates beyond 70 fs. Figure 4.8 shows the power

spectral density of the MUTC photodetector. We compare this result to an average of the power spectral density that Sun *et al.* [47] reported from five realizations of their Monte Carlo simulations. They computed their power spectral density using an impulse with a duration of 15 ps. We computed $h(t)$ and $|H(f)|^2$ using the same impulse duration. We have found that when the optical pulse duration is less than about 500 fs, the impulse response tends to a finite limit $h_e(t)$ that represents the electronic response and has a mean-square pulse duration ~ 90 ps^2.

The calculation of the impulse response using the drift-diffusion equations is far more rapid computationally than is its calculation using Monte Carlo simulations. Hence, it is possible to do a broad parameter study. In Fig. 4.9, we compare the device diameter, beam diameter, steady state output current, and the voltage bias.

We compare these results to the average of the power spectral density that Sun *et al.* [47] reported from five realizations of their Monte Carlo simulations. The difference is small in all cases.

4.5   Phase noise in the MUTC photodetectors

In this chapter, we calculate the phase noise of the MUTC photodetector and compare our results to the Monte Carlo simulation results of Sun *et al.* [47] and to the experimental results of Quinlan *et al.* [46]. Using Eq. 3.29, we calculate the phase noise of the MUTC photodetector. Figure 4.10 shows the phase noise of the MUTC photodetector as a function of offset frequency for three different optical pulse widths.
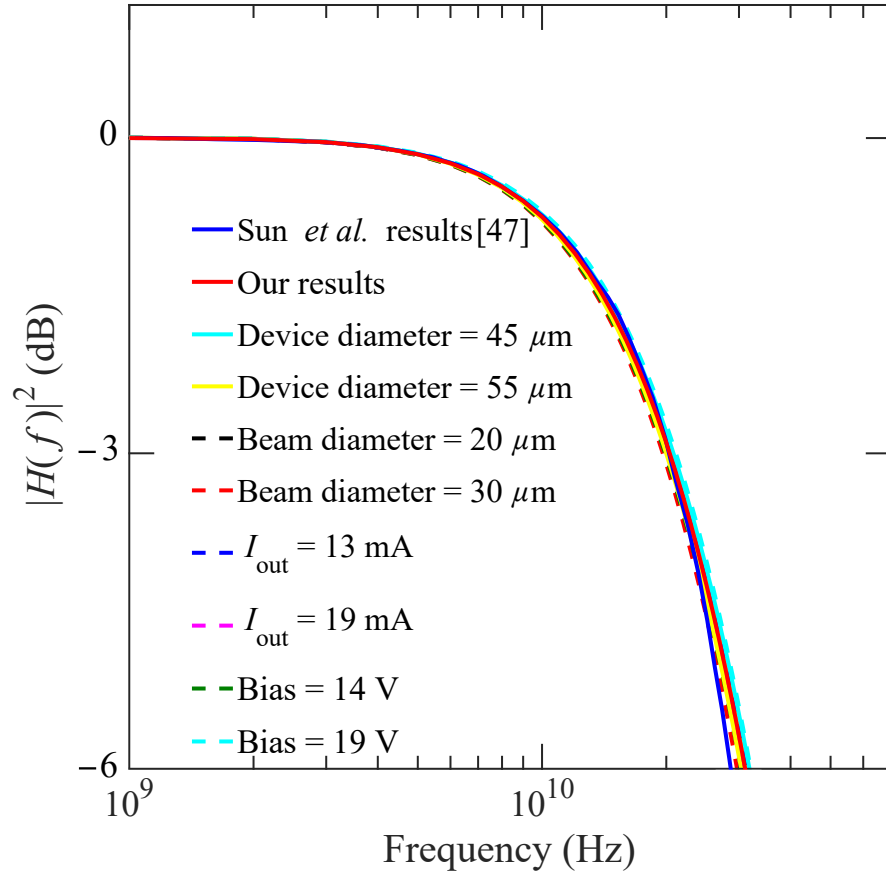
Figure 4.9: Power spectral density of the MUTC photodetector for different parameters.

We show the phase noise deviation from the long pulse limit as a function of the optical pulse width in Fig. 4.11.

As shown in Figs. 4.10 and 4.11, we obtain good agreement with both experimental and Monte Carlo simulation results. Here, we considered a range of average currents between 14 mA and 18 mA and bias voltages between 15 V and 21 V, which correspond to the ranges in the experiments of Quinlan et al. [46]. In Fig. 4.11, we show how the phase noise deviation from the long-pulse limit depends on the bias
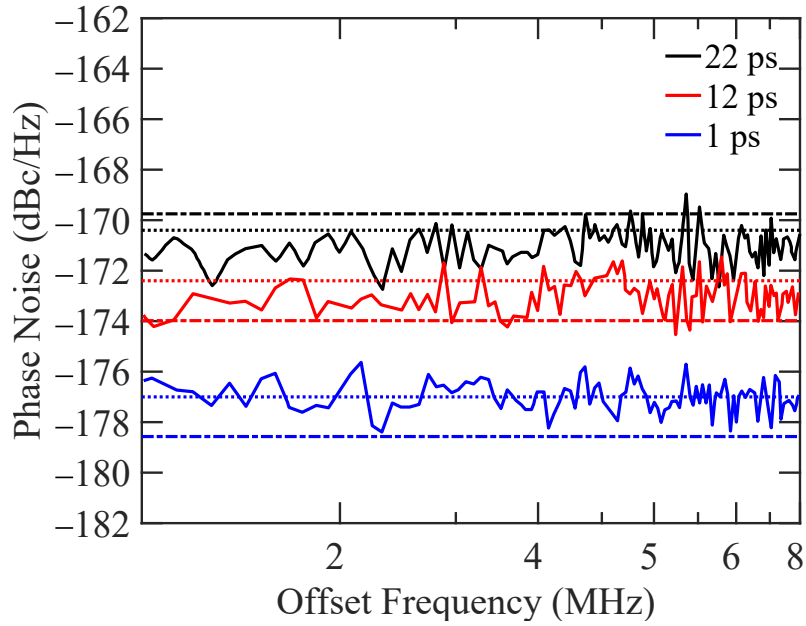
Figure 4.10: Phase noise of the MUTC photodetector as a function of offset frequency for three different optical pulse widths. Dot-dashed lines are experimental results from Ref. [46]; solid lines are Monte Carlo simulation results from Ref. [47]; dotted lines are our simulation results.
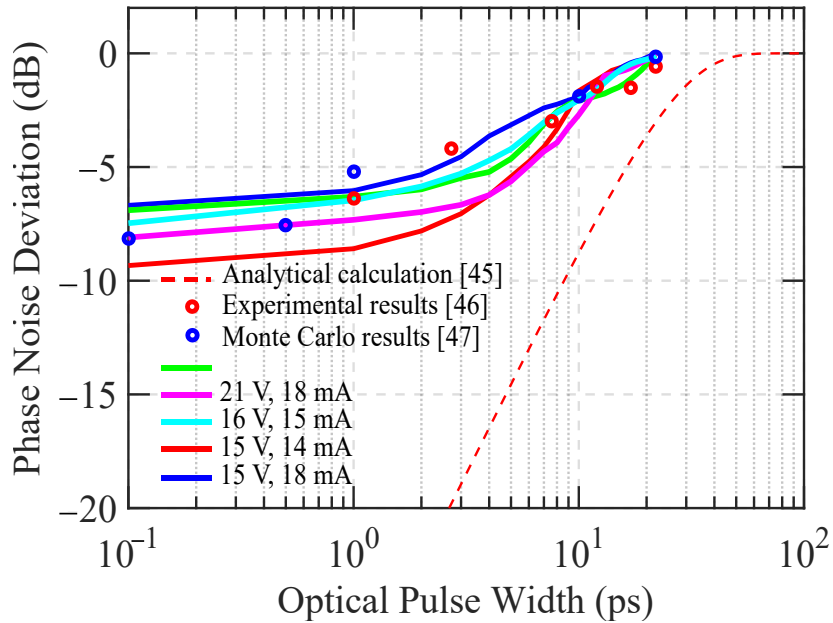
Figure 4.11: Phase noise deviation from the long pulse limit.

voltage and output current for the MUTC device considered earlier in Refs. [46] and [47]. The computational rapidity of our approach makes it possible to carry out a detailed device optimization in which all the layer elements in the MUTC device are varied in order to minimize the phase noise while maintaining low nonlinearity, as described in the next section.

4.5.1 Suggestions for improving device performance

Here, we use our approach to design an MUTC structure, based on the structure of Fig. 2.4, but with lower phase noise and nonlinearity. In our parameter study, we first altered the thickness of each of the absorption regions by up to 10%. However, we did not find a significant change in the impulse response. Next, we altered the doping density in each of the absorption regions. The total impulse response $h(t)$ is given by the sum of the impulse responses of each of the absorption regions separately, so that

$$h_e(t) = \sum_{j=1}^{N} h_j(t),\tag{4.3}$$

where $h_j(t)$ denotes the individual contribution of each region. For the structure in Fig. 2.4, we have $N = 7$, and we show $h_j(t)$ in Fig. 4.12, along with the location of each region. From Eq. 3.29 in Sec. 3.2, we conclude that it is desirable to reduce the variance of $h_e(t)$ as much as possible. We obtained our best results when we increased the doping density in region $j = 4$ (280 nm–430 nm) from 1.2×10^{18} cm^{-3} to 1.5×10^{18} cm^{-3}, we decreased the density in region $j = 5$ (430 nm–630 nm) from
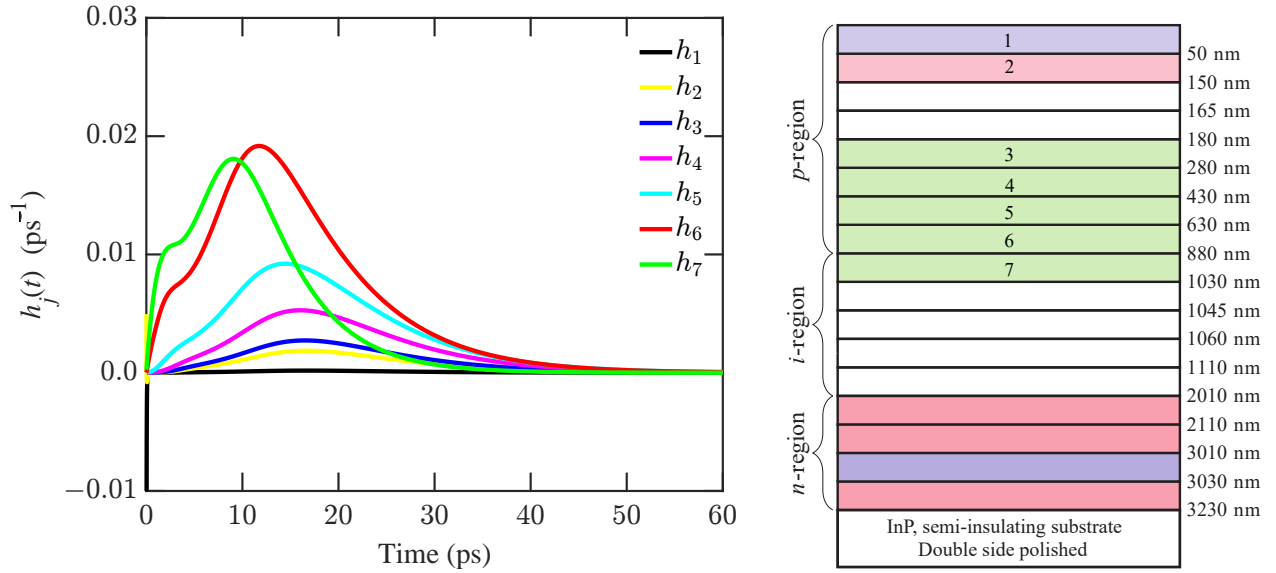
Figure 4.12: Contribution of each of the absorption regions to the impulse response of the MUTC photodetector. The diagram of the device layers is simplified from the full device structure in Fig. 2.4.

8.0×10^{17} cm^{-3} to 6.0×10^{17} cm^{-3}, and we decreased the doping density in region $j = 6$ (630 nm–880 nm) from 5.0×10^{17} cm^{-3} to 1.5×10^{17} cm^{-3}. These changes have the effect of reducing the size of the tail of $h_e(t)$.

In Table 4.1, we compare the phase noise that we calculated for the structure of Li *et al.* [42] (structure 1) and our modified structure (structure 2) for three different pulse durations at which the phase noise is experimentally measured. In all cases, the phase noise is reduced by at least 1.4 dB. For 22-ps pulses, the reduction in phase noise is over 3 dB.

We also calculated the harmonic powers in the modified structure and compared them to the harmonic powers in the Li *et al.* [42] structure in CW operation, as shown in Fig. 4.13. We find that there is no tradeoff with nonlinearity. The
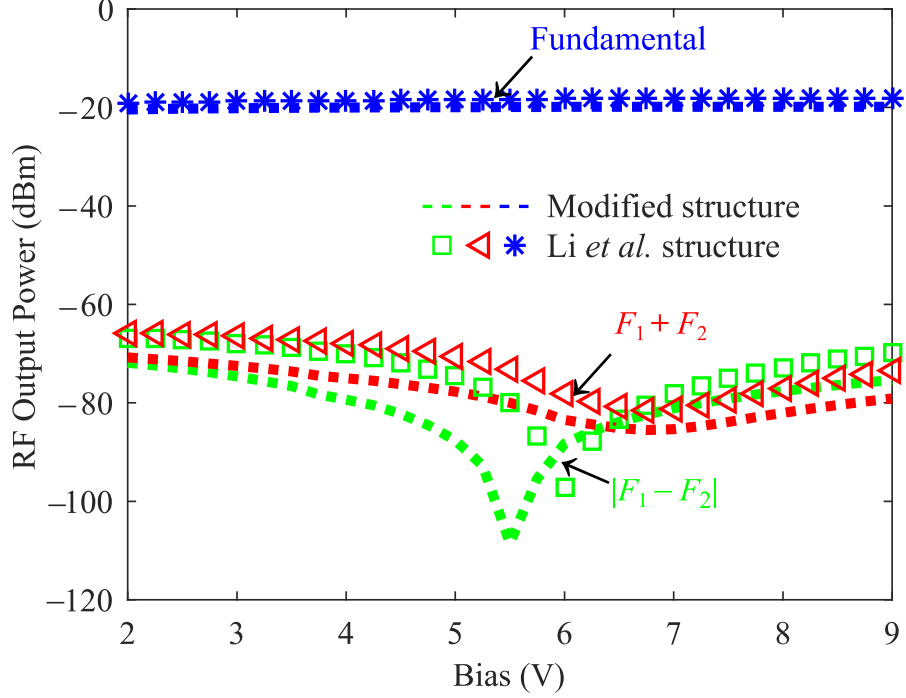
Figure 4.13: Fundamental and IMD2 ($F_1 + F_2$ and $F_1 - F_2$) powers as a function of reverse bias for the Li *et al.* [42] structure and the modified structure. We used frequencies $F_1 = 4.9$ GHz, $F_2 = 5.0$ GHz, and $F_3 = 5.15$ GHz.

Table 4.1: PN_1 = phase noise of the Li *et al.* [42] structure; PN_2 = phase noise of the modified structure; Difference = $(PN_1) - (PN_2)$.

Pulse Duration	Original structure	Modified structure	Difference
1 ps	-178.6 dBc/Hz	-180.0 dBc/Hz	1.4 dBc/Hz
12 ps	-174.0 dBc/Hz	-175.5 dBc/Hz	1.5 dBc/Hz
22 ps	-169.7 dBc/Hz	-172.8 dBc/Hz	3.1 dBc/Hz

modified structure has a lower second-order intermodulation distortion (IMD2).

It is not obvious that both phase noise and nonlinearity will improve simultaneously. To minimize phase noise, it is desirable to have as square an impulse response as possible. To minimize nonlinearity, it is desirable to minimize the vari-

ation of the efficiency and mean-square impulse response as a function of the input

pulse energy. These criteria are not equivalent.

Chapter 5

Impact of bleaching on responsivity and its effect on nonlinearity in frequency combs for *p-i-n* and MUTC photodetectors

5.1 Importance of optical links and frequency combs

Optical links are an appealing choice for a variety of radio frequency (RF) applications [29]. Applications include antenna remoting [82], radio-over-fiber [83], beamforming in phased-array radars [84], and optical signal processing of microwave signals [85]. These applications push link lengths towards 100 km or more. For link lengths in this range, stimulated Brillouin scattering [86] (SBS) severely limits the optical launch power, which necessitates the inclusion of either midspan or post-link optical amplification [87]. In many cases (e.g., antenna remoting), midspan amplification is not an option; the use of an amplifier prior to the photodetector drives the link noise figure substantially above the shot-noise limit [87]. Optical links also have some limitations such as less efficiency, higher noise figure, lower spur-free dynamic range (SFDR), and lower RF power in comparison to purely electronic systems [27].

While any single CW optical signal is limited to powers below the threshold for SBS, additional signals outside the gain bandwidth may be launched into the fiber without penalty. Hence, broadband digital signals are less susceptible to the

effects of SBS than are narrowband signals. As each comb line experiences the same RF modulation, the optical comb effectively behaves as an N-element array in the absence of chromatic dispersion as long as the signals are within the detector bandwidth. The RF signals that are recovered from the heterodyne beat of each comb line with its sidebands are coherently summed by the photodetector. Therefore, the comb-based link has the same RF performance as a conventional analog link operating at the same average photocurrent (optical power) level. The important concept here is that the power in each comb line is now limited by the SBS threshold power. Hence, an optical comb with N comb lines can transmit on the order of N times more average power through the link than is possible in a CW laser-based analog link. This approach reduces the dependence on amplification prior to the photodetector in single-span links and may eventually obviate the need for them [87]. This approach has been demonstrated experimentally by McKinney *et al.* [87]

5.1.1 Modeling responsivity in *p-i-n* and MUTC photodetectors

In Eq. 1.5 of Sec. 1.1.1, we defined the responsivity $\mathfrak{R}$ as the ratio of the output electrical current to the input optical power. It can also be expressed as the product of the quantum efficiency, η, and the ratio of the electron charge to the photon energy. In the absence of avalanche effects, the limiting value of $\mathfrak{R}$ occurs in principle when $\eta = 1$, i.e. when every incident photon is converted into an electron carrier that is conveyed to the external circuit.

5.1.1.1 Modeling bleaching in p-i-n and MUTC photodetectors

Bleaching or absorption saturation in a high-current photodetector can occur when intense optical fields deplete the number of available final energy states or depopulate the initial states [28]. Additionally, the high density of electrons that is created can increase the possibility that they are recaptured. Regardless of its origin, bleaching leads to a reduction in the photodetector's responsivity as the peak intensity and hence the average power increases. This reduction in responsivity can lead to nonlinear distortion of an incoming RF-photonic signal. Juodawlkis *et al.* [44] have reported that this effect can limit the performance of photonic analog-to-digital converters (PADCs).

Bleaching is an important issue in RF-photonic systems that use frequency combs. Examples include systems that use frequency combs to generate low-noise microwave signals [88] and systems that use frequency combs to disambiguate radar signals [37]. Frequency combs in the RF-domain are generated by using a train of short, high-peak-power optical pulses that are converted into a comb in the RF-domain by a photodetector. The pulses in a typical optical pulse train have durations less than 500 fs, and are separated by 10–50 ns, corresponding to a repetition rate of 20 MHz to 100 MHz. Hence, the peak power is larger than the average power by a factor of 10^4–10^5.

We have developed an empirical model of bleaching, and we incorporate this model into the 1-D drift-diffusion equations to calculate the responsivity. We have determined the parameters of the bleaching model by comparison with experimental
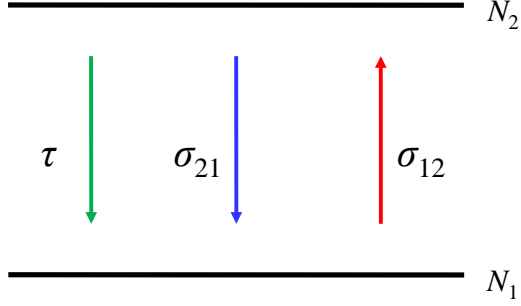
Figure 5.1: A 2-level system.

results for a *p-i-n* photodetector [13] and an MUTC photodetector [42]. When calculating the parameters of the empirical model, we used a pulse duration of 100 fs for the photodetector input.

We developed our model of bleaching starting from the well-known equations for emission and absorption for a two-level system [89], which is shown schematically in Fig. 5.1. The equations may be written

$$-\sigma_{12} N_1 I_{\mathrm{p}} + \sigma_{21} I_{\mathrm{p}} (N - N_1) + (\alpha/\tau)(N - N_1) = 0,$$

$$(\sigma_{21} I_{\mathrm{p}} + \alpha/\tau) N = [(\sigma_{12} + \sigma_{21}) I_{\mathrm{p}} + \alpha/\tau] N_1, \tag{5.1}$$

$$N_1 = N \frac{\sigma_{21} I_{\mathrm{p}} + \alpha/\tau}{(\sigma_{12} + \sigma_{21}) I_{\mathrm{p}} + \alpha/\tau},$$

where σ_{12} is the stimulated-absorption cross section, σ_{21} is the stimulated-emission cross section, I_{p} is the optical intensity, τ is the lifetime of atoms in the excited state, N_1 equals the population of the lower level, N_2 equals the population of the

upper level, and $N = N_1 + N_2$ equals the total population. We then find that

$$\frac{N_1}{N} = \frac{A + BI_\mathrm{p}}{C + DI_\mathrm{p}}, \tag{5.2}$$

where A, B, C, and D are fitting coefficients.

In practice, the physics of bleaching is complex and poorly understood. In order to match the experimentally measured bleaching, it is necessary to modify our model so that $A \neq C$. Additionally, we found that in order to obtain all positive coefficients from a least-square fit to the data, we had to add a quadratic term to our model, which then becomes

$$\frac{N_1}{N} = \frac{A + BI_\mathrm{p}}{C + DI_\mathrm{p} + EI_\mathrm{p}^2}, \tag{5.3}$$

or in both the numerator and denominator

$$\frac{N_1}{N} = \frac{A + BI_\mathrm{p} + CI_\mathrm{p}^2}{D + EI_\mathrm{p} + FI_\mathrm{p}^2}, \tag{5.4}$$

in order to obtain agreement with experiments. In effect, we are making a Pade' approximant expansion [90].

We use a least-squares algorithm to calculate the coefficients in these empirical models using unpublished data that was experimentally measured at the Naval Research Laboratory (NRL) and provided by J. D. McKinney, and is shown in Fig. 5.2.

Figure 5.2 shows experimental results of the responsivity of the *p-i-n* and MUTC photodetectors as a function of the average input optical power with a pulsed

responsivity (A/W)

* at 50 MHz repetition-rate, 100 mW: 2 nJ
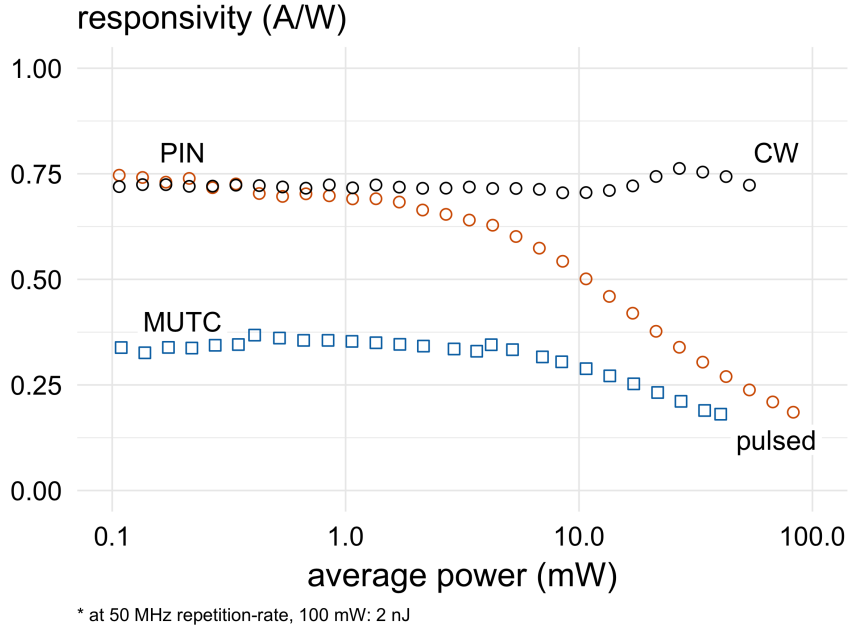
Figure 5.2: Responsivity as a function of average power for MUTC and
p-i-n photodetectors for continuous wave (CW) and pulsed inputs [91].

input in which pulses have a FWHM duration of 100 fs and a repetition frequency of
50 MHz. Figure 5.2 also shows results with a CW input for the *p-i-n* photodetector.
In the experiments, a Calmar Mendecino passively-modelocked erbium-doped fiber
laser was used. The output of the modelocked laser was a train of pulses with a
100-fs FWHM pulse duration and a 50-MHz repetition rate. The output was passed
through a variable attenuator and a calibrated optical tap with a 90/10 splitter.
The 10% tap was used as a power monitor and the 90% tap illuminated the MUTC
photodetector. The average optical power and average photocurrent were measured
as the optical attenuator was adjusted [91]. Knowing the repetition rate, the optical
power was then converted to a pulse energy to calculate the responsivity.

To take bleaching into account in our simulations, we modify the optical gen-

eration rate in Eq. 2.1. In Eq. 5.3, we assume that N_1 is the fraction of molecules that are available to create electron-hole pairs, and we multiply the generation rate in our drift-diffusion model by the factor N_1/N. The optical generation rate that we use in our drift-diffusion model G_{opt} is given by

$$G_{\mathrm{opt}}(x,t) = \frac{N_1}{N} G_c(x,t) \, \exp\left[-\alpha(L-x)\right], \tag{5.5}$$

where G_c is the generation coefficient without bleaching, α is the absorption coefficient, x is the distance across the device, and L is the device length. This model effectively assumes that the bleaching is instantaneous. That will not be the case in practice, but the finite response time will not affect the model as long as the time for the photodetector to return to the unbleached state is short compared to the repetition time. This assumption is reasonable, but has not been experimentally verified.

Figure 5.3 shows a comparison of our results to the experimental results for the MUTC photodetector using the values of A, B, C, and D in Table 5.1. The agreement using this choice is excellent. We note however that $B < 0$ is inconsistent with a two-level model. If we include a quadratic term in the denominator of Eq. 5.2, as given by Eq. 5.3 or Eq. 5.4 with $F = 0$, then all coefficients $A - E$ are positive. Table 5.2 shows the values of $A - F$ that match the data for the *p-i-n* photodetector. The agreement using this choice is also excellent as we show in Fig. 5.4. In addition to the values of $A - F$ for the MUTC photodetector, Table 5.2 contains the values of $A - F$ for the *p-i-n* photodetector in both pulsed and CW mode.
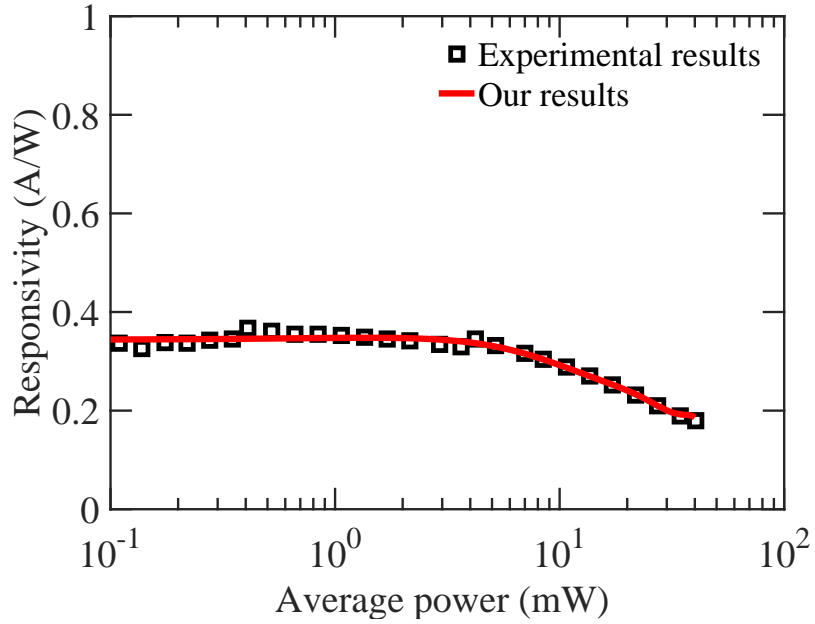
Figure 5.3: Responsivity as a function of average power for MUTC photodetectors with a pulsed input.

Table 5.1: Empirical fitting parameters in Eq. 5.2 for the MUTC photodetector with a pulsed input.

Fitting parameters	Values
A	1.000
B	-0.0073
C	2.8340
D	0.0317

Figure 5.4 shows the responsivity as a function of average optical power and compares our fitted results to the experimental results. We modified the length of the intrinsic region from 0.95 μm in the original structure [13] to 0.75 μm in this study to match the responsivity of the structure in our simulations with experimental data that was collected at the Naval Research Laboratory. We obtained good agreement

65

Table 5.2: Empirical fitting parameters in Eq. 5.3 for the MUTC photodetector and the *p-i-n* photodetector with a pulsed input and in Eq. 5.4 for the *p-i-n* photodetector with a CW input.

Fitting parameters	MUTC pulsed mode	*p-i-n* pulsed mode	*p-i-n* CW
A	1.0000	1.0000	1.0000
B	0.0322	0.0098	−0.0866
C	2.7181	0.6526	0.002
D	0.1632	0.0236	1.3924
E	0.0016	0.0015	−0.1207
F	0.000	0.00	0.0028
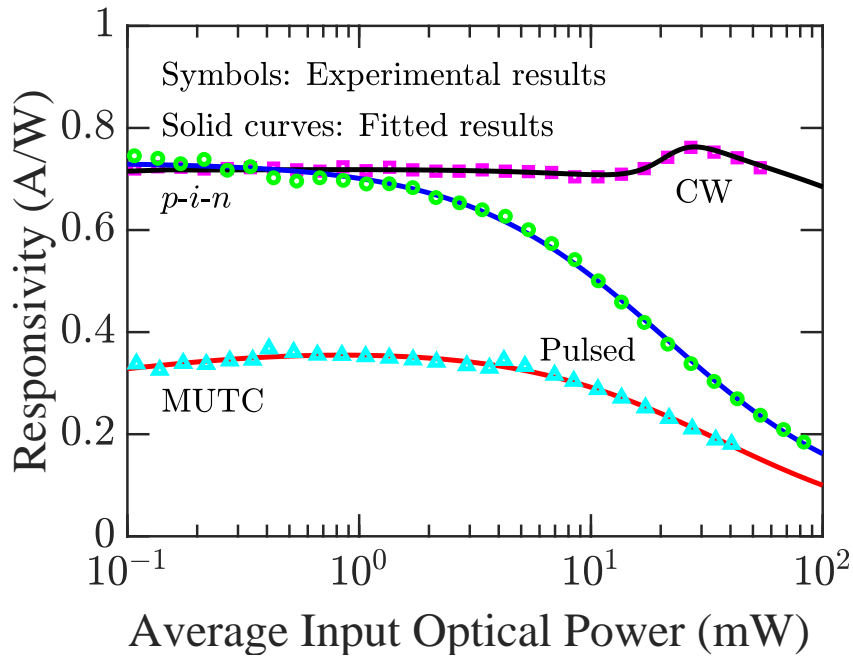
Figure 5.4: Responsivity as a function of average power for an MUTC photodetector with a pulsed input and for the *p-i-n* photodetector with both pulsed and CW inputs.

with experimental results for the MUTC photodetector in the pulsed mode. We see that it is also possible to empirically fit the CW data for the *p-i-n* photodetector,

including the visible bump. However, it is necessary to use a quadratic expression in both the numerator and denominator as a function of I_p. We are not certain that this bump is meaningful, and in any case it is not important when determining the impact of bleaching on photodetectors when operated in pulsed mode. To calculate the reduction in responsivity, we will use the measured CW values at an average power below 10 mW.

5.1.1.2 Nonlinearity characterization

The circuit nonlinearity can be characterized by representing the output voltage (V_{out}) as a function of the input voltage (V_{in}) in a Taylor series

$$V_{\text{out}}(V_{\text{in}}) = a_0 + a_1(V_{\text{in}} - V_{\text{b}}) + a_2(V_{\text{in}} - V_{\text{b}})^2 + a_3(V_{\text{in}} - V_{\text{b}})^3 + \cdots, \qquad (5.6)$$

where V_{b} is the bias voltage and

$$a_m = \frac{1}{m!} \left. \frac{d^m V_{\text{out}}}{dV_{\text{in}}^m} \right|_{V_{\text{in}}=V_{\text{b}}}, \qquad (5.7)$$

with $a_0 = V_{\text{out}}(V_{\text{b}})$ [28].

Consider an input signal of the form

$$V_{\text{in}}(t) = V_{\text{b}} + V \sin(\omega_1 t) + V \sin(\omega_2 t) + V \sin(\omega_3 t), \qquad (5.8)$$

where $\omega_j = 2\pi f_j$, $j = 1, 2, 3$. Substituting this input into Eq. 5.6, we obtain

67

$$V_{\text{out}}(t) = a_0 + a_1 V \left[\sin(2\pi f_1 t) + \sin(2\pi f_2 t) + \sin(2\pi f_3 t) \right]$$

$$+ a_2 V^2 \left[\sin(2\pi f_1 t) + \sin(2\pi f_2 t) + \sin(2\pi f_3 t) \right]^2 \qquad (5.9)$$

$$+ a_3 V^3 \left[\sin(2\pi f_1 t) + \sin(2\pi f_2 t) + \sin(3t) \right]^3 + \cdots ,$$

and after some algebra

$$V_{\text{out}}(t) = \left(a_0 + \frac{3 a_2 V^2}{2} \right) + \left(a_1 V + \frac{15 a_3 V^3}{4} \right) \sin(2\pi f_1 t)$$

$$+ \left(a_1 V + \frac{15 a_3 V^3}{4} \right) \sin(2\pi f_2 t) + \left(a_1 V + \frac{15 a_3 V^3}{4} \right) \sin(2\pi f_3 t)$$

$$- \frac{a_2 V^2}{2} \cos(4\pi f_1 t) - \frac{a_2 V^2}{2} \cos(4\pi f_2 t) - \frac{a_2 V^2}{2} \cos(4\pi f_3 t)$$

$$+ a_2 V^2 \cos\left[2\pi(f_1 - f_2)t \right] - a_2 V^2 \cos\left[2\pi(f_1 + f_2)t \right]$$

$$+ a_2 V^2 \cos\left[2\pi(f_1 - f_3)t \right] - a_2 V^2 \cos\left[2\pi(f_1 + f_3)t \right]$$

$$+ a_2 V^2 \cos\left[2\pi(f_2 - f_3)t \right] - a_2 V^2 \cos\left[2\pi(f_2 + f_3)t \right]$$

$$- \frac{a_3 V^3}{4} \sin(6\pi f_1 t) - \frac{a_3 V^3}{4} \sin(6\pi f_2 t) - \frac{a_3 V^3}{4} \sin(6\pi f_3 t)$$

$$+ \frac{3 a_3 V^3}{4} \sin\left[2\pi(2f_1 - f_2)t \right] - \frac{3 a_3 V^3}{4} \sin\left[2\pi(2f_1 + f_2)t \right]$$

$$+ \frac{3 a_3 V^3}{4} \sin\left[2\pi(2f_1 - f_3)t \right] - \frac{3 a_3 V^3}{4} \sin\left[2\pi(2f_1 + f_3)t \right]$$

$$+ \frac{3 a_3 V^3}{4} \sin\left[2\pi(2f_2 - f_1)t \right] - \frac{3 a_3 V^3}{4} \sin\left[2\pi(2f_2 + f_1)t \right]$$

$$+ \frac{3 a_3 V^3}{4} \sin\left[2\pi(2f_2 - f_3)t \right] - \frac{3 a_3 V^3}{4} \sin\left[2\pi(2f_2 + f_3)t \right]$$

$$+ \frac{3 a_3 V^3}{4} \sin\left[2\pi(2f_3 - f_1)t \right] - \frac{3 a_3 V^3}{4} \sin\left[2\pi(2f_3 + f_1)t \right]$$

$$+ \frac{3 a_3 V^3}{4} \sin\left[2\pi(2f_3 - f_2)t \right] - \frac{3 a_3 V^3}{4} \sin\left[2\pi(2f_3 + f_2)t \right]$$

$$+ \frac{3 a_3 V^3}{2} \sin\left[2\pi(f_1 + f_2 - f_3)t \right] + \frac{3 a_3 V^3}{2} \sin\left[2\pi(f_1 - f_2 + f_3)t \right]$$

$$- \frac{3 a_3 V^3}{2} \sin\left[2\pi(f_1 + f_2 + f_3)t \right] - \frac{3 a_3 V^3}{2} \sin\left[2\pi(f_1 - f_2 - f_3)t \right] + \cdots .$$

$$(5.10)$$

Additional frequency components appear in Eq. 5.10 that are due to intermodulation distortion (IMD) at the frequencies $f_1 \pm f_2$, $f_1 \pm f_3$, $f_2 \pm f_3$, $2f_1 \pm f_2$, $2f_1 \pm f_3$, $2f_2 \pm f_3$, $2f_3 \pm f_1$, $2f_3 \pm f_2$, and $f_1 \pm f_2 \pm f_3$.

We calculate the impact of photodetector nonlinearity on an RF-photonic signal as a function of the average optical power, including the effect of bleaching. When considering nonlinearity in photodetectors, the second-order intermodulation distortion (IMD2) and the third-order intermodulation distortion (IMD3) are particularly significant, especially IMD3, since it generates frequencies that can interfere with the fundamental frequency. The second-order output intercept point (OIP2) and the third-order output intercept point (OIP3) are the usual figures of merit to characterize IMD2 and IMD3 powers [1]. The OIP2 and OIP3 are defined as the extrapolated intercept point of the power of the fundamental frequency and the IMD2 and IMD3 powers, respectively. On a log-log plot, the slope of the fundamental power is 1 and the slope of the IMD2 power is 2, as shown schematically in Fig. 5.5. OIP2 can be calculated from the fundamental power and the IMD2 power,

$$\text{OIP2} = 2P_f - P_{\text{IMD2}}, \tag{5.11}$$

where P_f is the fundamental power in dBm, and P_{IMD2} is the power of the IMD2 in dBm [1, 92]. The slope of the IMD3 power on a log-log plot is 3, and we show it schematically in Fig. 5.6. OIP3 can be calculated from the fundamental power and the IMD3 power,

$$\text{OIP3} = P_f + \frac{1}{2} \left(P_f - P_{\text{IMD3}} \right), \tag{5.12}$$
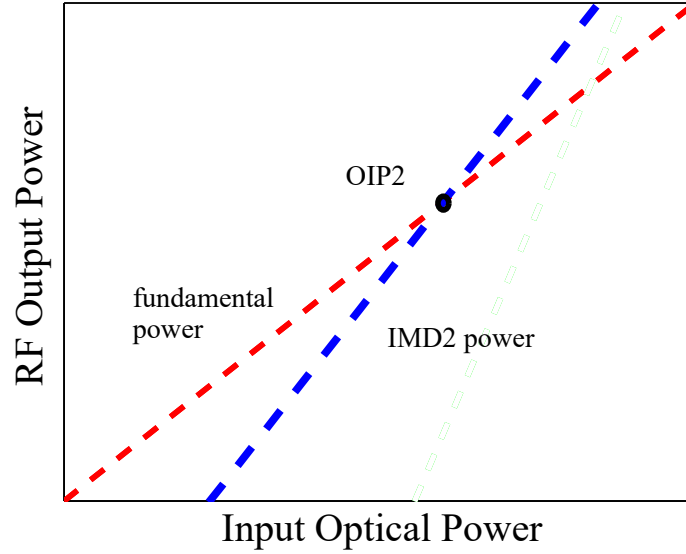
Figure 5.5: RF output power as a function of optical input power.
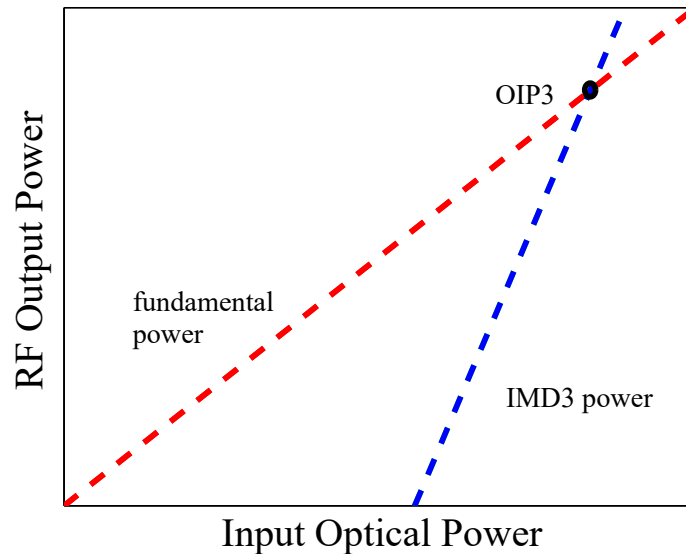
Figure 5.6: RF output power as a function of optical input power.

where P_{IMD3} is the IMD3 power in dBm [1, 55, 92]. As we mentioned earlier, there are several second-order intermodulation terms at the frequencies $f_1 \pm f_2$, $f_1 \pm f_3$, and $f_2 \pm f_3$, and third-order intermodulation terms at the frequencies $f_1 \pm f_2 \pm f_3$. Some of these third-order intermodulation frequencies are close to the fundamental frequency.
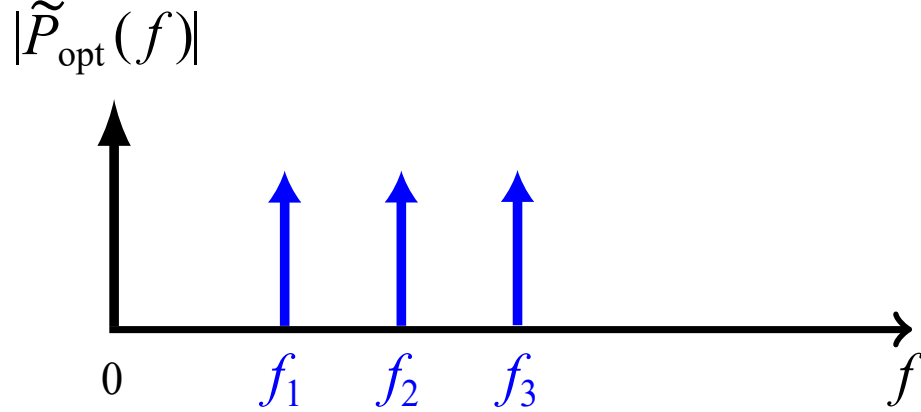
Figure 5.7: Spectrum of the optical intensity profile of a CW three-tone modulated input.

Figure 5.7 shows the spectrum of the optical intensity profile of a CW three-tone modulated input signal where $\widetilde{P}_{\text{opt}}(f)$ is the Fourier transform of $P_{\text{opt}}(t)$. There are three frequency components that correspond to three modulation frequencies f_1, f_2, and f_3, shown as blue arrows. Figure 5.8 shows the spectrum of the output current of the photodetector due to a CW three-tone modulated input. There are three-tone modulation frequency components at f_1, f_2, and f_3 that are shown as blue arrows, IMD2 components at $f_1 + f_2$ and $|f_1 - f_2|$ that are shown as magenta arrows, and an IMD3 component at $f_1 + f_2 - f_3$ that is shown as a cyan arrow. If f_1, f_2, and f_3 are all nearly equal, then there are IMD3 products that are close to f_1 and can interfere with it.

Photodetector nonlinearity can be measured using one-, two-, and three-tone measurement systems [1]. Figure 5.9 shows the set up of a three-tone measurement system. Three Nd:YAG lasers are modulated by three Mach-Zehnder modulators (MZMs), and their output is fed through optical attenuators. The first two modu-
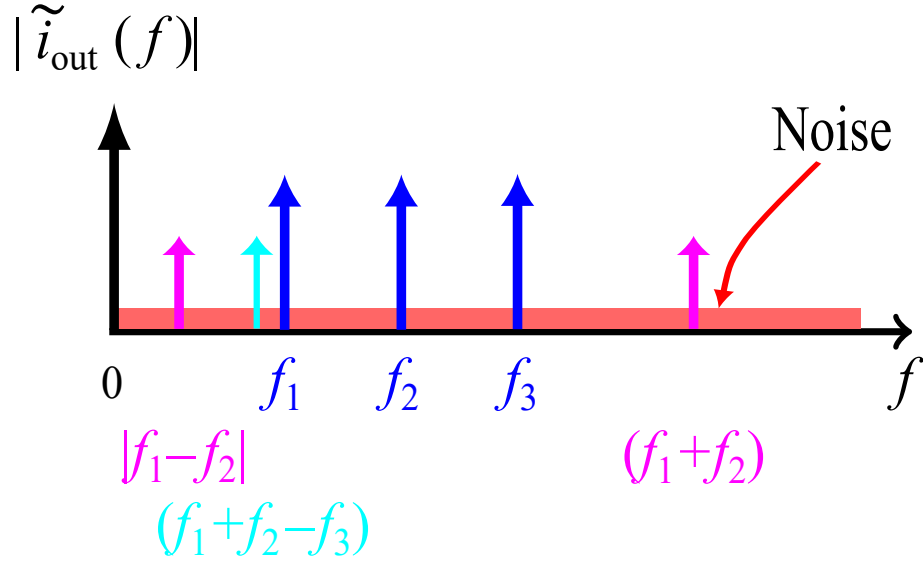
Figure 5.8: Spectrum of the output current due to a CW three-tone modulated input.
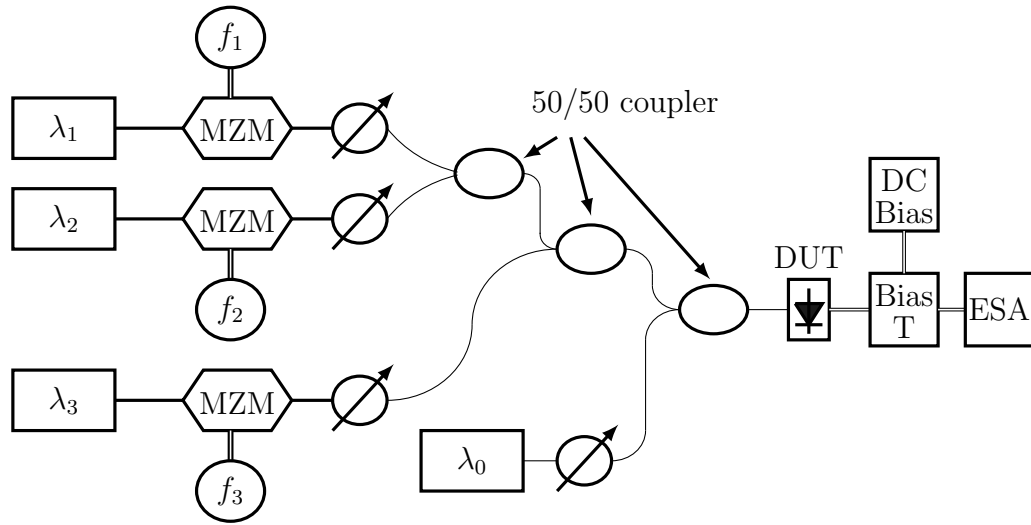
Figure 5.9: A four-laser three-tone MZM measurement setup. This figure is similar to Fig. 2 in [1].

lated light frequencies are combined using a 50/50 coupler and are then combined with a third frequency using another 50/50 coupler. The unmodulated laser frequency is transmitted through a variable optical attenuator and is then combined with the signal using a final 50/50 coupler. The output is fed into the device under

test (DUT). The RF output power is measured with an electrical spectrum analyzer (ESA). The modulation depth is varied by attenuating the lasers.

In our calculation, the input modulated light power $P(t)$ may be expressed as

$$P(t) = P_{\text{opt}}(t) \left\{ 1 + m \left[\sin \left(2\pi f_1 t \right) + \sin \left(2\pi f_2 t \right) + \sin \left(2\pi f_3 t \right) \right] \right\}, \qquad (5.13)$$

where m is modulation depth, f_1, f_2, and f_3 are the three modulation frequencies, and $P_{\text{opt}}(t)$ is the input light power of the optical envelope as a function of time, which is constant as a function of time in the CW mode and is defined as

$$P_0(t) = \sum_n A \operatorname{sech} \left(\frac{t - nT_r}{\tau} \right), \qquad (5.14)$$

in the pulsed mode, where A is the amplitude of input optical power, T_r is the repetition time, and τ is the pulse width.

If we write the electric field as

$$\mathbf{E}(t) = \mathbf{E}_i(t) \exp(2\pi j f_0 t) + \mathbf{E}_i^*(t) \exp(-2\pi j f_0 t), \qquad (5.15)$$

where f_0 is the frequency of the optical carrier, then we find that

$$P_{\text{opt}}(t) = 2 A_{\text{eff}} \epsilon c |\mathbf{E}_i(t)|^2, \qquad (5.16)$$

where A_{eff} is the effective area of the optical beam. The three frequencies are close to each other in the experiments. In our calculations, we used $f_1 = 10$ MHz, $f_2 = 10.5$
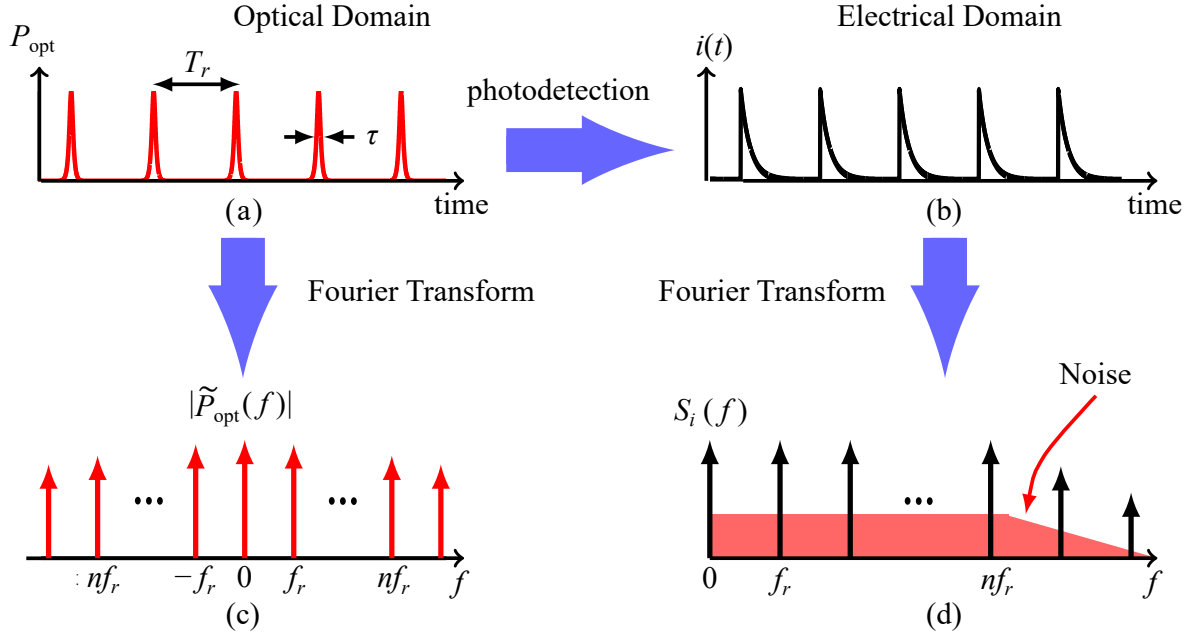
Figure 5.10: Time and frequency domain depictions of the optical and photodetected electrical pulse trains, where T_r is the repetition time and τ is the pulse duration of the optical signal. (a) Optical pulse train intensity profile. (b) Photodetected electrical pulse train. (c) Spectrum of the optical intensity profile. (d) Power spectrum of the photocurrent. This figure is similar to Fig. 1 in Quinlan *et al.* [45]

MHz, and $f_3 = 9$ MHz. The reason for choosing these three frequencies is to be close to each other, fall inside the 50-MHz repetition frequency, and also avoid aliasing. We will consider a pulse train that is 2-μs long and thus an integer number of periods for f_1, f_2, and f_3.

The use of frequency combs changes the characterization of nonlinearity in a fundamental way. The IMD2 and IMD3 and hence the OIP2 and OIP3 all become functions of the comb line number n. Instead of one of each of these quantities, as is the case for a modulated CW input, we must determine these quantities for each comb line. Figure 5.10 illustrates schematically the photodetection of a periodic
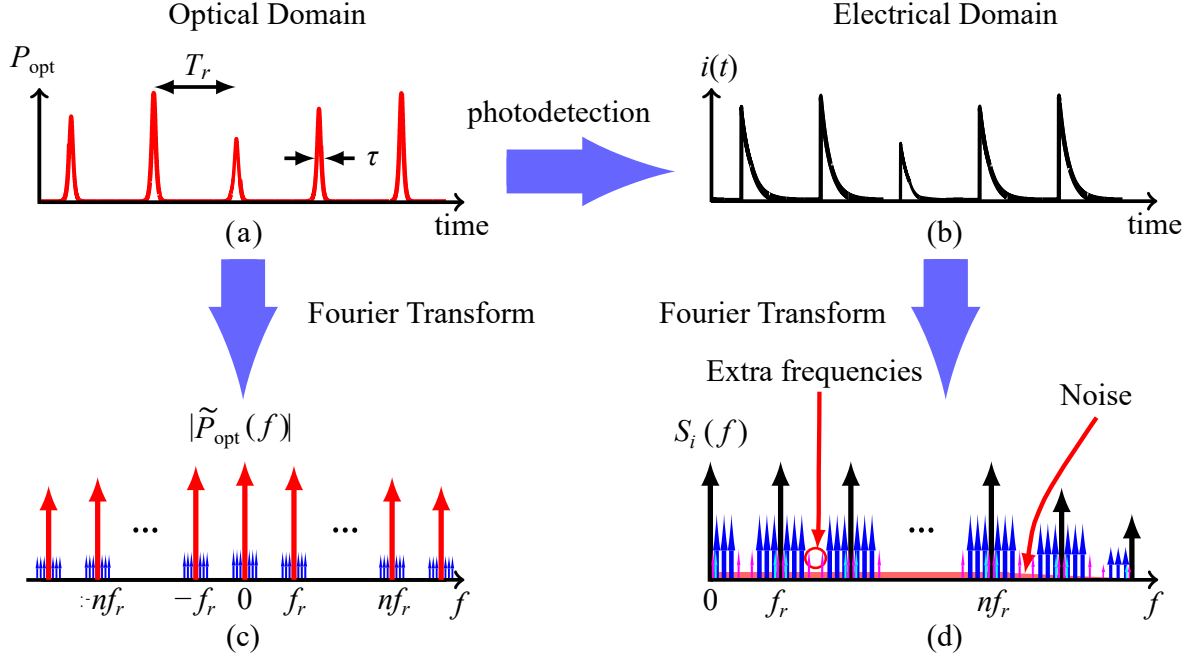
Figure 5.11: Time and frequency domain depictions of a modulated optical and photodetected electrical pulse trains, where T_r is the repetition time and τ is the pulse duration of the optical signal. (a) Modulated optical pulse train intensity profile. (b) Modulated photodetected electrical pulse train. (c) Spectrum of the modulated optical intensity profile. (d) Power spectrum of the modulated photocurrent.

train of optical pulses, which then produces a train of electrical pulses where $\widetilde{P}_{\mathrm{opt}}(f)$ is the Fourier transform of $P_{\mathrm{opt}}(t)$ and $S_i(f)$ is the photocurrent spectral density. The periodic train of optical pulses corresponds to equally spaced comb lines in the frequency domain that are spaced by the repetition frequency and centered around zero [45]. The output of the photodetector is a periodic train of electrical pulses that corresponds to comb lines in the frequency domain that are again separated by the repetition frequency. The output radio frequency spectrum sits on top of a noise pedestal. We modulate the input optical pulses with three different frequencies.

Figure 5.11 shows time and frequency domain depictions of a modulated op-
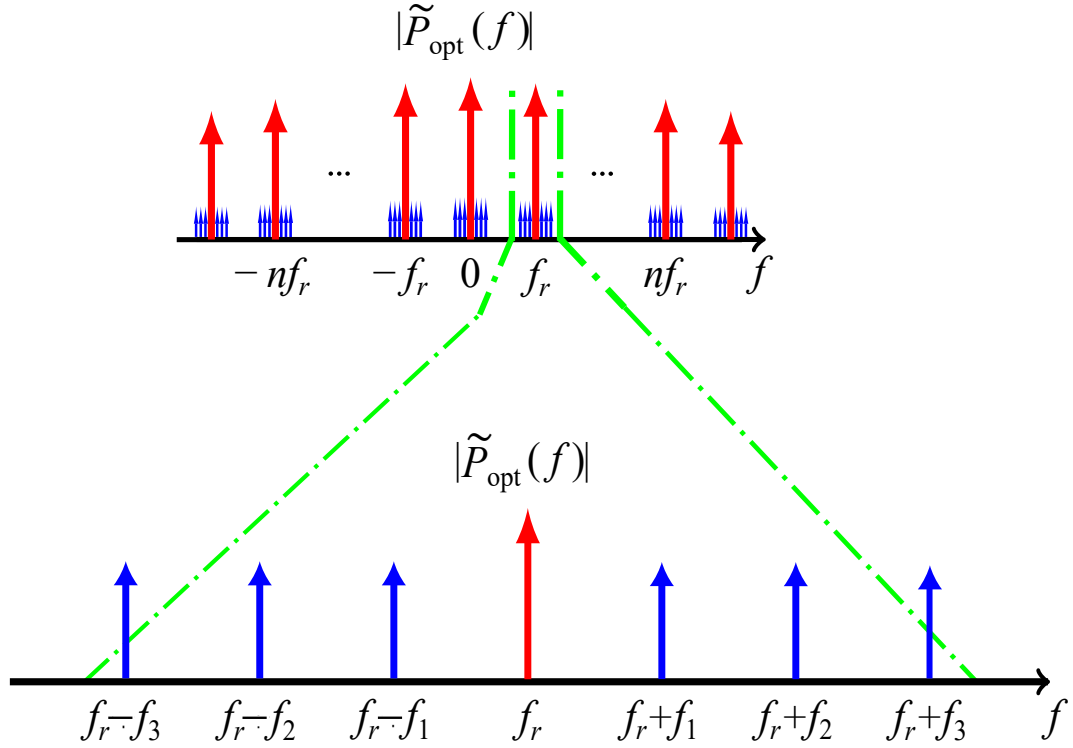
Figure 5.12: Expanded view of the spectrum of the modulated optical intensity profile. Red arrows show comb lines at harmonics of the repetition frequency. Blue arrows show the comb lines at modulation frequencies ($nf_r \pm f_1$, $nf_r \pm f_2$, and $nf_r \pm f_3$ for each comb line where n is the comb line number. In the expanded view, we show comb lines for $n = 1$.

tical and a photodetected electrical pulse train, while Fig. 5.12 shows the spectrum of the modulated optical intensity profile and the corresponding frequency domain comb lines. The n-th comb line, which is shown by a red arrow, is surrounded by smaller lines at the modulated frequencies $nf_r \pm f_1$, $nf_r \pm f_2$, and $nf_r \pm f_3$, which are shown by blue arrows. In the expanded view, we show the fundamental and modulation frequency components for the first comb line ($n = 1$). Associated with each comb line is a fundamental power $S_{in} = S_i(nf_r)$, as well as power in each of the modulated components.
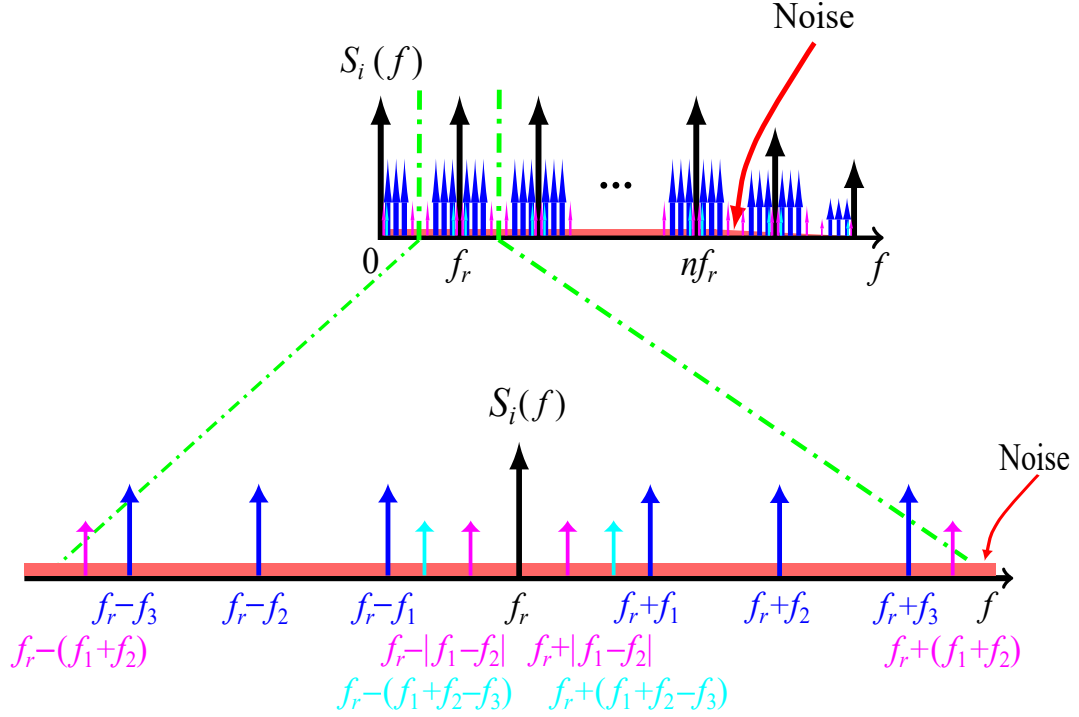
Figure 5.13: Expanded view of the power spectrum of the modulated photocurrent. Black arrows show comb lines at the harmonics of the fundamental frequency. Blue arrows show comb lines at modulated frequencies ($nf_r \pm f_1$, $nf_r \pm f_2$, and $nf_r \pm f_3$) for each comb line, where n is the comb line number. Purple arrows show IMD2$_n$ lines at $nf_r \pm (f_1 \pm f_2)$. Cyan arrows show IMD3$_n$ lines at $nf_r \pm (f_1 + f_2 - f_3)$. In the expanded view, we show comb lines for $n = 1$.

Figure 5.13 shows the power spectrum of the modulated photocurrent. There is a set of comb lines, which are indicated by black arrows. Each comb line is surrounded by lines at the modulation frequencies $nf_r \pm f_1$, $nf_r \pm f_2$, and $nf_r \pm f_3$, which are shown with blue arrows, lines at the IMD2$_n$ frequencies $nf_r \pm (f_1 \pm f_2)$, which are shown with purple arrows, and lines at the IMD3$_n$ frequencies $nf_r \pm (f_1 + f_2 - f_3)$, which are shown with cyan arrows. In this figure, we show the fundamental frequency, the modulated frequency components, and the additional IMD2$_n$, and IMD3$_n$ components for the first comb line.

We calculate the nonlinearity as a function of the average input optical power $P_{\mathrm{opt}}(t)$, given in Eq. 5.13, for different modulation depths. For pulsed inputs, we first calculate the impulse response of the photodetector for different input optical pulse energies, and we then combine the electrical pulse in the time domain, given by Eq. 5.14, taking into account the gap of 20 ns between the pulses, to obtain the total electrical response $P_{\mathrm{e}}(t)$ over a 2-μs-long modulation time. We next calculate the Fourier transform of $P_{\mathrm{e}}(t)$ in order to determine the harmonic powers of the photocurrent for a different choice of the amplitude A. Using this approach, along with Eq. 5.5, we calculate the nonlinear distortion of a pulsed input both with and without bleaching. We study modulation depths $m = 4\%$ and $m = 8\%$. The principal effect of bleaching is to lower the responsivity of the photodetector so that fewer electrons are produced. That lowers the power at the fundamental frequencies S_{in}, but also decreases contribution of space charge to the nonlinearity.

In this dissertation, we focused on the IMD2$_n$ products at $nf_r + (f_1 - f_2)$ and the IMD3$_n$ products at $nf_r + (f_1 - f_2 + f_3)$. These are the frequency combinations closest to the fundamental frequency. We calculate one IMD2$_n$ and one IMD3$_n$ and from that one OIP2$_n$ and one OIP3$_n$ for each comb line n. We calculate the IMD2$_n$, IMD3$_n$, OIP2$_n$, and OIP3$_n$ for a single comb line n as a function of comb line frequency $f = nf_r$, where f_r is the repetition frequency of the input optical power (50 MHz) as a function of comb line frequency. We also calculate distortion-to-signal ratios $\rho_{2n} = \mathrm{IMD2}_n/S_{in}$ and $\rho_{3n} = \mathrm{IMD3}_n/S_{in}$ for each comb line n, and we show the effect of bleaching on this ratio. Also, we calculate the contributions of the electron current, hole current, and displacement current to OIP2$_n$, OIP3$_n$, ρ_{3n},

and ρ_{3n} in both *p-i-n* and MUTC photodetector for modulation depths $m = 4\%$.

Chapter 6

Impact of Nonlinearity on RF-Modulated Frequency Combs

In this section, we discuss the impact of nonlinearity on RF-modulated frequency combs in both a *p-i-n* and an MUTC photodetector. As mentioned earlier in Chap. 5, Sec. 5.1.1, we modified the length of the intrinsic region from 0.95 μm in the original *p-i-n* structure [13] to 0.75 μm in this study to match the responsivity of the structure in our simulations with experimental data that was collected at the Naval Research Laboratory. The MUTC structure [42] that we study here is the same one that we used in previous chapters. We define the comb line frequency as $f = nf_r$ where n is the comb line number and f_r is the repetition frequency of the input optical power (50 MHz).

Juodawlkis *et al.* [44] found that bleaching (nonlinear saturation) degrades the performance of photonic analog-to-digital converters (PADCs) by reducing responsivity at high peak power and can potentially add to nonlinear distortion. In order to investigate the impact of bleaching, we compare the nonlinear distortion with bleaching to the nonlinear distortion when bleaching is not included. We calculate the intermodulation distortion products IMD2 and IMD3 and the corresponding output intercept points OIP2 and OIP3 as a function of the average input optical power $P_{\text{opt}}(t)$, given in Eq. 5.13. The principal effect of bleaching is to lower the responsivity, which in turn decreases the space charge. We thus find, somewhat

paradoxically, that bleaching lowers the nonlinear distortion at some frequencies. In general, the impact of bleaching on nonlinear distortion is complex. Its effect differs significantly depending on both the comb line number and the device.

We compare our results with and without bleaching for modulation depths of 4% and 8%. Changing the modulation depth allows us to validate the assumption that we can expand second- and third-order intermodulation distortion powers quadratically and cubically, respectively. We find that this assumption is valid at least up to a modulation depth of 8%.

In order to better understand how nonlinearity affects the nonlinear distortion, we individually calculated the contribution of the three current components —the electron current, the hole current, and the displacement current— to the nonlinear distortion. As expected, the hole current contributes significantly to the nonlinear distortion in p-i-n photodetectors. Without bleaching, the displacement current is significant in both devices at some frequencies. However, it becomes negligible in both devices when bleaching is taken into account.

6.1   Simulation results for the p-i-n and MUTC photodetectors

Figures 6.1 and 6.2 show OIP2$_n$ and OIP3$_n$ as a function of comb line frequency and mode number n with an average input optical power of 25 mW for the MUTC photodetector and the p-i-n photodetector, respectively. We show OIP2$_n$ and OIP3$_n$ when bleaching is included and when it is not for modulation depths $m = 4\%$ and $m = 8\%$.

Figure 6.1: $OIP2_n$ and $OIP3_n$ as a function of comb line frequency for the MUTC photodetector with modulation depths $m = 4\%$ and $m = 8\%$. The average input optical power is 25-mW. (a) $OIP2_n$, $m = 4\%$; (b) $OIP2_n$, $m = 8\%$; (c) $OIP3_n$, $m = 4\%$; (d) $OIP3_n$, $m = 8\%$.

Figures 6.1(a) and 6.1(b) show the intercept point between the $IMD2_n$ power and the fundamental power S_{in} in the n-th comb line, while Figs. 6.1(c) and 6.1(d) show the intercept point between the $IMD3_n$ power and the fundamental power S_{in}. These intercept points occur at a lower power when bleaching is included than when it is not. The gap is larger for low comb line numbers. The intercept point decreases

both with and without bleaching when n increases, but this decrease is noticeably slower when bleaching is included, so that the intercepts cross and diverge again when n is large. The falloff of $OIP2_n$ and $OIP3_n$ occurs because the amplitude of the power in the frequency domain decreases as frequency increases. $OIP2_n$ and $OIP3_n$ are lower when bleaching is included because bleaching reduces the output power due to the reduction in the responsivity. The behavior of $OIP2_n$ and $OIP3_n$ as a function of comb line frequency is defined by the pattern of the impulse response with and without bleaching in the frequency domain. The impact of bleaching is to lower the responsivity, which lowers the space charge, but at the same time it decreases the power at higher frequencies. Hence, as a result we observe that the decrease in $OIP2_n$ and $OIP3_n$ due to bleaching is large at low frequencies, becomes almost negligible at 15 GHz, and increases again at frequencies beyond 15 GHz.

In Fig. 6.2 we now show the $OIP2_n$ and $OIP3_n$ for the p-i-n photodetector. We note that the scale in Fig. 6.2 is different from Fig. 6.1 because in general the $OIP2_n$ and $OIP3_n$ are higher. Figures 6.2(a) and 6.2(b) show the intercept point between the $IMD2_n$ power and the fundamental power S_{in} in the n-th comb line, while Figs. 6.2(c) and 6.2(d) show the intercept point between the $IMD3_n$ power and the fundamental power S_{in}. The same as the MUTC photodetector, these intercept points occur at a lower power when bleaching is included than when it is not and gap is larger for low comb line numbers. The intercept point decreases both with and without bleaching when n increases, but in contrast to the MUTC photodetector, in the p-i-n photodetector, this decrease is noticeably slower when bleaching is included. The decrease in responsivity affects the output power in the
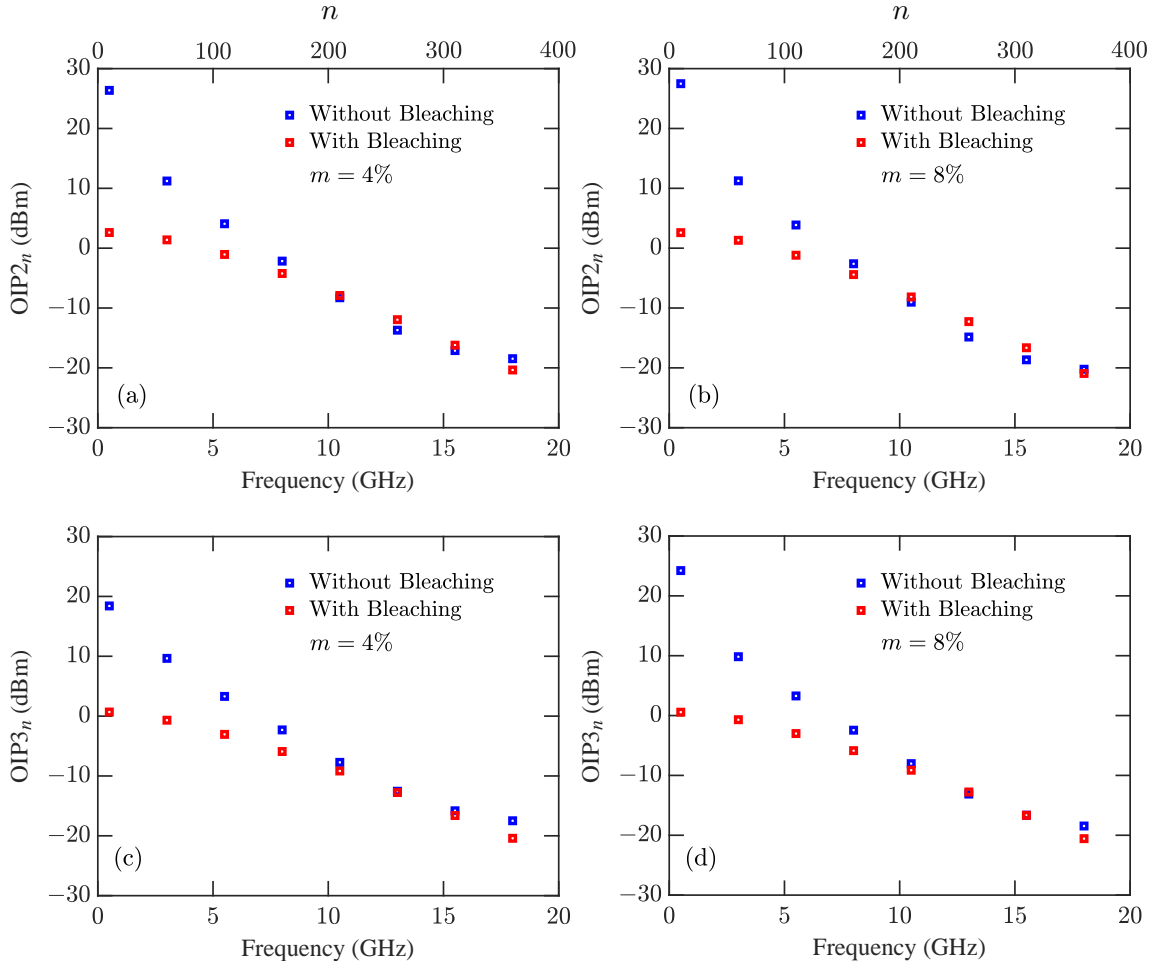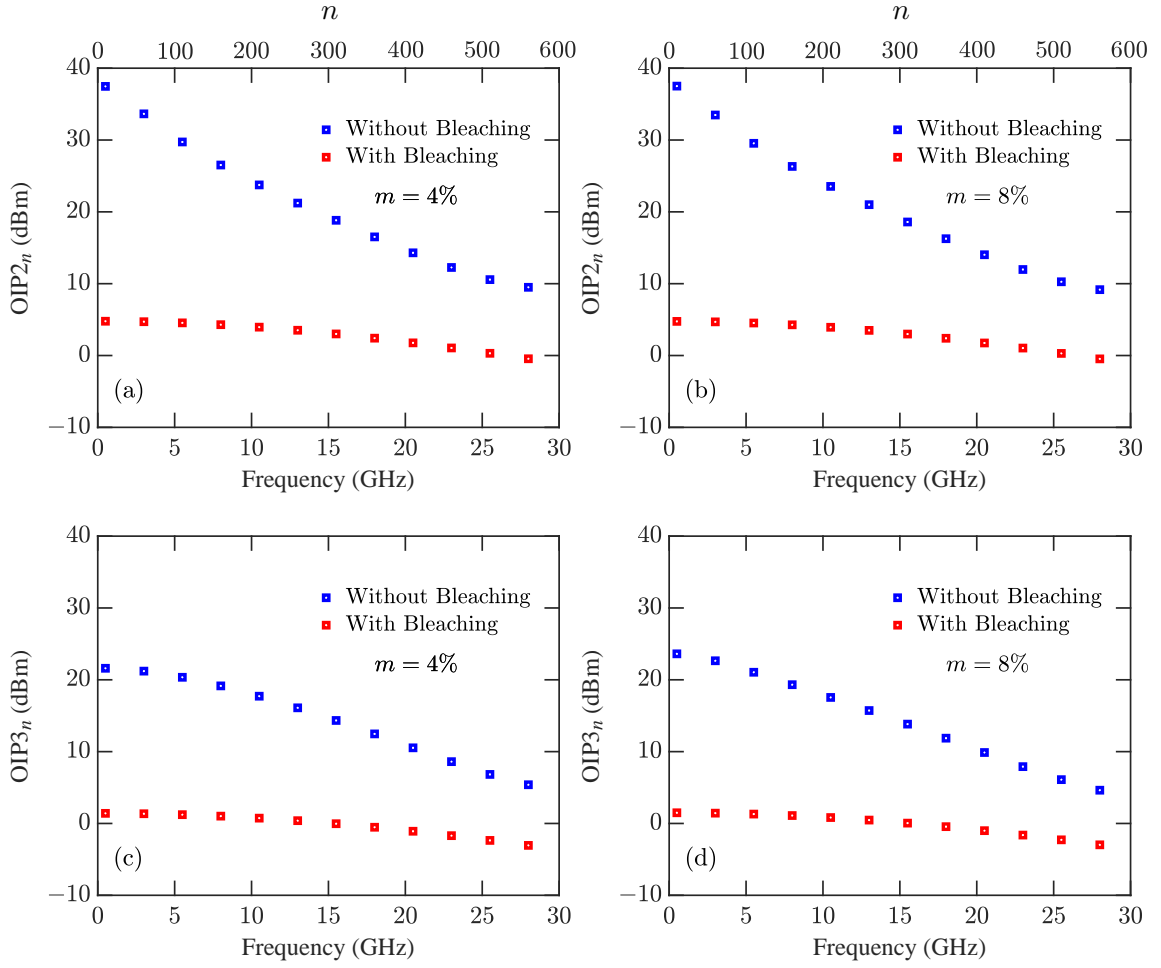
Figure 6.2: $OIP2_n$ and $OIP3_n$ as a function of comb line frequency for the *p-i-n* photodetector with modulation depths $m = 4\%$ and $m = 8\%$. The average input optical power is 25-mW. (a) $OIP2_n$, $m = 4\%$; (b) $OIP2_n$, $m = 8\%$; (c) $OIP3_n$, $m = 4\%$; (d) $OIP3_n$, $m = 8\%$.

p-i-n photodetector more than in the MUTC photodetector, so that the fundamental power and intermodulation distortion powers only change slightly as n increases when bleaching is included. Hence, the gap between $OIP2_n$ and $OIP3_n$ becomes smaller as n becomes larger.

Figures 6.3 and 6.4 compare $OIP2_n$ and $OIP3_n$ for the MUTC and *p-i-n* photodetectors with modulation depths $m = 4\%$ and $m = 8\%$ when bleaching is in-

cluded. As can be seen in Fig. 6.3, $OIP2_n$ and $OIP3_n$ are both slightly higher for modulation depth $m = 4\%$ than for modulation depth $m = 8\%$. However, this
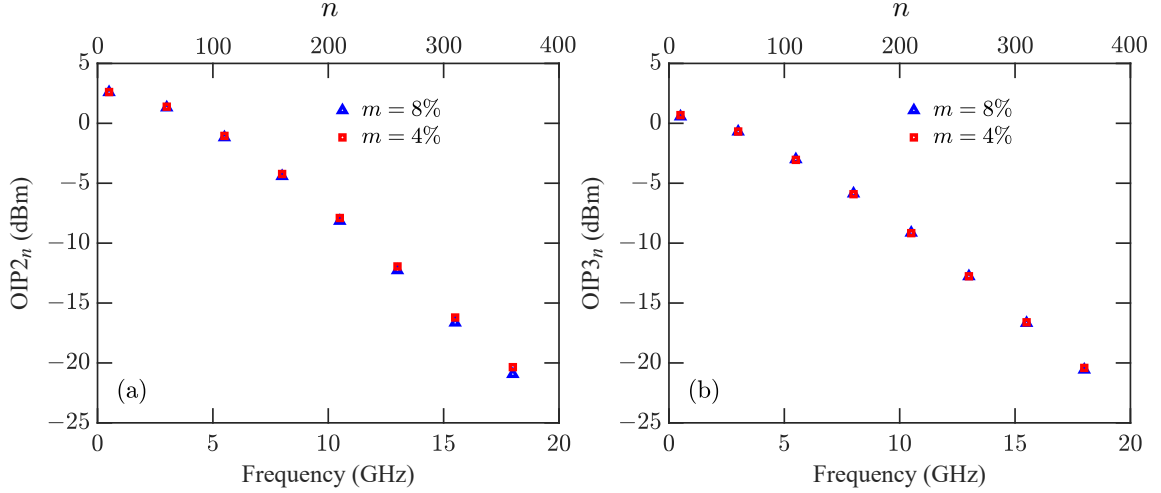
Figure 6.3: Comparison of (a) $OIP2_n$ and (b) $OIP3_n$ for the MUTC photodetector when bleaching is included with $m = 4\%$ and $m = 8\%$.
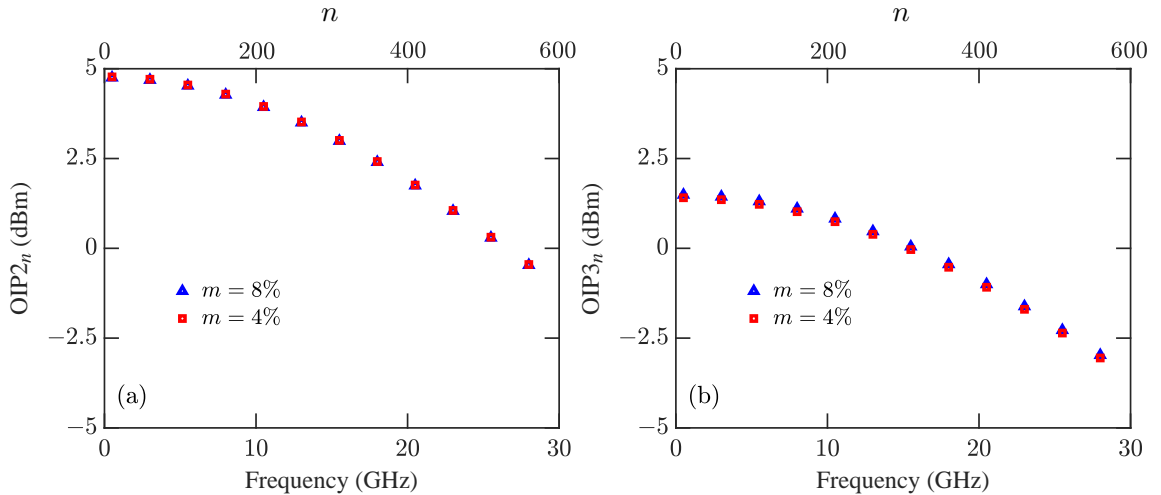
Figure 6.4: Comparison of (a) $OIP2_n$ and (b) $OIP3_n$ for the p-i-n photodetector when bleaching is included with $m = 4\%$ and $m = 8\%$.

difference is negligibly small. As can be seen in Fig. 6.4, $OIP2_n$ is almost iden-

tical for both $m = 4\%$ and $m = 8\%$, but OIP3$_n$ is slightly higher for modulation depth $m = 4\%$ than it is for modulation depth $m = 8\%$. As was the case for the
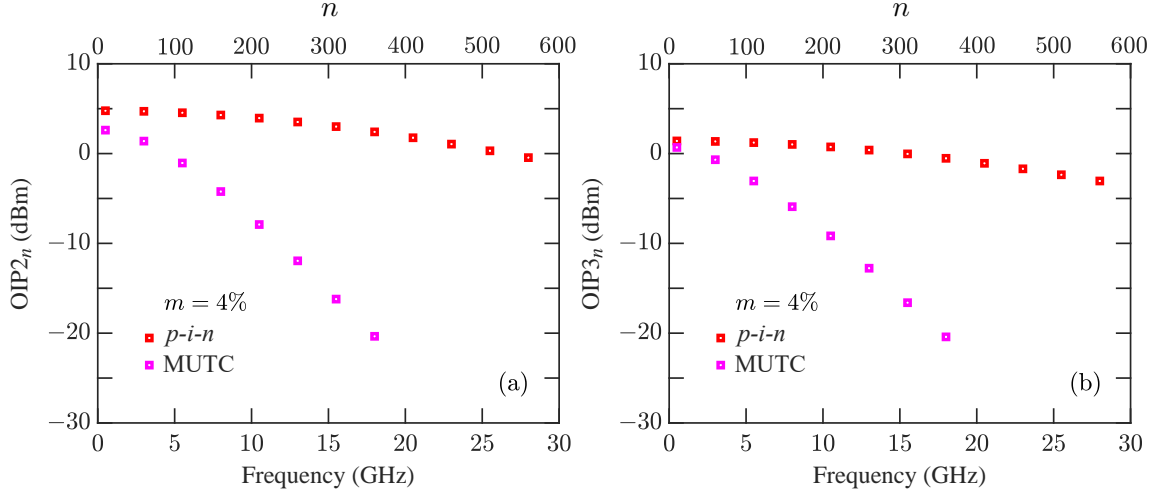
Figure 6.5: Comparison of (a) OIP2$_n$ and (b) OIP3$_n$ when bleaching is included for $m = 4\%$ in the p-i-n and MUTC photodetectors.

MUTC photodetector, this difference is negligible. Hence, our use of the standard intermodulation distortion products is valid up to at least $m = 8\%$.

Figure 6.5 compares OIP2$_n$ and OIP3$_n$ with modulation depth $m = 4\%$ in the p-i-n and MUTC photodetectors when bleaching is included. OIP2$_n$ and OIP3$_n$ for the p-i-n photodetector have fallen by ~ 5 dB at 28 GHz, while OIP2$_n$ and OIP3$_n$ for the MUTC photodetector have fallen by more than 20 dB at 18 GHz. As we will discuss shortly, this difference leads to a dramatic difference in the distortion-to-signal ratios. In order to explain this difference between the p-i-n and MUTC photodetectors, we plotted the fundamental power, IMD2$_n$ power, and IMD3$_n$ power as a function of frequency in Fig. 6.6 when bleaching is included. Some of the difference between these two photodetectors can perhaps be attributed to the difference
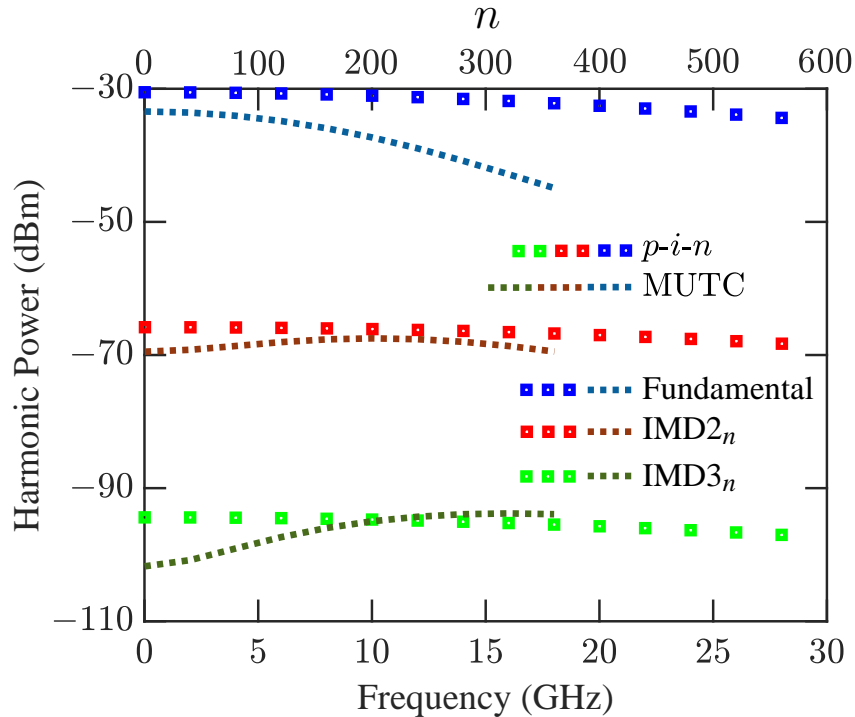
Figure 6.6: Fundamental power, $IMD2_n$ power, and $IMD3_n$ power as a function of frequency in the p-i-n and MUTC photodetectors.

between the 3-dB bandwidth of the two devices that we considered, which is 29 GHz for the p-i-n photodetector and is 19 GHz for the MUTC photodetector. However, most of the difference is due to the difference in $IMD2_n$, $IMD3_n$ powers as a function of frequency. $IMD2_n$ and $IMD3_n$ both steadily decrease as the frequency increases for the p-i-n photodetector. By contrast, $IMD2_n$ increases for the MUTC photodetector up to 10 GHz before starting to decrease, while $IMD3_n$ steadily increases over the entire frequency range. This increase in the distortion products is somewhat unintuitive, but the distortion products in the frequency comb near a given comb line nf_r is obtained from the combined contribution of many signals, so that for example the distortion product $nf_r + (f_1 - f_2)$ will be obtained from the sum of all the signals at $lf_r + f_1$ and $mf_r - f_2$, where l and m are any integers such

87

that $l + m = n$. The distortion products add more coherently in the MUTC pho-
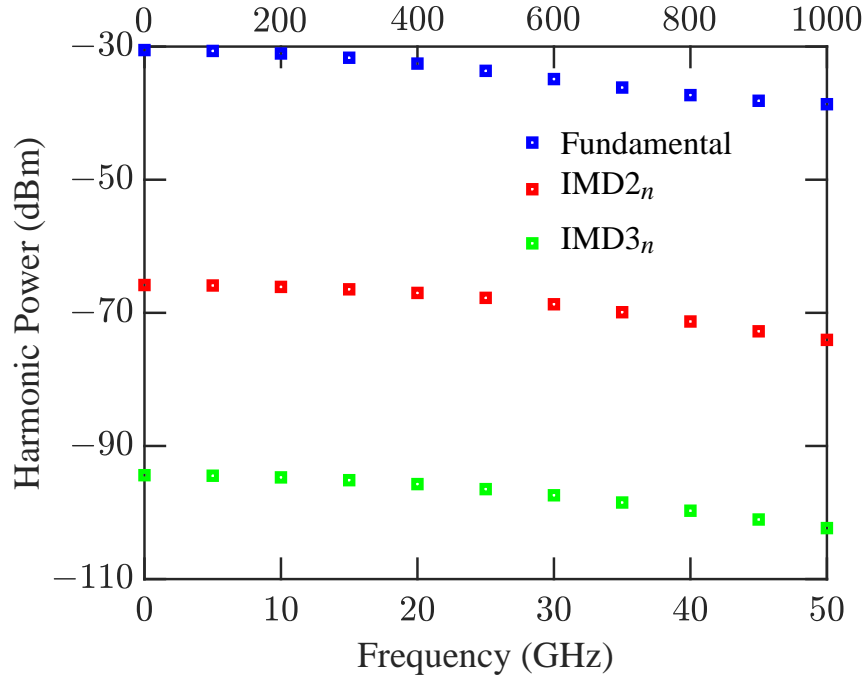
Figure 6.7: Fundamental power, IMD2_n power, and IMD3_n power as a function of frequency in the p-i-n photodetector.

todetector than they do in the p-i-n photodetector. We have verified that IMD2_n and IMD3_n steadily decline up to 50 GHz for the p-i-n photodetector, as shown in Fig. 6.7 when bleaching is included. Hence, this difference in behavior is not due to the difference in the bandwidths of the particular photodetectors that we considered. The current in the MUTC photodetector is almost entirely due to electrons, while the current in the p-i-n photodetector has significant contributions from both electrons and holes flowing in opposite directions. We attribute the lower coherence in the summation of the distortion products at each frequency to the presence of two carriers.

Figures 6.8 and 6.9 show the separate contribution of the electron current, hole
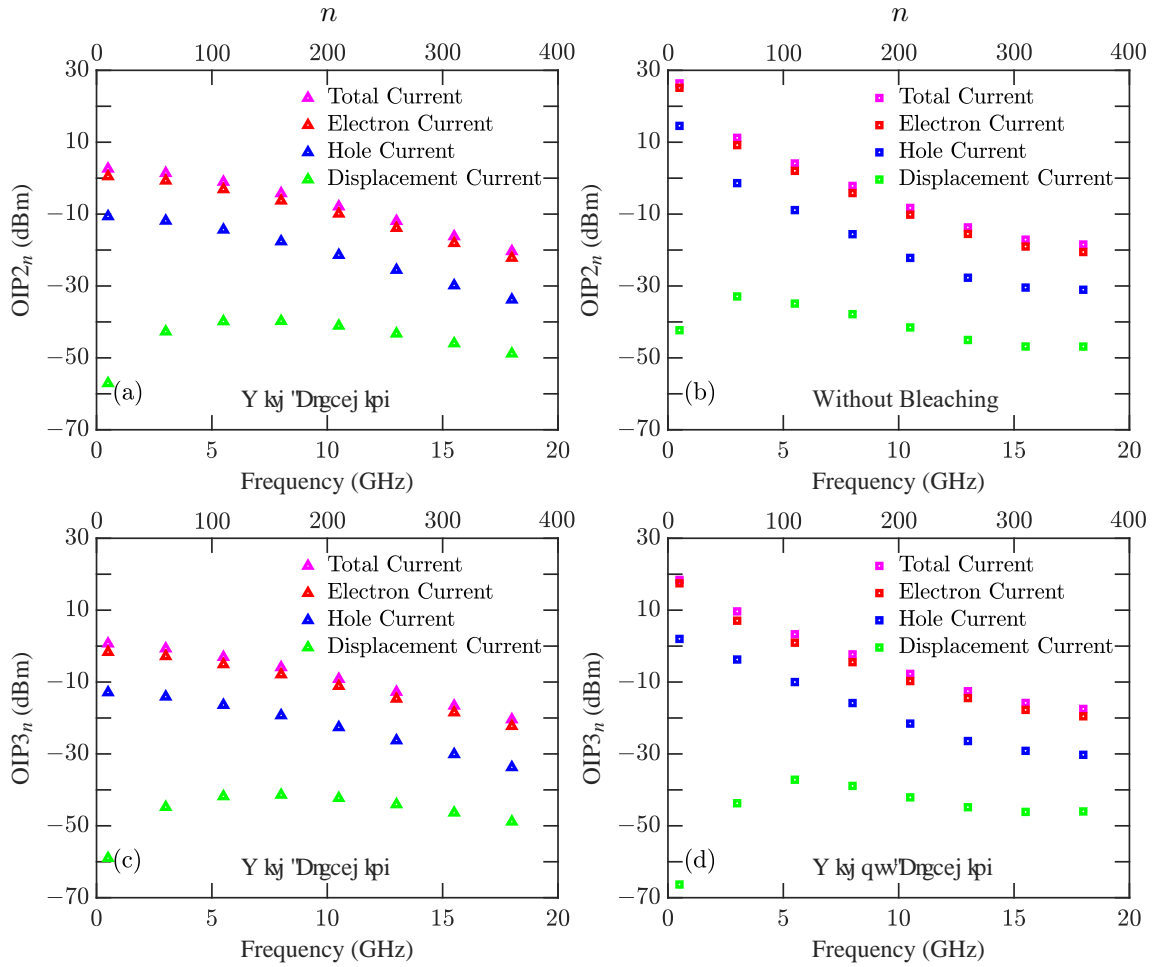
Figure 6.8: Contribution of different current components to $OIP2_n$ and $OIP3_n$ in the MUTC photodetector with $m = 4\%$ with and without bleaching as a function of comb line frequency. The magenta, the red, the blue, and green curves show the contributions of the total, electron, hole, and displacement currents, respectively. (a) $OIP2_n$ with bleaching, (b) $OIP2_n$ without bleaching, (c) $OIP3_n$ with bleaching, (d) $OIP3_n$ without bleaching.

current, and displacement current, as well as the total current as a function of comb line frequency to $OIP2_n$ and $OIP3_n$. We show results for $m = 4\%$ with and without bleaching. Figure 6.8 shows results for the MUTC photodetector, and Fig. 6.9 shows
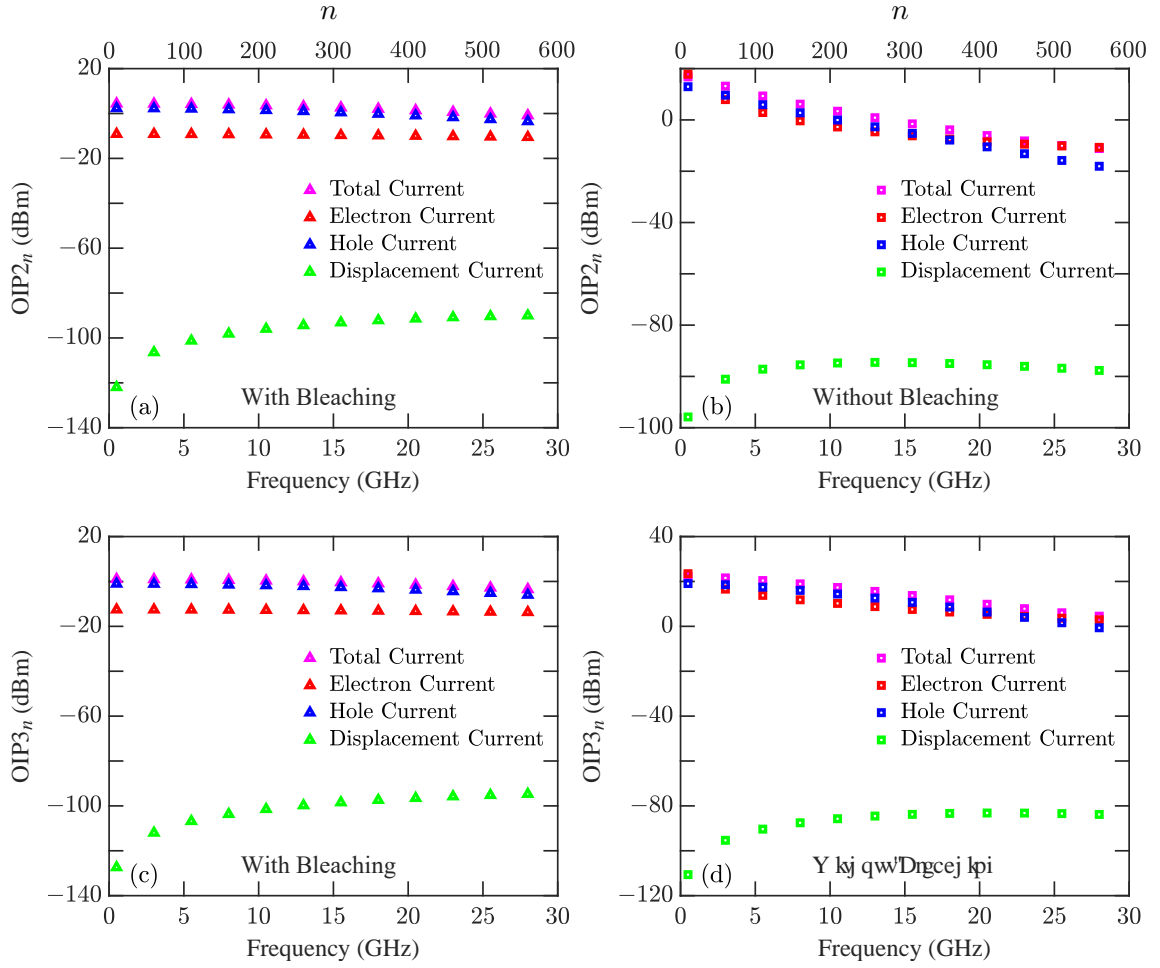
Figure 6.9: Contribution of different current components to $OIP2_n$ and $OIP3_n$ in the p-i-n photodetector with $m = 4\%$ with and without bleaching as a function of comb line frequency. The magenta, the red, the blue, and green curves show the contributions of the total, electron, hole, and displacement currents, respectively. (a) $OIP2_n$ with bleaching, (b) $OIP2_n$ without bleaching, (c) $OIP3_n$ with bleaching, (d) $OIP3_n$ without bleaching.

results for the p-i-n photodetector. Figure 6.8 shows that displacement current does not contribute significantly to either $OIP2_n$ or $OIP3_n$ in the MUTC photodetector. In this figure we show that electron current contributes almost 10 dBm more than

hole current to OIP2_n and OIP3_n with and without bleaching. In MUTC photodetectors, the electrons are the major carriers and holes contribute less to the total current than electrons. Figure 4.7 shows the same behavior of the current components that is visible in Fig. 6.8. Electrons contribute the largest amount to the total current and displacement current contributes the least. We observe in Fig. 6.9 that the displacement current does not play a major role in OIP2_n and OIP3_n in the p-i-n photodetector. Figures 6.9(a) and 6.9(c) show that electron current contributes almost 10 dBm less than hole current to OIP2_n and OIP3_n when bleaching is included. Without bleaching, we find that at comb line frequencies below 2 GHz and beyond 20 GHz, the electron current contributes $\lesssim 5$ dBm more than the hole current, while at comb line frequencies between 2 GHz and 20 GHz the hole current contributes $\lesssim 5$ dBm more than the electron current. This behavior is consistent with Fig. 4.3, which shows that the displacement current does not play a role in the total current and that the electron and hole currents are the major current components.

Figure 6.10 shows the fundamental power S_{in}, the IMD2_n power, and the IMD3_n power in the MUTC photodetector with modulation depths $m = 4\%$ and $m = 8\%$ for $n = 20$ ($nf_r = 1$ GHz) and $n = 200$ ($nf_r = 10$ GHz). In Fig. 6.10, the dotted curves show the harmonic powers when bleaching is not included and solid curves show the harmonic powers when bleaching is included.

Bleaching lowers the fundamental harmonic powers because the responsivity decreases. As shown in Fig. 5.4, this effect becomes more pronounced as the input optical power increases. For lower frequency comb lines, $n \lesssim 50$, we find that the

Figure 6.10: Power at the fundamental frequency (nf_r), the $IMD2_n$ power, and the $IMD3_n$ power in the MUTC photodetector. Solid lines show results with bleaching; dotted lines show results without bleaching: (a) $n = 20$ $(nf_r = 1$ GHz$)$ with $m = 4\%$, (b) $n = 200$ $(nf_r = 10$ GHz$)$ with $m = 4\%$, (c) $n = 20$ $(nf_r = 1$ GHz$)$ with $m = 8\%$, (d) $n = 200$ $(nf_r = 10$ GHz$)$ with $m = 8\%$.

$IMD2_n$ and $IMD3_n$ powers are higher when bleaching is included, but for higher frequency comb lines, the $IMD2_n$ and $IMD3_n$ powers are higher when bleaching is not included. This behavior is due to the change in the impulse response of the photodetector in the frequency domain.

Figure 6.11 shows the fundamental power S_{in}, the $IMD2_n$ power, and the
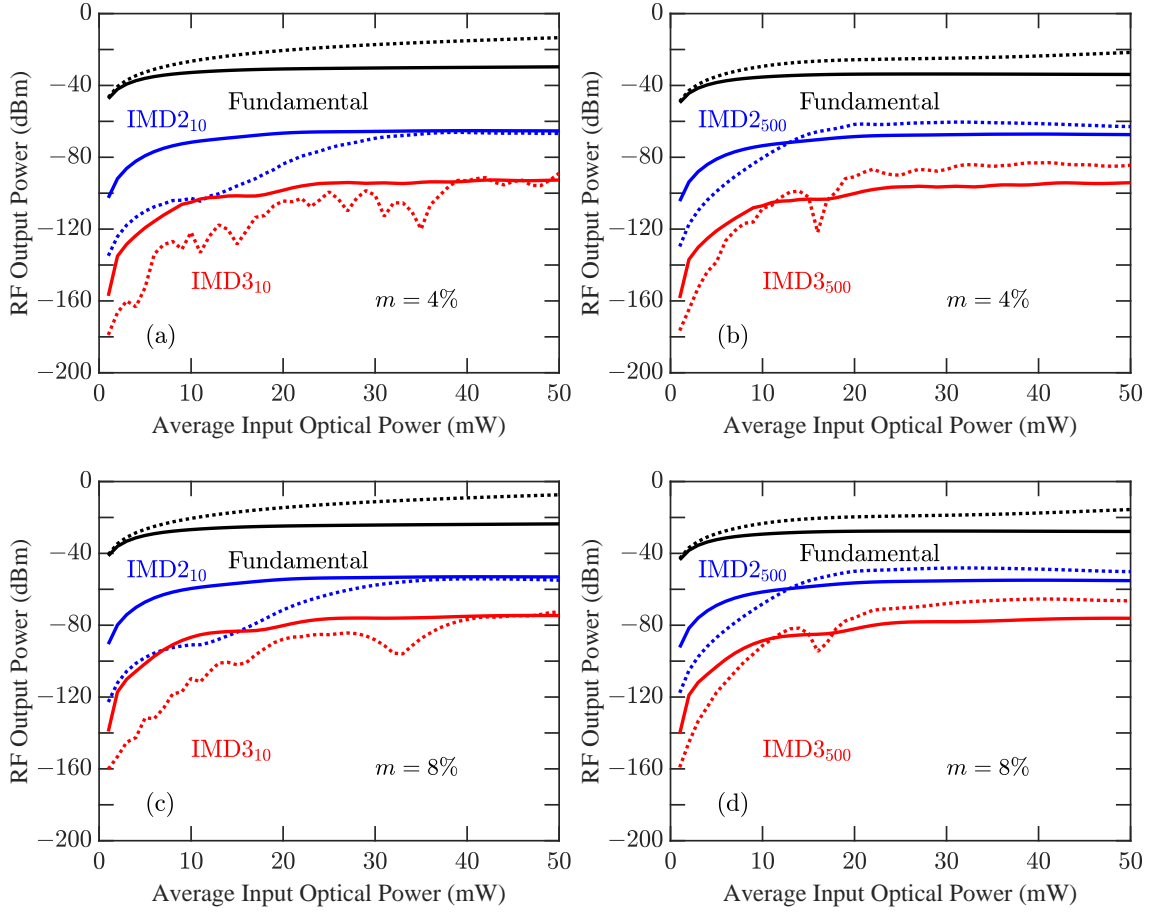
Figure 6.11: Power at the fundamental frequency (nf_r), the IMD2$_n$ power, and the IMD3$_n$ power in the p-i-n photodetector. Solid lines show results with bleaching; dotted lines show results without bleaching: (a) $n = 10$ ($nf_r = 0.5$ GHz) with $m = 4\%$, (b) $n = 500$ ($nf_r = 25$ GHz) with $m = 4\%$, (c) $n = 10$ ($nf_r = 0.5$ GHz) with $m = 8\%$, (d) $n = 500$ ($nf_r = 25$ GHz) with $m = 8\%$.

IMD3$_n$ power in the p-i-n photodetector with modulation depths $m = 4\%$ and $m = 8\%$ for $n = 10$ ($nf_r = 0.5$ GHz) and $n = 500$ ($nf_r = 25$ GHz). In Fig. 6.11, the dotted curves show the harmonic powers when bleaching is not included and solid curves show the harmonic powers when bleaching is included. In the p-i-n photodetector, as in the MUTC photodetector, bleaching lowers the fundamental harmonic

powers because the responsivity decreases. This effect becomes more pronounced as the input optical power increases. For lo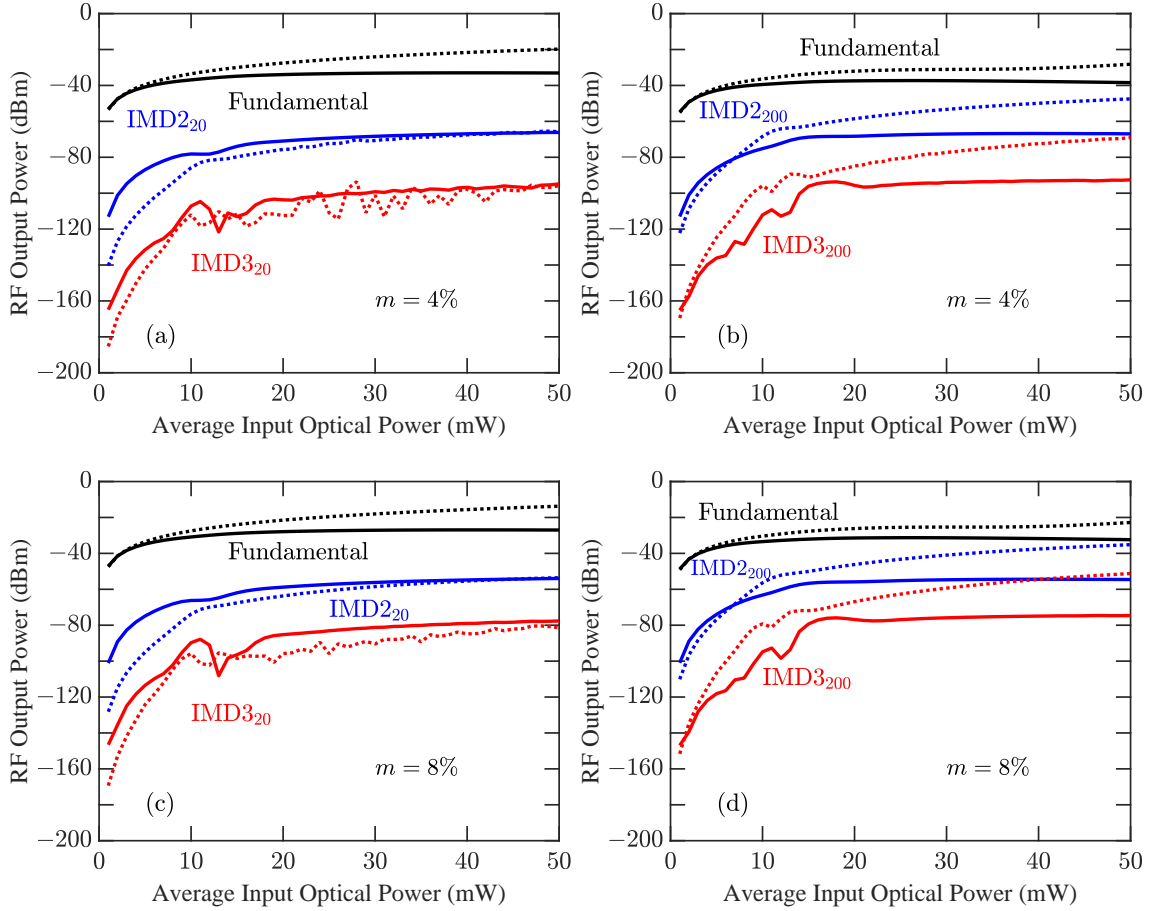wer frequency comb lines, $n \lesssim 100$, we find that the IMD2_n and IMD3_n powers are higher when bleaching is included, but for higher frequency comb lines the IMD2_n and IMD3_n powers are higher when bleaching is not included and that is due to the change of the impulse response of the photodetector.

Figures 6.12 and 6.13 show the distortion-to-signal ratios $\rho_{2n} = \text{IMD2}_n/S_{in}$ and $\rho_{3n} = \text{IMD3}_n/S_{in}$ as a function of comb line frequency. We show results with and without bleaching for modulation depths $m = 4\%$ and $m = 8\%$. Figure 6.12 shows that the ratios ρ_{2n} and ρ_{3n} increase for the MUTC photodetector as the comb line number increases for both $m = 4\%$ and $m = 8\%$. As expected, these ratios are higher for modulation depth $m = 8\%$ by the expected linear and quadratic factors respectively. Figure 6.12 shows that as the comb line number increases, the fraction of each comb line power in IMD2_n and IMD3_n increases, so that the impact of nonlinearity increases. However, these ratios are lower with bleaching at comb line frequencies below 5 GHz ($n \lesssim 100$) than without bleaching. Hence, nonlinearity becomes more important at higher frequencies due to the limited device bandwidth.

Figure 6.13 shows that the ratios ρ_{2n} and ρ_{3n} increase for the p-i-n photodetectors as the comb line number increases for both $m = 4\%$ and $m = 8\%$, but this increase is not noticeable when bleaching is included. These ratios are higher when bleaching is included than when it is not, and the gap decreases as the comb line frequency increases. We also find that these ratios are higher for modulation depth $m = 8\%$. Figure 6.13 shows that as the comb line frequency increases, the fraction
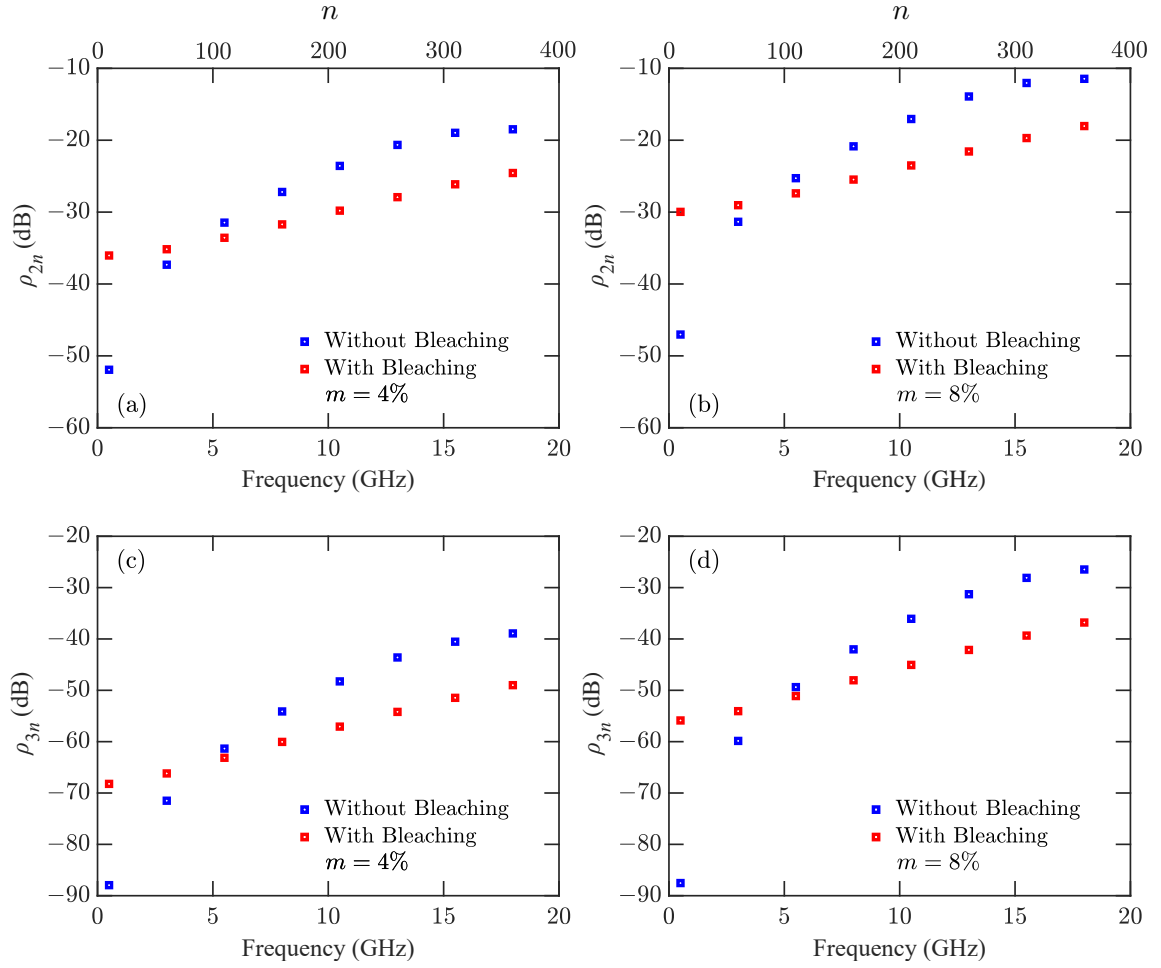
Figure 6.12: The ratio of the IMD2$_n$ and IMD3$_n$ powers to the fundamental power S_{in} in the MUTC photodetector as a function of comb line frequency with and without bleaching, for: (a) ρ_{2n}, $m = 4\%$, (b) ρ_{2n}, $m = 8\%$, (c) ρ_{3n}, $m = 4\%$, (d) ρ_{3n}, $m = 8\%$.

of each comb line power in IMD2$_n$ and IMD3$_n$ increases, so that the impact of non-linearity increases, just as we observed for the MUTC photodetector. However, the increase is not noticeable when bleaching is included in the *p-i-n* photodetector, in contrast to the MUTC photodetector.

Figure 6.14 compares the ratios ρ_{2n} and ρ_{3n} for modulation depths $m = 4\%$
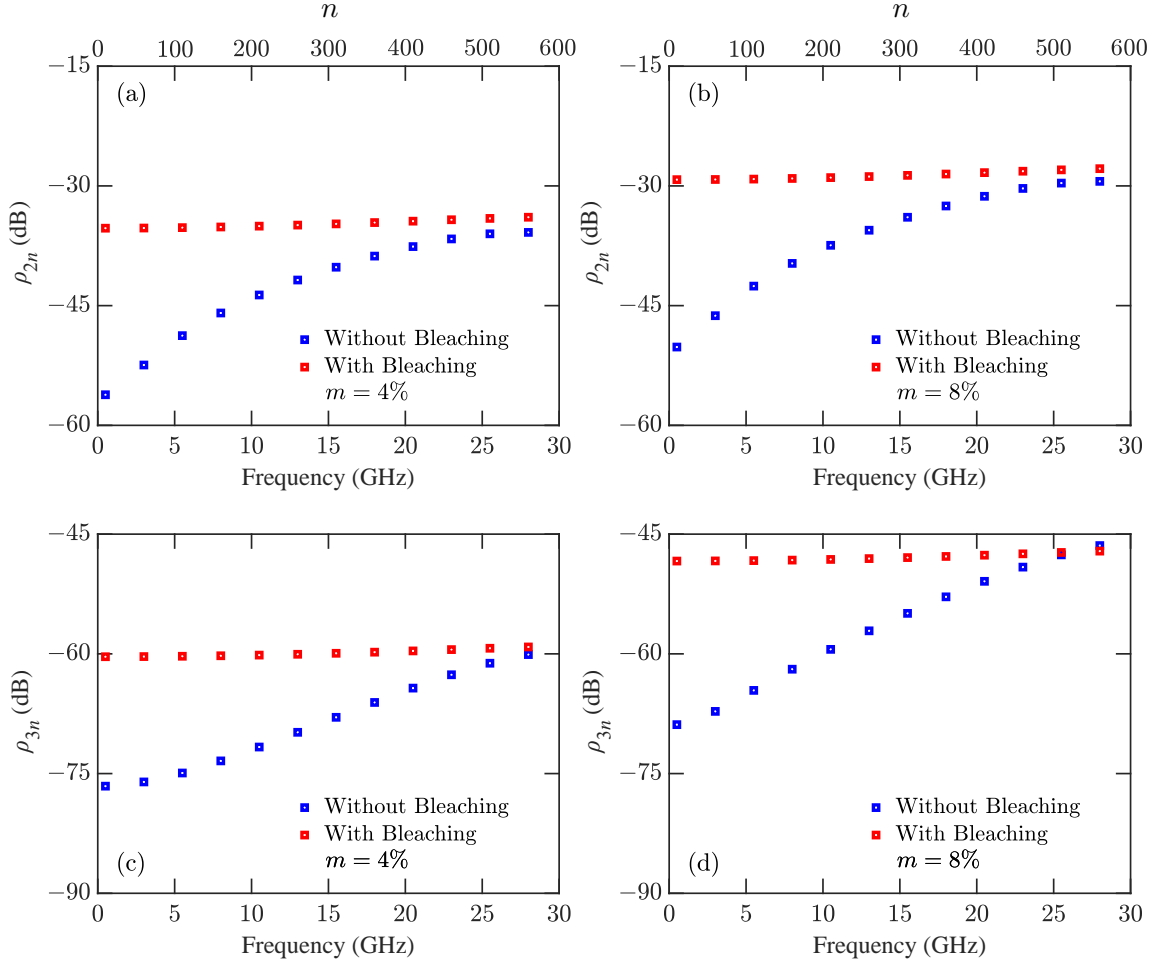
Figure 6.13: The ratio of the IMD2$_n$ and IMD3$_n$ powers to the fundamental power S_{in} in the p-i-n photodetector as a function of comb line frequency with and without bleaching, for: (a) ρ_{2n}, $m = 4\%$, (b) ρ_{2n}, $m = 8\%$, (c) ρ_{3n}, $m = 4\%$, (d) ρ_{3n}, $m = 8\%$.

in the p-i-n and MUTC photodetectors when the bleaching is included. We observe that ρ_{2n} and ρ_{3n} increase rapidly for the MUTC photodetector, while they remain relatively flat for the p-i-n photodetector. We find that ρ_{2n} is smaller for the p-i-n photodetector beyond 3 GHz ($n = 60$), while ρ_{3n} is smaller for the p-i-n photodetector beyond 8 GHz ($n = 160$). The third-order intermodulation products are
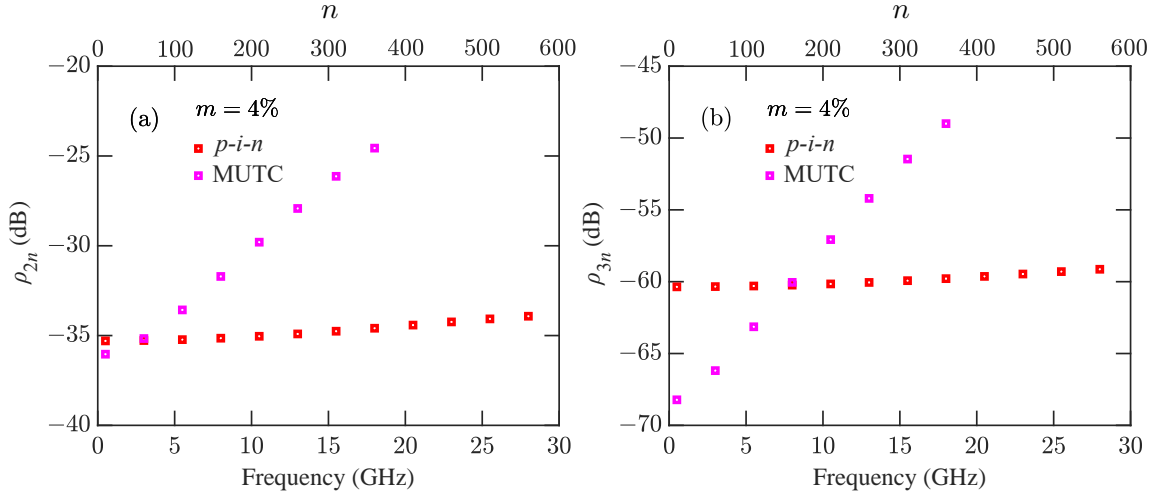
Figure 6.14: The ratio of the IMD2$_n$ and IMD3$_n$ powers to the fundamental power S_{in} in the MUTC and p-i-n photodetectors as a function of comb line frequency when bleaching is included. (a) IMD2$_n$/S_{in}, (b) IMD3$_n$/S_{in}.

particularly important because these products can overlap and thus interfere with the fundamental frequencies. We conclude that nonlinear distortion has less impact at low frequencies in the MUTC photodetector than it does in the p-i-n photodetector, but the opposite is true at higher frequencies.

Figures 6.15 and 6.16 show the separate contribution of the electron current, hole current, and displacement current, as well as the total current as a function of comb line frequency to ρ_{2n} and ρ_{3n}. Figures 6.15(a) and 6.15(c) show that with bleaching all the current components make a comparable contribution in the MUTC photodetector to ρ_{2n} and ρ_{3n}. By contrast, Figs. 6.15(b) and 6.15(d) show that when bleaching is not included the contribution of displacement current to the ratios ρ_{2n} and ρ_{3n} is higher than the contribution due to the electron and hole currents at comb
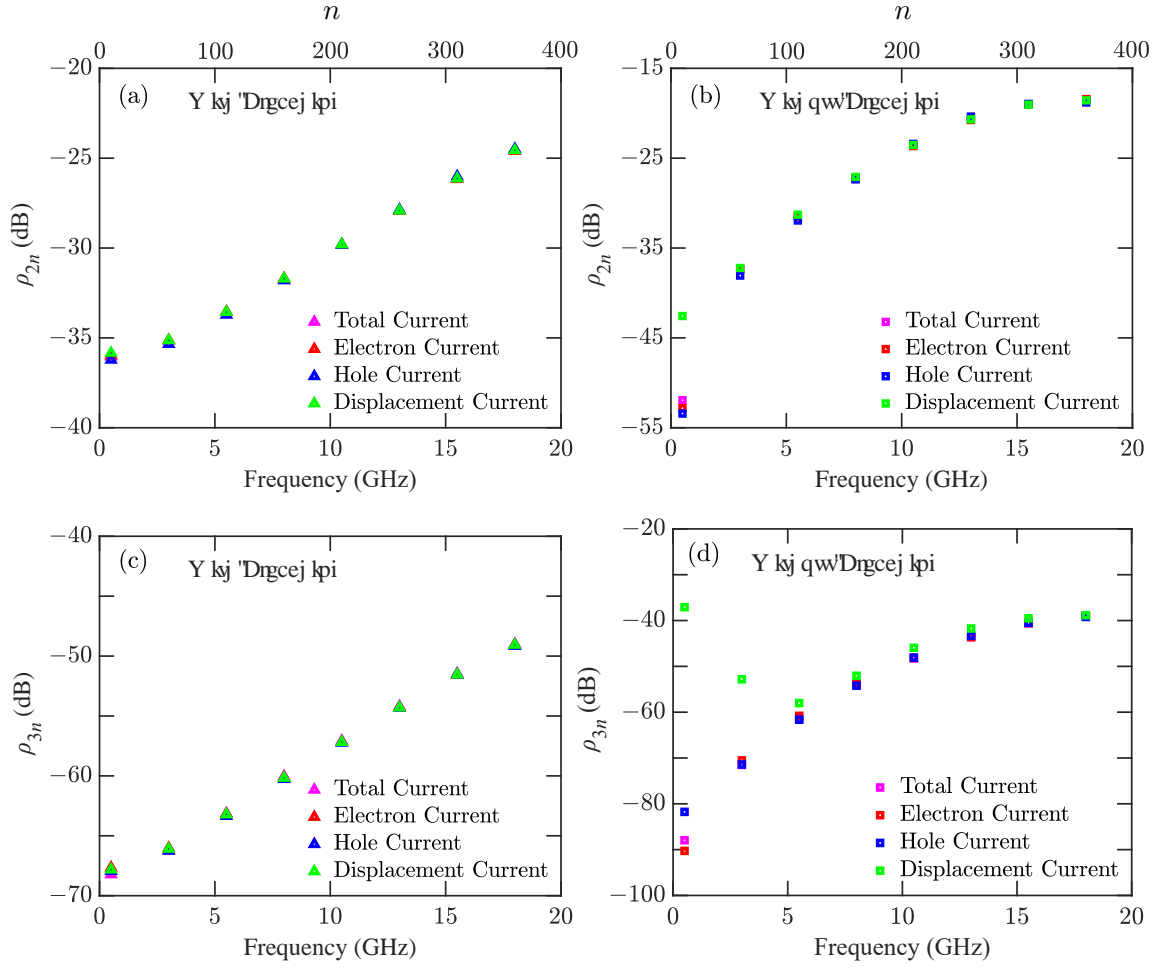
Figure 6.15: The contribution of different currents to the ratios ρ_{2n} and ρ_{3n} in the MUTC photodetector with $m = 4\%$ with and without bleaching as a function of comb line frequency. The magenta, the red, the blue, and green curves show the contributions of the total current, electron current, hole current, and displacement current, respectively. (a) ρ_{2n} with bleaching, (b) ρ_{2n} without bleaching, (c) ρ_{3n} with bleaching, (d) ρ_{3n} without bleaching.

line frequencies below 5 GHz. Figures 6.16(a) and 6.16(c) show that displacement current does not contribute strongly to ρ_{2n} and ρ_{3n} in the p-i-n photodetector when bleaching is included. The contribution of the displacement current is almost 3 dB
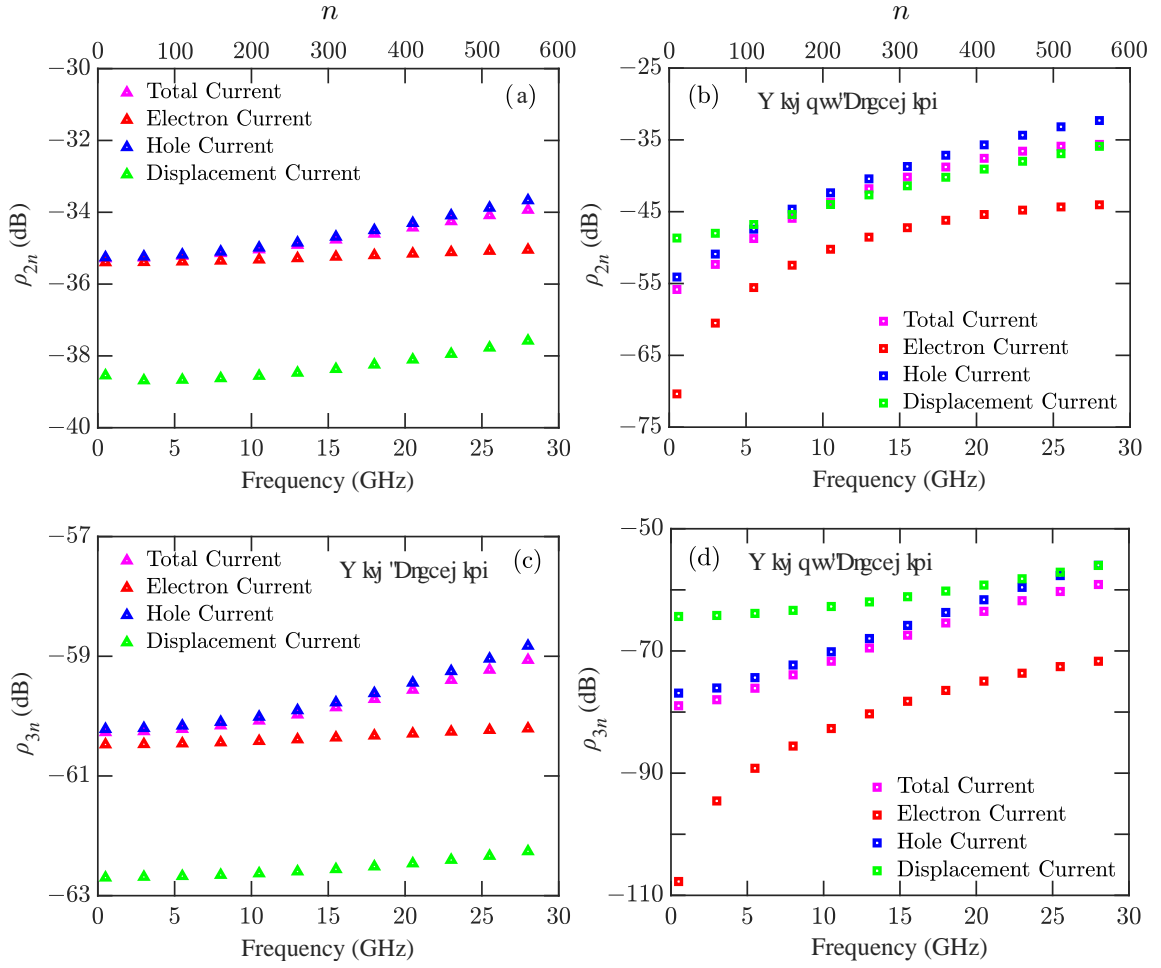
Figure 6.16: The contribution of different currents to the ratios ρ_{2n} and ρ_{3n} in the *p-i-n* photodetector with $m = 4\%$ with and without bleaching as a function of comb line frequency. The magenta, the red, the blue, and green curves show the contributions of the total current, electron current, hole current, and displacement current, respectively. (a) ρ_{2n} with bleaching, (b) ρ_{2n} without bleaching, (c) ρ_{3n} with bleaching, (d) ρ_{3n} without bleaching.

below the contributions due to electron and hole currents. Moreover, the contributions to ρ_{2n} and ρ_{3n} due to the electron current are lower than the contributions due to the hole current, and as the comb line frequency increases, the gap between

these contributions increases. Figures 6.16(b) and 6.16(d) show that displacement current makes the largest contribution to ρ_{2n} at comb line frequencies below 5 GHz ($n \lesssim 100$) when bleaching is not included. It is also the largest contribution to ρ_{3n}. As can be seen from these figures, the electron current contribution to ρ_{2n} and ρ_{3n} is almost 10 dBm less than the contribution of the displacement and hole currents when bleaching is not included.

The principal effect of bleaching is to lower the responsivity, which decreases the number of electrons in the device. The decrease in the electron number becomes more pronounced when the input power increases, as a result of which the fundamental comb powers S_{in} and the intermodulation products eventually saturate as the input optical power increases. Simultaneously, the smaller number of electrons in the device lowers the nonlinearity due to space charge effects. We find that the OIP2$_n$ and OIP3$_n$ powers decrease as n increases in both the MUTC photodetector and the p-i-n photodetector whether or not bleaching is included. However, in the MUTC photodetector, the impact of bleaching is strongest at lower comb line frequencies and almost disappears at comb line frequencies between 10 GHz and 17 GHz and reappears again at comb line frequencies beyond 17 GHz.

As a consequence, the impact of bleaching on the ratios ρ_{2n} and ρ_{3n} is complex and not always detrimental. In the MUTC photodetector, when $n \lesssim 100$ ($\lesssim 5$ GHz), we find that the ratio is higher when bleaching is included. On the other hand, when $n \gtrsim 100$ ($\gtrsim 5$ GHz), the ratio is lower when bleaching is included, so that bleaching actually improves this ratio at comb line frequencies beyond 5 GHz. In the p-i-n photodetector the ratio is always higher when bleaching is included. We cal-

culated the separate contributions of the electron, hole, and displacement currents, as well as the total current to ρ_{2n} and ρ_{3n}. The results that we present in Figs. 6.12 and 6.13 imply that the p-i-n photodetector has higher distortion-to-signal ratios than does the MUTC photodetector at low comb line frequencies. Additionally, we find that bleaching reduces these ratios at higher comb line frequencies in the MUTC photodetector.

However, lower responsivity implies a lower signal-to-noise ratio. Hence, we expect the impact of noise to increase. This issue should be investigated in the future.

Chapter 7

Conclusion

In this dissertation, we theoretically studied the performance of a single hetero-junction p-i-n photodetector and a modified uni-traveling carrier (MUTC) photodetector using the drift-diffusion equations. We first reviewed the basic equations and the computational method that we used to solve these equations. Our model includes contributions from the Franz-Keldysh effect and non-local impact ionization, as well as empirical models of mobility and diffusion for both electrons and holes.

We used our drift-diffusion model to calculate the impulse response of both a p-i-n and an MUTC photodetector and the phase noise of the MUTC photodetector. In the drift-diffusion equations, we perturbed the optical generation rate by ΔG_{opt}, and we then calculated the impulse response of both the p-i-n and MUTC photodetectors due to this perturbation. We found that in the p-i-n photodetector, the electron current dominates the total current at times up to 70 fs, but the hole current dominates the total current at later times, and the displacement current is always negligible. The calculated quantum efficiency of the p-i-n photodetector is $\eta = 64\%$ and the 3-dB cut-off frequency is 24 GHz, which are in good agreement with experimental results [43]. By contrast to the p-i-n photodetector, we found that the displacement current cannot be neglected in the MUTC photodetector since it dominates the total current for the first 50 fs. Thereafter, the electron

current dominates at all times. The calculated quantum efficiency of the MUTC photodetector is $\eta = 56\%$, and the 3-dB cut-off frequency is 25 GHz, which are in excellent agreement with the experiments by Li *et al.* [42].

We next used the impulse response of the device to calculate the phase noise in the MUTC photodetector. Agreement with prior experiments and Monte Carlo simulations was excellent. Our approach is computationally faster than Monte Carlo simulations by many orders of magnitude. Hence, this approach makes it possible to optimize the device parameters in order to reduce the phase noise. Using our method, we modified the design of Li *et al.* [42] to obtain a structure with at least 1.4 dBc/Hz lower phase noise and reduced nonlinearity.

We developed an empirical model of bleaching based on experimental data that were collected at the Naval Research Laboratory, and we incorporated this model into the 1-D drift-diffusion equations to calculate the responsivity. We determined the parameters of the bleaching model in the pulsed mode and the CW mode for the *p-i-n* photodetector and in the pulsed mode for the MUTC photodetector. We included the bleaching in our drift-diffusion model to study nonlinearity in *p-i-n* and MUTC photodetectors in the pulsed mode.

We calculated the impact of bleaching on device nonlinearity as a function of the average optical power. We modeled the three-tone modulation technique to calculate IMD2, IMD3 in the pulsed mode. We calculated OIP2, and OIP3 to characterize IMD2 and IMD3 and determined the effect of bleaching on the nonlinearity of the *p-i-n* and MUTC photodetectors as a function of average input optical power. The output of modulated optical pulse trains in the photodetector is a set of fre-

quency comb lines in the frequency domain. In contrast with a CW input, for which there is one IMD2 and one IMD3, each comb line has its own IMD2 and IMD3. We determined the behavior of IMD2_n, IMD3_n, OIP2_n, and OIP3_n for each comb line n with and without bleaching. We found that in both p-i-n and MUTC photodetectors OIP2_n, and OIP3_n occur at a lower power when bleaching is included than when it is not. The gap is larger for low comb line numbers. OIP2_n, and OIP3_n decrease both with and without bleaching when n increases, but this decrease is noticeably slower when bleaching is included. In the MUTC photodetector this decrease is large at low frequencies, becomes almost negligible at 15 GHz, and increases again at frequencies beyond 15 GHz. We also found that when bleaching is included, OIP2_n and OIP3_n are higher in the p-i-n photodetector than the MUTC photodetector and the difference between them increases as comb line number increases. We determined the contribution of electron current, hole current, and displacement current to OIP2_n and OIP3_n in both the p-i-n and MUTC photodetector. We found that in the MUTC photodetector displacement current does not play a major role both in OIP2_n and OIP3_n, and electron current contributes almost 10 dBm more than hole current in OIP2_n and OIP3_n, both with and without bleaching. In MUTC photodetectors, electrons are major carriers and holes contribute less to the total current than electrons. We found that in the p-i-n photodetector displacement current does not play a major role in OIP2_n and OIP3_n, and the electron current contributes almost 10 dBm less than the hole current to OIP2_n and OIP3_n with bleaching. Electron and hole contribution are more complicated when bleaching is not included. At comb line frequencies below 2 GHz and beyond 20 GHz, the electron current contributes

$\lesssim 5$ dBm more than hole current and at comb line frequencies between 2 GHz and 20 GHz, the hole current contributes $\lesssim 5$ dBm more than the electron current to $OIP2_n$ and $OIP3_n$.

We calculated the distortion-to-signal ratios $\rho_{2n} = IMD2_n/S_{in}$ and $\rho_{3n} = IMD3_n/S_{in}$ as a function of comb line frequency with and without bleaching. We found that these ratios increase as the comb line number increases, which implies that the fraction of each comb line power in $IMD2_n$ and $IMD3_n$ increases. Hence, the impact of nonlinearity becomes larger as the comb line number increases. The rate of increase is slower in the p-i-n photodetector that we studied than the MUTC photodetector.

We determined the separate contributions of the electron, hole, and displacement currents to the ρ_{2n} and ρ_{3n} as a function of comb line frequency with and without bleaching in both the p-i-n and MUTC photodetector. We showed that in the MUTC photodetector all the current components make similar contributions to ρ_{2n} and ρ_{3n} when bleaching is included. By contrast, the contribution of the displacement current to the ratios ρ_{2n} and ρ_{3n} is higher than the contributions from the electron and hole currents for comb line frequencies below 5 GHz when bleaching is not included. We also found that the displacement current does not contribute significantly to ρ_{2n} and ρ_{3n} in the p-i-n photodetector when bleaching is included. The contribution due to the displacement current is almost 3 dB below the contributions due to the electron and hole currents. On the other hand, the displacement current makes a significant contribution to ρ_{2n} at comb line frequencies below 5 GHz ($n \lesssim 100$), and it also makes the dominant contribution to ρ_{3n} when bleaching is not

included. We found that the electron current contribution to ρ_{2n} and ρ_{3n} is always less than the contribution from the displacement and hole currents when bleaching is not included.

The impact of bleaching on the ratios ρ_{2n} and ρ_{3n} is complex and not always detrimental. In the MUTC photodetector, when $n \lesssim 100$ ($\lesssim 5$ GHz), we found that the ratio is higher with bleaching. On the other hand, when $n \gtrsim 100$ ($\gtrsim 5$ GHz), the ratio is lower with bleaching, so that bleaching actually improves this ratio. In the p-i-n photodetector the ratio is always higher with bleaching.

Our results imply that the impact of nonlinear distortion is greater for the p-i-n photodetector than it is for the MUTC photodetector at low comb line frequencies, while the reverse is true at high comb line frequencies. Additionally, bleaching reduces distortion-to-signal ratios at higher comb line frequencies in the MUTC photodetector.

Bibliography

[1] M. N. Draa, A. S. Hastings, and K. J. Williams, "Comparison of photodiode nonlinearity measurement systems," Opt. Express **19**, 12635–12645 (2011).

[2] Bahaa E. A. Saleh and Malvin Carl Teich, *Fundamentals of Photonics* (Wiley, 1991).

[3] S. Bhadra and A. Ghatak, *Guided Wave Optics and Photonic Devices* (CRC, 2016).

[4] S. M. Sze, and M. K. Lee, *Semiconductor Devices: Physics and Technology* (Wiley, 2012).

[5] M. Razeghi, *The MOCVD Challenge: A Survey of GaInAsP-InP and GaInAsP-GaAs for Photonic and Electronic Device Applications* (CRC, 2010).

[6] B. Nabet, *Photodetectors: Materials, Devices and Applications* (Woodhead, 2015).

[7] R. H. Kingston, *Detection of Optical and Infrared Radiation* (Springer, 1978).

[8] C. H. Cox, *Analog Optical Links: Theory and Practice* (Cambridge University Press, 2004).

[9] J. M. Liu, *Photonic Devices* (Cambridge University Press, 2009).

[10] R. F. Pierret, *Semiconductor Device Fundamentals* (Addison-Wesley, 1996).

[11] A. Yariv and P. Yeh, *Photonics: Optical Electronics in Modern Communications* (Oxford University Press, 2007).

[12] K. J. Williams, R. D. Esman, and M. Dagenais, "Effects of high space-charge fields on the response of microwave photodetectors," IEEE Photon. Technol. Lett. **6**, 639–641 (1994).

[13] K. J. Williams, R. D. Esman, and M. Dagenais, "Nonlinearities in p-i-n microwave photodetectors," J. Lightw. Technol. **14**, 84–96 (1996).

[14] Y.-L. Huang and C.-K. Sun, "Nonlinear saturation behaviors of high-speed p-i-n photodetectors," J. Lightw. Technol. **18**, 203–212 (2000).

[15] J. Guo, Y. Zuo, Y. Zhang, W. Ding, B. Cheng, J. Yu, and Q. Wang, "Simulation research of nonlinear behavior induced by the charge-carrier effect in resonantcavity-enhanced photodetectors," J. Lightw. Technol. **25**, 2783–2790 (2007).

[16] H. Jiang, D. S. Shin, G. L. Li, T. A. Vang, D. C. Scott, and P. K. L. Yu, "The frequency behavior of the third-order intercept point in a waveguide photodiode," IEEE Photon. Technol. Lett. **12**, 540–542 (2000).

[17] S. P. Wilson, A. B. Walker, "One- and two-dimensional models of the transient response of metal semiconductor metal photodetectors including diffraction," Semiconduct. Sci. Technol. **12**, 1265–1272 (1997).

[18] J. Harari, F. Journet, O. Rabii, G. Jin, J. P. Vilcot, and D. Decoster, "Modeling of waveguide PIN photodetectors under very high optical power," IEEE Trans. Microw. Theory Tech. **43**, 2304–2310 (1995).

[19] A. Afzalian and D. Flandre, "Physical modeling and design of thin-film SOI lateral PIN photodiodes," IEEE Trans. Electron Devices **52**, 1116–1122 (2005).

[20] S. P. Wilson and A. B. Walker, "Mechanism of impact ionization enhancement in GaAs p-i-n diodes under high illumination conditions," Semiconduct. Sci. Technol. **13**, 190–193 (1998).

[21] Y. Fu, H. Pan, Z. Li, A. Beling, and J. C. Campbell, "Characterizing and modeling nonlinear intermodulation distortions in modified uni-traveling carrier photodiodes," IEEE J. Quantum Electron. **47**, 1312–1319 (2011).

[22] Y. Hu, B. S. Marks, C. R. Menyuk, V. J. Urick, and K. J. Williams, "Modeling sources of nonlinearity in a simple p-i-n photodetector," J. Lightwave Technol. **32**, 3710–3720 (2014).

[23] Y. Hu, C. R. Menyuk, M. N. Hutchinson, V. J. Urick, and K. J. Williams, "Frequency dependent harmonic powers in a modified uni-traveling carrier photodetector," Opt. Lett. **42**, 919–922 (2017).

[24] Y. Hu, C. R. Menyuk, X. Xie, M. N. Hutchinson, V. J. Urick, J. C. Campbell, and K. J. Williams, "Computational study of amplitude-to-phase conversion

in a modified unitraveling carrier (MUTC) Photodetector," IEEE Photon. J. **9**, 1–11 (2017).

[25] Alwyn J. Seeds, "Microwave photonics," IEEE Trans. Microw. Theory Techn. **50**, 877–887 (2002).

[26] T. R. Clark, M. Currie, and P. J. Matthews, "Digitally linearized wide-band photonic link," J. Lightw. Technol. **19**, 172–179 (2001).

[27] C. H. Cox, E. I. Ackerman, G. E. Betts, and J. L. Prince, "Limits on the performance of RF-over-fiber links and their impact on device design," IEEE Trans. Microw. Theory Techn. **54**, 906–920 (2006).

[28] V. J. Urick, Keith J. Williams, and Jason D. McKinney, *Fundamentals of Microwave Photonics* (Wiley, 2015).

[29] J. D. McKinney and K. J. Williams, "Sampled analog optical links," IEEE Trans. Microw. Theory Techn. **57**, 2093–2099 (2009).

[30] R. T. Schermer and J. D. McKinney, "Disambiguation of Sub-Sampled Photonic Links by Acousto-Optic Delay Modulation," in IEEE Avionics and Vehicle Fiber-Optics and Photonics Conference (IEEE, 2017), pp. 35–36.

[31] R. T. Schermer and J. D. McKinney, "Non-uniform sub-nyquist optical sampling by acousto-optic delay modulation," J. Lightw. Technol. **36**, 5058–5066 (2018).

[32] S. R. Harmon and J. D. McKinney, "Precision broadband RF signal recovery in subsampled analog optical links," IEEE Photon. Technol. Lett. **27**, 620–623 (2014).

[33] W. C. Black and D. A. Hodges, "Time interleaved converter arrays," IEEE J. Solid-State Circuits **15**, 1022–1029 (1980).

[34] R. Venkataramani and Y. Bresler, "Perfect reconstruction formulas and bounds on aliasing error in sub-Nyquist nonuniform sampling of multiband signals," IEEE Trans. Inf. Theory **46**, 2173–2183 (2000).

[35] C. Vogel and H. Johansson, "Time-interleaved analog-to-digital converters: Status and future directions," in IEEE International Symposium on Circuits and Systems (IEEE, 2006), pp. 3386–3389.

[36] I. Coddington, N. Newbury, and W. Swann, "Dual-comb spectroscopy," Optica **3**, 414–426 (2016).

[37] S. R. Harmon and J. D. McKinney, "Broadband RF disambiguation in subsampled analog optical links via intentionally-introduced sampling jitter," Opt. Express **22**, 23928–23937 (2014).

[38] A. Aldroubi and K. Grochenig, "Nonuniform sampling and reconstruction in shift-invariant space," SIAM Rev. **43**, 585–620 (2001).

[39] J. A. Tropp, J. N. Laska, M. F. Duarte, J. K. Romberg, and R. G. Baraniuk, "Beyond nyquist: efficient sampling of sparse bandlimited signals," IEEE Trans. Inf. Theory **56**, 520–544, (2009).

[40] R. Maleh, G. L. Fudge, F. A. Boyle, and P. E. Pace, "Analog-to-information and the Nyquist folding receiver," IEEE J. Emerging Sel. Top. Circuits Syst. **2**, 564–578 (2012).

[41] T. Ishibashi, N. Shimizu, S. Kodama, H. Ito, T. Nagatsuma and T. Furuta, "Uni-traveling-carrier photodiodes," in Ultrafast Electronics and Optoelectronics, Vol. 13 of 1997 OSA Trends in Optics and Photonics Series (Optical Society of America, 1997), paper UC3.

[42] Z. Li, H. Pan, H. Chen, A. Beling, and J. C. Campbell, "High-saturation-current modified uni-traveling-carrier photodiode with cliff layer," IEEE J. Quantum Electron. **46**, 626–632 (2010).

[43] K. J. Williams, "Microwave nonlinearities in photodiodes," PhD Dissertation, University of Maryland College Park, Maryland, USA, 1994.

[44] P. W. Juodawlkis, F. J. O'Donnell, J. J. Hargreaves, D. C. Oakley, A. Napoleone, S. H. Groves, L. J., Molvar, K. M. Mahoney, L. J. Missaggia, J. P. Donnelly, R. C. Williamson, and J. C. Twichell, "Absorption saturation nonlinearity in InGaAs/InP p-i-n photodiodes," in 15th Annual Meeting of the IEEE Lasers and Electro Optics Society (IEEE, 2002), pp. 426–427.

[45] F. Quinlan, T. M. Fortier, H. Jiang, and S. A. Diddams, "Analysis of shot noise in the detection of ultrashort optical pulse trains," J. Opt. Soc. Am. B **30**, 1775–1785 (2013).

[46] F. Quinlan, T. M. Fortier, H. Jiang, A. Hati, C. Nelson, Y. Fu, J. C. Campbell, and S. A. Diddams, "Exploiting shot noise correlations in the photodetection of ultrashort optical pulse trains," Nat. Photonics **7**, 290–293 (2013).

[47] W. Sun, F. Quinlan, T. M. Fortier, J. D. Deschenes, Y. Fu, S. A. Diddams, and J. C. Campbell, "Broadband noise limit in the photodetection of ultralow jitter optical pulses," Phys. Rev. Lett. **113**, 203901 (2014).

[48] S. E. Jamali Mahabadi and C. R. Menyuk, "Calculation of the impulse response of PIN and MUTC photodetectors using the drift-diffusion equations," in Laser Science (Optical Society of America, 2017), paper JTu2A-53.

[49] S. E. Jamali Mahabadi, F. J. Quinlan, T. F. Carruthers, and C. R. Menyuk, "Phase noise and performance optimization in MUTC photodetectors using the drift-diffusion equations," in IEEE Photonics Conference (IEEE, 2018), pp. 1–2.

[50] S. E. Jamali Mahabadi, T. F. Carruthers, and C. R. Menyuk, "Modeling phase noise in high-power photodetectors," in IEEE International Conference on Numerical Simulation of Optoelectronic Devices (IEEE, 2019), pp. 65–66.

[51] S. E. J Mahabadi, S. Wang, T. F. Carruthers, C. R. Menyuk, F. J. Quinlan, M. N. Hutchinson, J. D. McKinney, and K. J. Williams, "Calculation of the impulse response and phase noise of a high-current photodetector using the drift-diffusion equations," Opt. Express **27**, 3717–3730 (2019).

[52] S. E. Jamali Mahabadi, T. F. Carruthers, C. R. Menyuk, M. N. Hutchinson, J. D. McKinney, and K. J. Williams, "Impact of nonlinearity on RF-modulated frequency combs with different modulation depths in an MUTC photodetector," in IEEE International Topical Meeting on Microwave Photonics (IEEE, 2019), pp. 1–4.

[53] S. E. Jamali Mahabadi, T. F. Carruthers, C. R. Menyuk, M. N. Hutchinson, J. D. McKinney, and K. J. Williams, "Impact of nonlinearity in an MUTC photodetector on an RF-modulated frequency comb," in IEEE Photonics Conference (IEEE, 2019), pp. 1–2.

[54] S. E. Jamali Mahabadi, T. F. Carruthers, C. R. Menyuk, J. D. McKinney, and K. J. Williams, "Impact on frequency combs of nonlinearity including bleaching in p-i-n photodetectors," in IEEE Photonics Society Summer Topical Meeting Series (IEEE, 2020), pp. 1–2.

[55] Y. Hu, "Modeling Nonlinearity and Noise in High-Current Photodetectors," Ph.D. Dissertation, University of Maryland, Baltimore County, Maryland, USA, 2017.

[56] H. Ito, S. Kodama, Y. Muramoto, T. Furuta, T. Nagatsuma, and T. Ishibashi, "High-speed and high-output InP-InGaAs unitraveling-carrier photodiodes," IEEE J. Sel. Topics Quantum Electron. **10**, 709–727 (2004).

[57] E. Rouvalis, M. Chtioui, F. van Dijk, F. Lelarge, M. J. Fice, C. C. Renaud, G. Carpintero, and A. J. Seeds, "170 GHz uni-traveling carrier photodiodes

for InP-based photonic integrated circuits," Opt. Express **20**, 20090–20095 (2012).

[58] G. M. Dunn, A. B. Walker, A. J. Vickers, and V. R. Wicks, "Transient response of photodetectors," J. Appl. Phys. **79**, 7329–7338 (1996).

[59] M. Dentan and B. de Cremoux, "Numerical simulation of the nonlinear response of a *p-i-n* photodiode under high illumination," J. Lightw. Technol. **8**, 1137–1144 (1990).

[60] K. J. Williams, R. D. Esman, R. B. Wilson, and J. D. Kulick, "Differences in *p*-side and *n*-side illuminated *p-i-n* photodiode nonlinearities," IEEE Photon. Technol. Lett. **10**, 132–134 (1998).

[61] S. P. Wilson, S. J. Woods, and A. B. Walker "Modelling of *p-i-n* photodiodes under high illumination conditions," Int. J. Numer. Modell. Electron. Netw. Devices Fields **10**, 139–151 (1997).

[62] S. J. Woods, S. P. Wilson, and A. B. Walker, "Non-unique solutions in drift diffusion modelling of phototransistors," Int. J. Numer. Modell. Electron. Netw. Devices Fields **13**, 37–57 (2000).

[63] T. H. Windhorn, L. W. Cook, and G. E. Stillman, "Temperature dependent electron velocity-field characteristics for $In_{0.53}Ga_{0.47}As$ at high electric fields," J. Electron. Mater. **11**, 1065–1082 (1982).

[64] P. Hill, J. Schlafer, W. Powazinik, M. Urban, E. Eichen, and R. Olshansky, "Measurement of hole velocity in n-type InGaAs," Appl. Phys. Lett. **50**, 1260-1262 (1987).

[65] K. W. Böer, *Survey of Semiconductor Physics* (Van Nostrand Reinhold, 1990).

[66] C. Hilsum, "Simple empirical relationship between mobility and carrier concentration," Electron. Lett. **10**, 259–260 (1974).

[67] K. W. Böer, "High-field carrier transport in inhomogeneous semiconductors," Annalen der Physik **7**, 371–393 (1985).

[68] M. Razeghi, *Fundamentals of Solid State Engineering* (Springer, 2006).

[69] K. Yang, J. C. Cowles, J. R. East, and G. I. Haddad, "Theoretical and experimental dc characterization of InGaAs-based abrupt emitter HBT's," IEEE Trans. Electron Devices **42**, 1047–1058 (1995).

[70] H. Wang and G.-I. Ng, "Avalanche multiplication in InP/InGaAs double heterojunction bipolar transistors with composite collectors," IEEE Trans. Electron Devices **47**, 1125–1133 (2000).

[71] K. Horio and H. Yanai, "Numerical modeling of heterojunctions including the thermionic emission mechanism at the heterojunction interface," IEEE Trans. Electron Devices **37**, 1093–1098 (1990).

[72] B. K. Crone, P. S. Davids, I. H. Campbell, and D. L. Smith, "Device model investigation of bilayer organic light emitting diodes," J. Appl. Phys. **87**, 1974–1982 (2000).

[73] G. Xiao, J. Lee, J.J. Lioua, and A. Ortiz-Conde, "Incomplete ionization in a semiconductor and its implications to device modeling," Microelectron. Reliab. **39**, 1299–1303 (1999).

[74] R. Scaburri, "The incomplete ionization of substitutional dopants in Silicon Carbide," PhD Dissertation, University of Bologna, Bologna, Italy, 2011.

[75] U. Mishra and J. Singh, *Semiconductor Device Physics and Design* (Springer, 2007).

[76] T. P. Pearsall, "Impact ionization rates for electrons and holes in $Ga_{0.47}In_{0.53}As$," Appl. Phys. Lett. **36**, 218–220 (1979).

[77] J. S. Marsland, R. C. Woods, and C. A. Brownhill, "Lucky drift estimation of excess noise factor for conventional avalanche photodiodes including the dead space effect," IEEE Trans. Electron Devices **39**, 1129–1135 (1992).

[78] S. Selberherr, *Analysis and Simulation of Semiconductor Devices* (Springer, 2012).

[79] J. Callaway, "Optical absorption in an electric field," Phys. Rev. **130**, 549–553 (1963).

[80] Y. Hu, C. R. Menyuk, M. N. Hutchinson, V. J. Urick, and K. J. Williams, "Impact of the Coulomb interaction on the Franz-Keldysh effect in a high-current photodetector," Opt. Lett. **41**, 456–459 (2016).

[81] I-H. Tan, G. L. Snider, L. D. Chang, and E. L. Hu, "A self-consistent solution of Schrödinger–Poisson equations using a nonuniform mesh," J. Appl. Phys. **68**, 4071–4076 (1990).

[82] A. J. Seeds and K. J. Williams, "Microwave photonics," J. Lightw. Technol. **24**, 4628–4641 (2006).

[83] H. Pfrommer, M. A. Piqueras, J. Herrera, V. Polo, A. Martinez, S. Karlsson, O. Kjebon, R. Schatz, Y. Yu, T. Tsegaye, C. P. Liu, C. H. Chuang, A. Enard, F. Van Dijk, A. J. Seeds, and J. Marti, "Full-duplex docsis/wireless docsis fiber-radio network employing packaged afpm-based base-stations," IEEE Photon. Technol. Lett. **18**, 406–408 (2006).

[84] D. Dolfi, D. Mongardien, S. Tonda, M. Schaller, and J. Chazelas, "Photonics for airborne phased array radars," in IEEE International Conference on Phased Array Systems and Technology (IEEE, 2000), pp. 379–382.

[85] R. A. Minasian, "Photonic signal processing of microwave signals," IEEE Trans. Microw. Theory Tech. **54**, 832–846 (2006).

[86] G. P. Agrawal, *Nonlinear Fiber Optics* (Academic Press, 1995).

[87] J. D. McKinney, V. J. Urick, and J. Briguglio "Optical comb sources for high dynamic-range single-span long-haul analog optical links," IEEE Trans. Microw. Theory Techn. **59**, 3249–3257 (2011).

[88] J. Millo, R. Boudot, M. Lours, P. Y. Bourgeois, A. N. Luiten, Y. Le Coq, Y. Kersalé, and G. Santarelli, "Ultra-low-noise microwave extraction from fiber-based optical frequency comb," Opt. Lett. **34**, 3707–3709 (2009).

[89] A. E. Siegman, *Lasers* (University Science Books, 1986).

[90] W. H. Press, S. A. Teukolsky, W. T. Vetterling, B. P. Flannery, *Numerical Recipes: The Art of Scientific Computing* (Cambridge University Press, 2007).

[91] Experimental data provided by J. D. McKinney that were measured at the Naval Research Laboratory.

[92] I. P. Kaminow, T. Li, and A. E. Willner, *Optical Fiber Telecommunications Volume A: Components and Subsystems* (Academic Press, 2008).